Development of patient-specific, lattice-structured hip implant stems based on finite element analysis and machine learning

Thesis for The Degree of Doctor of Philosophy (PhD)

Rashwan Alkentar

***Supervisor*:** Dr. Tamás Mankovits

UNIVERSITY OF DEBRECEN

Doctoral Council for Natural Sciences and Engineering

Doctoral School of informatics

Debrecen, 2025

Declaration

Hereby I declare that I prepared this thesis within the Doctoral Council for Natural Sciences and Engineering, Doctoral School of informatics, University of Debrecen in order to obtain a PhD Degree in engineering at Debrecen University.

The results published in the thesis are not reported in any other PhD theses.

Debrecen, 2025/august/28

……..

signature of the candidate

Hereby I confirm that Rashawn Alkentar candidate conducted his studies with my supervision within the Data science and visualization Doctoral Program of the Doctoral School of informatics between 2019 and 2025 The independent studies and research work of the candidate significantly contributed to the results published in the thesis.

I also declare that the results published in the thesis are not reported in any other theses.

I support the acceptance of the thesis.

Debrecen, 2025/august/28

……

signature of the supervisor

Development of patient-specific, lattice-structured hip implant stems based on finite element analysis and machine learning

Dissertation submitted in partial fulfilment of the requirements for

the doctoral (PhD) degree in Informatics

Written by Rashwan Alkentar certified in Mechanical Engineering

Prepared in the framework of the Informatics doctoral school of

the University of Debrecen

(Data science and visualization program)

Dissertation supervisor: Dr. Tamás Mankovits

The official opponents of the dissertation:

Dr. …….

Dr. …….

The evaluation committee:

Chairperson:

Dr. …….

Members:

Dr. …….

Dr. …….

Dr. …….

Dr. …….

The date of the dissertation defense: ……2025

Acknowledgments

To my supervisor, Dr. Tamás Mankovits, I am sincerely thankful to your insightful guidance and steadfast support that made this work possible.

To Dr. Dávid Huri, Dr. Sándor Manó, and Dr. Csonkáné Dóró Lilla, your generous technical and administrative support has been invaluable assistance throughout the work.

To my work family, all my colleagues, I warmly thank you for the wonderful moments we shared together.

To my family, I love you all, thank you for your everlasting support.

Doha, a piece of my soul and my friend, and my sister, your unconditional love taught me how to be a real human being, may God bless you.

To my beloved Lama, my wife, my partner, my friend; simply my everything, you are the reason my heart smiles, thank you for being in my life.

Abstract

Because of the increase in hip implant operations over the last few decades, the design and manufacturing techniques have also been improving in order to create the optimal design that suits each individual patient and minimizes the need for revisional surgery. The hip implant fixture into the human bones has been the main concern from the biomechanical point of view. Lattice topology optimization has aided in supporting the osseointegration properties since the lattice structures have shown, once applied, the ability to produce a close-to-bone structure due to their properties. Due to their properties, lattice structures have aided in supporting the osseointegration properties once applied to the implant, leading to a better fixture for implants as strange objects into the human bone. However, the properties of the lattice structures change based on their parameters, which in turn can complicate the structure's shape and topology, making the manufacturing process a complicated task. For the purpose of saving the time and effort of the implant creation process, machine learning methods have come to support the prediction of the mechanical properties, and additive manufacturing techniques have handled the manufacturing of the complex topology of the implant structure.

This doctoral dissertation provides a comprehensive and carefully updated examination of literature pertaining to the process of the lattice optimization of hip implants. Additionally, it goes deep into the complex field of practical design optimization for the hip implant using lattice structures. With the aid of machine learning techniques, these lattice structure properties have been calculated according to desired mechanical properties. Thus, the process ensures higher overall efficiency and precision of the implant design.

The research investigates material selection, where the study shows the benefits of using the titanium Ti6Al4V alloy with the lattice structures design due to its suitable properties. This alloy has a high corrosion resistance and almost no critical interaction with the human body fluid. The alloy’s Young’s

modulus is also calculated to assess the elasticity of the selected material. The dissertation also focuses on the initial computer-aided design of the lattice structures and their applied types. Three distinct types of latticed structures with different shapes are discussed. The mechanical properties relating to unit cells and the effect they have on the general implant design are investigated. Using one of the machine learning techniques, Linear regression, the porosity of the latticed design is pre-set to be in a suitable range that results in better topology and mechanical properties for the implant design. Total numerical simulation is performed on the three designs of unit cells, then the specimens are 3D-printed, and a laboratory compression test is performed to validate the results of the simulations.

Keywords: Optimization, lattice structures, machine learning, osseointegration, Finite Element Analysis, Direct laser metal sintering, additive manufacturing, compression testing, Linear Regression.

Table of contents

Abstract....viii
Table of contents.... xi
List of figures.... xv
List of tables.... xix
Abbreviations.... xxi
Chapter 1: Introduction.... 1
Overview.... 1
Research motivation.... 7
Aims and objectives.... 9
Contribution....12
Chapter 2: Literature review....14
2.1 Metallic biomaterials....14
2.2 Bone properties....18
2.3 Cellular structures....19
2.4 Lattice structures and osseointegration of Hip implant....25
2.5 Additive Manufacturing (AM)....37
2.6 Finite element analysis in biomechanics....40
2.7 Implant optimization....43
Chapter 3: Mechanical properties of Ti6Al4V....47
3.1 Experiment setup....47
3.2 Compression test results....49
3.3 FE analysis results....50
Chapter 4. Designing and manufacturing lattice structures....52

4.1 Latticed design 52
4.2 Lattice structure's specimens manufacturing 53
4.3 Results 55
Chapter 5: Lattice structures mechanical properties 61
5.1 Preparation of the specimens 61
5.2 Compression test and FE model 62
5.3 Results 65
Chapter 6: Surrogate model Development 68
6.1 Lattice type selection 68
6.2 FE analysis setup 68
6.3 Laboratory compression test 75
6.4 FEM results 77
6.5 Laboratory compression test results 80
Chapter 7: Porosity prediction via machine learning 81
Chapter 8: Hip implant stem database 88
8.1 Introduction 88
8.2 Hip Implants data preparation from FEM 89
8.3 Regression learner results 95
Chapter 9: Conclusion and Future Work 101
Theses: 103
Thesis 1: 103
Thesis 2: 103
Thesis 3: 104
Thesis 4: 104
Publications 106

References 109

List of figures

Figure 1. Hip implant parts and location in the body [2]. 1
Figure 2. Primary and revision trends of hip replacement rates [12]. 3
Figure 3. Stress shielding scheme [29] 6
Figure 4. a) Metal screws and plates used to hold fractured bone parts together during healing, b) typical hip joint replacement made mostly of metal [40]. 15
Figure 5. Human bone structure [49].....18
Figure 6. Micro-lattice [63] 21
Figure 7. Types of lattices used with hip implants optimization [64] 22
Figure 8. bending-dominated (a) and stretch-dominated (b) structures [66]...23
Figure 9. Categories of lattice structures [75] 24
Figure 10. a) bones distribution in the normal hip, b) artificial hip implant embedded in the pelvis and the femoral canal [77]. 25
Figure 11. Geometric parameters of Hip implant. a) femur parameters, b) patient's specific implant parameters, c) the stem in front of the canal. [77]. 27
Figure 12. Human implant evolution [49] 29
Figure 13. Total hip replacement surgery steps. [77] 30
Figure 14. Hip Cementles stem designs [100] 32
Figure 15. Cemented vs uncemented prosthesis [101].....32
Figure 16. Design limits for Tetrahedron topology [124] 35
Figure 17. Octet truss design limits [124] 36
Figure 18. schematic graphic of DMLS process [136] 39
Figure 19. Parts manufactured via DMLS. a) hip implant, b) skull plate, c) Ti knee implant, d) rendered Drill guide to support stability in bone geometry [136].....40
Figure 20. Specimen for compression testing.....48
Figure 21. a) Compression test, b) FEM 49
Figure 22. Stress-strain values 50
Figure 23. Convergence study 50
Figure 24. Stress-strain graph and Young's modulus values 51

Figure 25. Dimensions and lattice details 53
Figure 26. 3D-printed specimens(a) 3D lattice infill pattern, (b) double-pyramid lattice and face diagonals, (c) octahedral lattice 2 [167] 54
Figure 27. Lattice structures geometry: (a) 3 Dimensional Lattice Infill Pattern, (b) Double pyramid lattice and face diagonals, (c) Octahedral lattice 2 [167] ..54
Figure 28. The deviation in values between CAD design's dimensions, masses, porosities and the printed specimens'. a) variance in Length, width, b) Variance in Height, c) Variance in mass, d) variance in porosity [167].....59
Figure 29. Scanning results for: a) 3-Dimensional Lattice Infill Pattern, b) Double pyramid lattice and face diagonals, c) Octahedral lattice 2 [167] 60
Figure 30. Lattice structures types: (a) 3D lattice infill pattern, (b) double-pyramid lattice with cross, (c) double-pyramid lattice and face diagonals, (d) octahedral lattice 2 [169]. 62
Figure 31. Compression test setup [169].....63
Figure 32. Mesh convergence study [169] 64
Figure 33. Simulation settings [169] 64
Figure 34. Effective Young's modulus: (a) 3D lattice infill pattern, (b) double-pyramid lattice with cross, (c) double-pyramid lattice and face diagonals, (d) octahedral lattice 2 [169]. 65
Figure 35. Young's modulus FEM. (a) 3D lattice infill pattern, (b) Double pyramid lattice with cross, (c) Double pyramid lattice and face diagonals, (d) Octahedral lattice 2. 66
Figure 36. Compression setup for 3D Lattice infill type [177].....69
Figure 37. Young's modulus of 3D lattice infill [177].....69
Figure 38. Poisson's ratio compressive test setup [177] 70
Figure 39. Hip implant [177] 71
Figure 40. a) Resin samples b) compression test setup 72
Figure 41. Application of lattice structure to the hip implant [179] 73
Figure 42. Compression test of hip implant with relation to ISO 7206-4:2010.74
Figure 43. Hip implant's cross-section with surrogate models [179].....75

Figure 44. 1 mm shell 3D printed implant 76
Figure 45. Positioning implant into the Resin 76
Figure 46. Hip implant compression setup 77
Figure 47. Compression plates' vertical deformation, latticed vs surrogate models 78
Figure 48. Mesh convergence 79
Figure 49. (a) Bulk Hip implant , (b) 3D-lattice infill, (c) double-pyramid lattice and face diagonals, (d) octahedral lattice 2 81
Figure 50. Unit cells' input data 83
Figure 51. Input data histogram: (a) 3D-lattice infill, (b) double-pyramid lattice and face diagonals, (c) octahedral lattice 2. 83
Figure 52. ML models 86
Figure 53. Prediction True vs Predicted 87
Figure 54. Hip implant accommodation in the femur 89
Figure 55. a) Forces and b) resulting moments, acting on the hip implant [182] 90
Figure 56. Forces acting on hip implant in stumbling case 91
Figure 57. True vs Predicted response graph a) Maximum displacement training, b) Maximum displacement testing , c) von Mises stress training d) von Mises stress testing e) Total strain energy training f) Total strain energy testing 97
Figure 58. FE calculated values case 2mm shell, 80-kg patient Length 0.4, Thickness 0.2 98

List of tables

Table 1. Chemical composition of Ti6Al4V....47
Table 2. Lattice structure's parameters....54
Table 3. Average measurements of the 3D-printed specimens....55
Table 4. Measured vs nominal data comparison [167]....55
Table 5. porosity values, deviation vs real values....57
Table 6. Specimen's parameters....61
Table 7. Deviation in Young's modulus values between numerical analysis and laboratorial results....66
Table 8. Poisson's ratio result....70
Table 9. Resin samples dimensions and Young's modulus results....72
Table 10. Material's properties for FEM [179]....73
Table 11. Vertical deformation results deviation between latticed and surrogate models FEM....78
Table 12. Deviations in computation results for latticed model vs surrogate model....79
Table 13. Vertical deformation Latticed model FE results vs Lab results....80
Table 14. Range of porosity's values and their corresponding values of length and thickness....82
Table 15. Numbers of learning points....84
Table 16. Accuracy values for lattice types....85
Table 17. Force values....90
Table 18. FE calculated outputs values of the learning and testing points....92
Table 19. Evaluation of the Total displacement prediction model....95
Table 20. Evaluation of the Stress von Mises prediction model....95
Table 21. Evaluation of the Total strain energy prediction model....96
Table 22. FEM calculated cases vs Trained model calculated case....98
Table 23. Hip implant stem database....99

Abbreviations

AM Additive Manufacturing

THA Total Hip Arthroplasty

FEM Finite Element Method

FEA Finite Element Analysis

TO Topology Optimization

THR Total Hip Replacement

RHA Revision Hip Arthroplasty

ML Machine Learning

DP Deep Learning

YM Young's Modulus

MRI magnetic resonance imaging

CT computed tomography

PMMA acrylic polymer polymethyl methacrylate

HA Hip arthroplasty

PBF Power Bed Fusion

DMLS Direct Metal Laser Sintering

EBM Electron-Beam Melting

DED Directed Energy Deposition

SLM Selective Laser Melting

UHMWPE Ultra High Molecular Weight Polyethylene

TPMS Triply Periodic Minimal Surfaces

SIMP Solid Isotropic Material Penalization

MMC Moving Morphable Component

MMA Moving Asymptotes

ESO Evolution Structural Optimization

VAE Variational Autoencoder

NN Neural networks

SVR Support Vector Regression

SVM Support Vector Machine

SNN Shallow Neural Network

GPR Gaussian Process Regression

DNN Deep Neural Network

DLNN Deep Learning Neural Network

MSE Mean Square Error

RMSE Root Mean Square Error

ReLU Rectified Linear Unit

Chapter 1: Introduction

Overview

Patients with hip diseases suffer while performing daily activities like walking, running and jumping, which makes hip replacement surgery a commonly needed procedure. The Total Hip Arthroplasty (THA) is a procedure where the injured hip is exchanged with a new artificial implant. The main goal of the implant is to impart the load from the acetabulum to the bone of the thigh. This dictates inserting the hip implant inside the femur [1]. Figure 1 shows the parts of the hip implant within the human body, mentioning the names of all parts involved in the procedure.

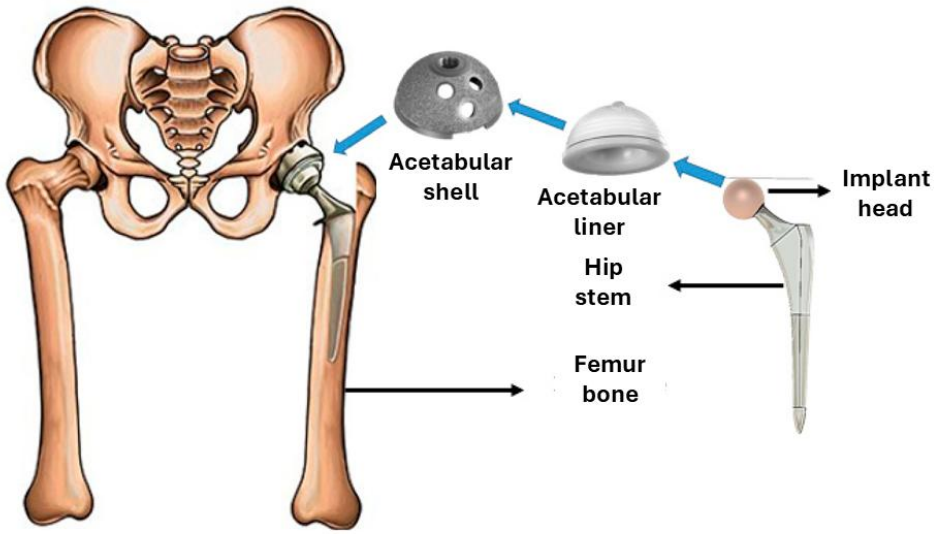

Figure 1. Hip implant parts and location in the body [2].

The artificial hip implant principle was developed in Europe in the early 1940s [3]. A good Total Hip Replacement (THR), if successful, can give the patient almost all the recovery of mobility with pain-free activities for almost 15 years [4]. Despite the fact that a successful hip implant surgery can return the activity to the patient, some cases might need a revision surgery (Revision Hip

Arthroplasty RHA) in order to resume its efficiency as expected [5]. In the ideal state, the implant stem should have full contact with its cortical bone surrounding it in the femur to attain a durable fixation of the implant into its place of insertion [6].

Research has been done in the arthroplasty field to estimate the longevity of the hip implant. All hip implants would come to an end in terms of functioning, and it is vital that patients having this kind of replacement know the approximate time of such validity. Thus, determining how long a hip replacement can last is now an essential question in the biomedical field. Total Hip Arthroplasty (THA) is considered to have a high success rate as a surgical procedure in the modern medicine [7]. Nevertheless, a low failure rate exists, and it is a high number of patients since the statistics state that 2 million arthroplasty procedures are done worldwide every year, the thing that makes a high number of patients in need of revision surgery [8]. In Germany alone, 210,000 hip implantation procedures and 30,000 revision surgeries were executed in 2011 [9].

Hip injuries are considered serious and highly damaging and might lead to a permanent disability and, sometimes, death. It Is also worth mentioning that hip fractures number worldwide is estimated to reach over 6.26 million by 2050 [10]. Between 2007 and 2017, the number of hip implant prostheses increased by a range of 30-40% [11]. Figure 2 shows the increase in hip implant revision surgeries over the years 1991 to 2010, where both males and females were investigated by T Dixon et al [12].

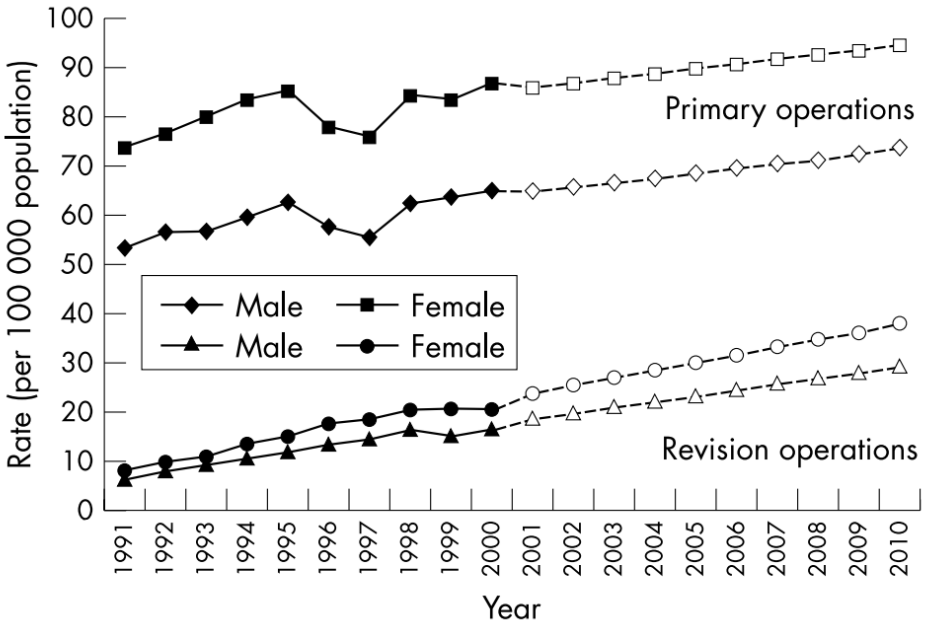

Figure 2. Primary and revision trends of hip replacement rates [12].

However, the life span of hip prosthesis can be increased by trying to adapt its properties to that of the human bone based on long-term medical studies results [13]. The ongoing research in the field of hip prosthesis motivated the innovation in material science, technology, surgical techniques and fixation methods, leading to an increase in the life span of the implant. Up until last year's statistics, 75% of hip implants last for up to 15 years [14], [15].

The human bone has a feature called "bone modeling" which enables it to adapt to the changes happening in the surrounding environment. Bone can remodel by renewing its cells in response to the novel changes of loads and boundaries. Sometimes, fractures may occur if the loads acting on the bone exceed its strength. Moreover, bone common diseases such as osteoporosis and necrosis can reduce the load-bearing capacity of the hip. Despite the remodeling feature and in case of heavily affected bones, some fractures may be permanent and irreversible [16].

Due to many bone diseases, like rheumatoid arthritis, osteoporosis and traumatic events, the number of total hip arthroplasty operations is increasing proportionally with the increment in the average population age all over the world. Over the past few years, the number of hip arthroplasty in young people has been significantly registering high values since the younger generation exert more intensive and frequent loads on the joints than the elderly. The gain or loss of the proximal femur, the closer-to-body-center part of the femur, in the presence of an orthopedic implant is the main factor affecting the performance of the durability and longevity of the prosthesis [17].

Any micromotion happening between the bone and the implant will cause the implant loosening. This creates the necessity to perform a revision surgery on the implant [18]. This micromotion needs to be minimized when designing the implant since it causes a decrease in the bone amount growing into the implant. The bone in-growth is obstructed by this high amount of micromotion, and this decrease of the bone in-growth results in a shorter lifespan of the implant [19]. The in-growth affects the implant's stability where high micromotion causes fibric membrane to develop between the bone and the implant which, in turn, leads to an unstable fixture [19], [20], [21]. The existence of such membrane hinders the bone ingrowth into the implant leading to reduced longevity [22].

Aseptic loosening is considered to be a frequent reason behind hip implant revisional surgery [23]. Aseptic loosening can mainly be caused by the stress shielding effect, which results from the implant material having a much greater elasticity modulus than that of the human bone. A bigger share of the load gets handled by the implant since it is stiffer than the bone's structure, which results in a decrease in the mechanical stimulus that incentivizes bone generation. With time, this causes losses in the bone and increases the level of

loosening of the implant. Less bone formation, in turn, makes it harder to perform any revision surgeries to implant a new prosthesis [24], [25], [26].

Figure 2 explains the mechanism of the stress shielding effect. In the normal situation, the femur undergoes the external load where the loading is imparted from the femoral head along the neck of the femur continuing to the femur cortical bone as shown in Figure 2a. When the stiffer part is inserted into the canal, the implant in this case, the load is divided between the bone and the implant. Thus the bone is exposed to a reduced amount of stress and hence the name, stress shielded [27].

The white area in Figure 3 on the left side shows the stress shielded area of the bone, while the dark area in Figure 3 on the right side shows how the femur surrounding the femur distal part is overly loaded. As Wolff's law states, the structure of the bone is developed in a suitable way to resist the loadings exerted on it. The fact that makes the parts of the bone undergoing extra load or stress respond by the increment of the bone mass, whereas the parts undergoing less load or stress will react by the decrement of bone mass. Subsequently, bone resorption results in and leads to the loosening of the implant and, in some cases, to complete failure [28].

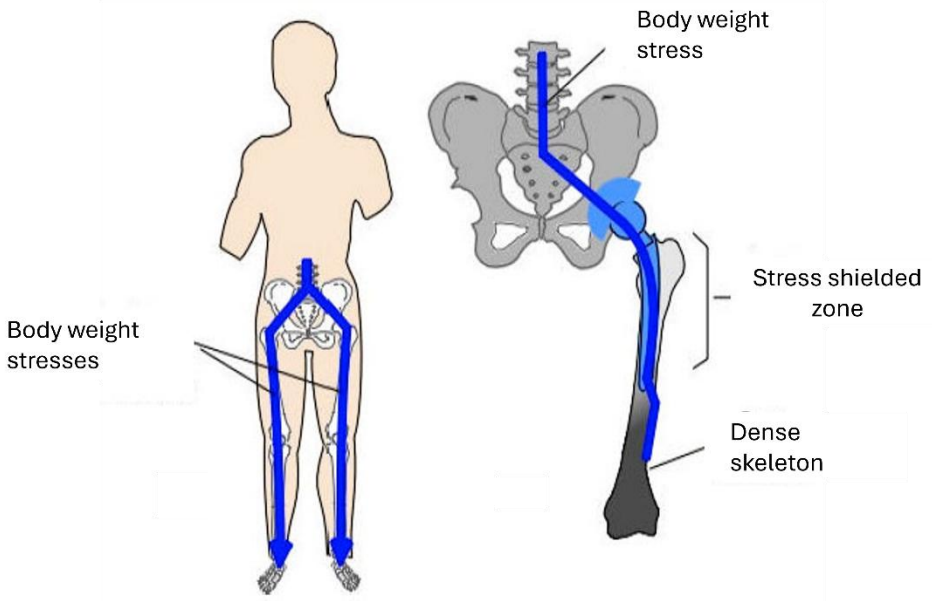

Figure 3. Stress shielding scheme [29]

In order to assess the loading taking place on the hip implant, the stress affecting the femur is one of the most important indicators, and it has been used in many studies to estimate the amount of stress shielding in the respective implant. Finite element analysis has been believed to be an effective means to analyze the load transmission to the femur through the stem. Harrysson et al. assessed the intensity of load transmission from stem to femur based on the distribution of the stress after implanting various kinds of femoral stems [30].

A study by Hazlehurst tried to mark 25 nodes in the Gruen zone (seven areas of the implant's stem) within the femur and assessed the stress shielding at every marked zone of the proximal femur by averaging the total von Mises stress on the distributed nodes in each section [31], [32]. In the end, not only have researchers evaluated *SS* stress shielding, but also, they were able to assess based on the change ratio of the femur stress after implanting the femoral stem, as shown in Equation 1.

$$SS\ (\%) = \frac{S_{int} - S_{stem}}{S_{int}} \cdot 100, \quad (1)$$

Where S_{int} is the von Mises stress on the functional femur, S_{stem} is the von Mises stress on the implanted femur [33].

Many factors can influence the existence of micromotion of the implant including the strength of the bone surrounding the implant, the surface contact between the implant and the bone, and the friction coefficient of the contact surface [34]. While the strength of the bone is a measure that cannot be controlled, designers can manipulate the surface contact during the designing process of the implant by enlarging the surface area. Each design can be better for each type of bone. A design type suitable for osteoporotic bones might be totally different from a design type for a child or healthy adult. Surface texture might also be achieved by application of material finishing properties or via the application of coating to the implant [35].

For the purpose of minimizing micromotion in the hip implant, a primary factor to take into consideration is stress distribution all along the implant. This comes from the fact that various loads on the implant can make a change to the density of the bone and the shape around the implant. A successful implant is the one that can guarantee equal distribution of stress around the whole surface of the implant. Increased bone density will result in areas of high stress whereas decreased density will exist in areas of low stress. Thus, the uneven distribution of the stress around the implant might cause unstable fixation [36].

Research motivation

Even though hip arthroplasty, a widely performed surgical procedure, has provided relief to millions of patients suffering from extensive pains and disorders in the hip joints, and despite the improvement in the surgical techniques and material science, the challenges still intercept the creation of

optimal implant longevity and functionality for the patient. The conventional solid implant often shows limitations as stated in the previous chapter. Thus, the need to explore innovative approaches arises. The integration of lattice structures into the hip implant design is one of the up-to-date approaches to address the recurrent hip implant issues.

Lattice structures are characterized by their open interconnected framework and have offered a remarkable advance in various engineering applications due to their excellent combination of lightweight properties, structural efficiency, and enhanced material utilization. With the incorporation of lattice structures into the design of the hip implant, we believe several potential benefits can be achieved. Lattice structures can help with organizing the mechanical loads distribution more efficiently across the implant-host bone interface and can reduce the stress shielding phenomenon. This can lead to better long-term stability and reduce the risk of complications related to the hip implant.

The research also seeks to build an enhanced osseointegration for the implant to the hosting bone. The porous nature of the lattice structures provides a larger surface area for the bone ingrowth, which facilitates the improvement of osseointegration and stability. More bone ingrowth leads to a quicker post-operative recovery and reduces the need for revision surgeries.

Advanced materials can be used with the utilization of lattice structures while maintaining implant strength and functionality. This enables the optimization of the weight of the hip implant which eliminates discomfort and improves the patient's mobility.

The parameters of lattice structures can be manipulated so that they can match patient-specific anatomical characteristics, which allows for more precise fitness and improved biomechanical properties and performance. The

personalization of the hip implant design holds the potential to optimize the outcomes and minimize the implant-related complications.

During the research, many challenges and objectives will be discussed. While the integration of the lattice structures into the hip implant design adds a significant value to the process, it still creates some interesting questions to be answered to ensure successful clinical implementation. The challenges include choosing the suitable material of the latticed implant that should be compatible with the hosting bone in order for a better osseointegration to be accomplished. The optimal lattice topology and design selection, where we seek creating the optimal implant design based on the patient's anatomical characteristics.

With the optimization process and the application of the lattice structures into the implant, the manufacturability of the designs should also be guaranteed to build a fruitful creation process of the implant. The long-term biocompatibility and durability assessment of the implant are also crucial factors in the process to ensure an efficient prosthesis.

The main incentive of this research is to address these challenges and advance the hip implant optimization process through the optimization of lattice structures. We aim to establish a solid method for the integration of the lattice-enhanced hip implants into orthopedic practice for the sake of enhancing the surgical operations success rate and increasing the longevity of the hip prosthesis. Ultimately, the research is trying to improve the quality of performance for the individuals undergoing hip arthroplasty.

Aims and objectives

The main aim of this dissertation is to optimize the hip implant arthroplasty by the integration of lattice structures in order to reach an improved biomechanical performance and patient outcomes, which imposes

the optimization and analysis of many factors. Optimizing the hip implant for the study means gaining a better fixation through increasing the osseointegration of the implant into the human body. As explained in the introduction, implant fixation can be enhanced by improving the bone ingrowth and preventing the micromotion of the implant that might cause loosening. Throughout the dissertation, many objectives should be achieved to reach the final goal of an efficient optimization for hip implant that can be patient-specific i.e., the methodology suggested here should adapt to the needs and requirements of the patient. These objectives can be summarized by the following:

- Within the literature review, the objective is to establish a comprehensive understanding of the current hip implant designs, studies, their limitations, and the expected benefits of integrating the lattice structures. Moreover, the research seeks to conduct an extensive literature review on the existing hip prosthesis biomechanical performance and limitations.
- Investigating and analyzing the impact of various materials on the real performance and durability of orthopedic implants via conducting a detailed literature review on many materials used in the biomedical field. The investigation will also surf through biocompatibility, the mechanical properties and the corrosion resistance of the chosen materials, given that these properties are the most important characteristics to have in a candidate for an orthopedic implant. After that, the study identifies the most suitable material within the current research.
- The optimization of design of the orthopedic implants for an enhanced structural integrity and a good functional performance. Via the utilization of the computer-aided design (CAD) tools, the research develops the novel implant design with the incorporation of the

biomechanical principles. Lattice structures are integrated into the novel design of the hip implant to optimize the structural design of the implant to better suit the hosting bone.

- Using Finite Element (FE) simulations for validating the performance of the lattice structured hip implants and using the FE tools to enhance the mechanical behavior of the orthopedic implants. The study also uses the FE models in order to accurately represent the real-world condition of the implant loadings and restrictions. FE also helps guide the optimization of implant design and the material selection.
- Exploring the potential of additive manufacturing technology and 3D printing techniques in the manufacturing of orthopedic implants with the concentration on the implant design customization and the material innovation. The research also investigates the feasibility of using patient-specific data to customize the implant design with the help of additive manufacturing. Practical use of the 3D printing will be used to print some samples as a preparation step before some laboratory tests.
- Implementing optimization techniques to boost the overall performance of and functionality of orthopedic implants. The study also applies optimization algorithms to identify the optimal combination of design parameters for an improved lattice-structured implant performance. Machine learning optimization is utilized in the optimization of the design and the performance of orthopedic implants. Optimization with the help of machine learning techniques enhances the research ability to investigate the use of such techniques in the prediction of the mechanical behavior and failure modes of orthopedic latticed implants. The machine learning model is developed based on historical performance data that generated good biomechanical result of the implant design.

By addressing these points, the research seeks to comprehensively introduce the effective optimization of the hip implant for the sake of creating the most-suitable patient-specific design of the implant with a set of pre-investigated parameters that can ensure a successful and reliable life of the implant.

Contribution

Despite the fact that there is much research concerning hip implant optimization, the results are still more generic than specified. Standardization of the hip implant design is helpful with the manufacturing process and gets unified requirements. However, the customization of the hip implants with the use of lattice structures will create an implant design, for each individual patient, that can enhance the stability and fixation of the implant inside their bodies. The unique aspect of this research lies in its ability to produce customized, patient-specific design of the hip implant with pre-defined parameters.

- Personalized design:

  The traditional hip implants usually come in standard shapes and sizes, which may not perfectly suit the anatomical features of every patient. This study seeks to address this limitation by the incorporation of lattice structures into the design process. These lattices can be customized to improve the match between the implant's structure and the hosting body, ensuring a better fit and reducing the risk of the complications associated with ill-fitting implants.

- Tailored parameters:

  By optimization, the study means to incorporate lattice structures into the design of the implant to optimize the implant's mechanical properties, enhancing its strength, durability and fixation, while minimizing the total weight. This can contribute to long-term performance and reduced wear of the implant. A systematic approach

is involved in this research to set parameters for the lattice structures. This includes factors such as bone size, shape and porosity. By defining these parameters in advance, the research can streamline the customization process to allow for an efficient and accurate generation of patient-specific hip implant design.

- Advanced computer modelling and simulation.

The thesis uses advanced computer modelling and simulation techniques to help analyze the biomechanical properties of the customized hip implant designs. This helps provide a thorough evaluation of the way the implant will interact with the patient's unique anatomy and how it will react against the various conditions. Optimal performance can be obtained with the help of the simulation and modelling process.

- Reduced complications and improved outcomes:

Once the optimization of the design by adjusting the hip implant parameters for each patient can be done, the research will be able to reduce the risk of complications such as the implant loosening, dislocation, and wear-related issues. Finally, the personalized approach can improve the patient's outcomes, reduce recovery times, and enhance the overall quality of the implant along its lifespan for individual undergoing hip replacement surgery.

Chapter 2: Literature review

2.1 Metallic biomaterials

Biomaterials can be defined as materials that are fit for usage in medicine and dentistry where these materials are subject to direct contact with the live tissue inside the human body [37]. The basic first decision with relation to the implant design is the suitable selection of biomaterials. And to make it clear, the term "biomaterial" directly refers to those materials that have an interaction with the biological parts in the body (tissues, organs, etc.), and they have the ability to help facilitate the reformation process of tissues without causing any uncalled-for results, i.e. toxicity, irritation and carcinogenesis [38], [39].

Biomaterials are divided into four main groups polymers, ceramics/glasses, metals, and composites, which can be a mixture of any of the rest of the groups. Each type of biomaterial to be dealt with is classified under one of these four types. Hence, it is necessary to understand the basic features of these groups well before going on to the designing stage of the implant [40].

Metallic biomaterials constitute the majority of biomaterials used in the most up-to-date manufacturing of implants and have witnessed widespread usage over the past few years. Metals used for implant material possess elevated strength, are less susceptible to fracture and are famous for their ability to resist corrosion. Currently used metallic biomaterials can be divided into three main groups: cobalt-based alloys, iron-based alloys, and titanium-based alloys.

As shown in Figure 4, musculoskeletal surgeries appliances are made fully or in part of metal. Metallic biomaterials can be counted on because of their high strength and the ability to withstand failure even when fatigue is considered. If the right biomaterial is chosen for the implant, then the latter can provide relief

from pain and regain function to the joints within which the cartilage was worn or damaged [40].

a b

Figure 4. a) Metal screws and plates used to hold fractured bone parts together during healing, b) typical hip joint replacement made mostly of metal [40].

The selection process for medical devices might sometimes be a complicated one. It depends on many factors. The main factors to be considered are the mechanical loading parameters, the biological requirements, chemical properties, and structural designing parameters. Metallic biomaterials have advantages over other materials like polymers and ceramics because they are tough, strong, and ductile (deformable, especially with comparison to ceramics).

However, metallic biomaterials have some disadvantages that include exposure to corrosion which is due to the nature of the metallic bond. During the 1960s, most of the steel-based biomaterials used with implants malfunctioned due to

corrosion, which led the designers to the alloys of titanium and cobalt-chrome for hip implants. It is worth noting that metallic biomaterials have a higher density and stiffness than most of the other natural materials used. These two properties lead to the undesirable issue of stress shielding. Stress shielding does not allow the tissue to be exposed to the natural levels of mechanical loading which causes the tissue to weaken and thus causes the loss of bone in the areas adjacent to the implant [40].

316L Stainless steel, titanium alloy Ti6Al4V and Cobalt chrome alloys CoCr have been extremely used as biomaterials for the orthopedic implants because of their suitable biological and mechanical properties [41]. The titanium alloy Ti6Al4V has proved to be a good candidate in the field of orthopedics due to its excellent biocompatibility, weight ratio, superior corrosion resistance and the low Young's modulus with comparison to the other biomaterials [42]. Young's modulus is a crucial factor in assessing the mechanical performance of implant materials. As for the TI6Al4V alloy, Young's modulus is approximately 110 GPa which is way higher than the human cortical and trabecular bone's Young's modulus which is around 10 to 30 GPa for cortical bone and 0.8 to 5 GPa for trabecular bone [41], [42], [43].

Since the titanium alloy is chosen for most of our research throughout the years of study, a general review is proposed on the metallic group of biomaterials. Titanium is considered the most biocompatible material out of all the metallic biomaterials since it can resist and tolerate body fluids. It has been used in the implant manufacturing field for more than 30 years. Its main advantageous properties include high strength, corrosion resistance and low weight, which led to a various range of successful applications. Titanium in the pure state has a high melting point, low density, and an elastic modulus of 107 GPa.

The titanium alloys came into the play to offer highly damage-tolerant implants. The low Young's modulus of Ti alloys with comparison to the steel implants is an advantage because it reduces bone resorption. Ti alloys are the perfect choice when direct contact between the implant and the tissue or bone is required. However, the low shear strength of titanium alloys makes them less of a candidate for manufacturing screws or plates. In addition, they do not have good surface wear properties and tend to seize when they have sliding contact with another TI alloy. Usually, the poor surface properties are improved via nitriding and oxidizing [44].

The selection of materials in the research is set on the titanium alloy Ti6Al4V of grade 23. As shown by the previous research done in the field, this alloy is widely known in the joint replacement field. This is due to its suitable biomechanical properties. These good qualities can be summarized by high fatigue resistance, osseoconductivity and biocompatibility. Since the manufacturing process to be used during the research is the direct metal laser sintering DMLS, i.e., a laser-based method, the titanium alloy properties are important to consider based on the condition of laser manufacturing techniques.

Ti6Al4V alloys to be a raw material for laser manufacturing are usually preprocessed because they usually form a martensitic-like microstructure which makes them have fast cooling, high temperature gradient, and high strength. However, they are brittle with low ductility of elongation 5%. The residual stress is high in such formations which causes stresses to remain in the manufactured part and can result in some defects [45]. This fact dictates the necessity for heat treatment after processing, which can relieve the residual stresses and can increase the elongation percentage up to 10% [46].

2.2 Bone properties

Bone is a resilient and firm tissue that provides structural enhancement to the body. Since it is a living structure, bone usually adapts to the surrounding environment and applied loads. The bone reactions to existing loads can be summarized by the following: The more the bone is loaded, the harder and denser it gets [47].

The normal human bone is usually composed of two main sections: the cortical the cancellous [48], [49]. The cortical bone is the outer layer of the bone tissue which contributes significantly to upholding the bone's structure stiffness and integrity. Additionally, cortical bones constitute approximately 80% of the total bone mass in the human body. Figure 5 presents a detailed depiction of a representative bone structure [49].

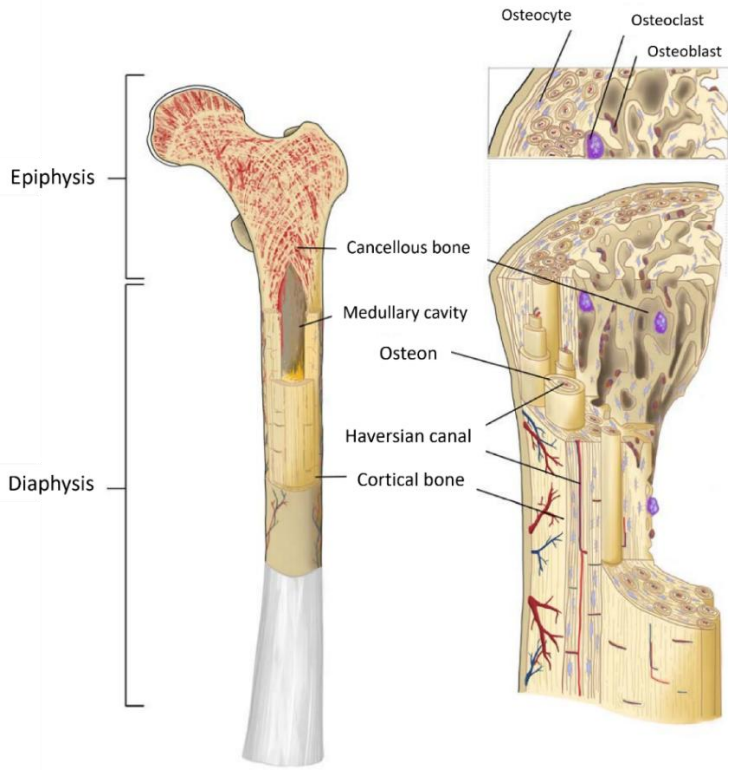

Figure 5. Human bone structure [49]

Cancellous bones resemble latticed structures, a feature that helps the bone to keep its strength and, at the same time, be lightweight compared to other bone types. Cancellous bones are usually situated at the long bone ends and in the structure of the short bones which is related to its ability to improve the transition of loads through such structures.

General bone health is mostly measured depending on the integrity of the cancellous bone. It was discovered that, at any certain age, men and women have different cancellous bone structure. Men have more trabecular bone mass compared to women, however, they both have the same probability in the decrease of the cancellous bone's density with aging [50]. This explains the sex and age considerations when designing orthopedic implants. These changes in the lattice design of the cancellous bone also require an implant design that can adapt to such changes [51].

Lattice structures help modify the metallic biomaterials in a way that makes them similar in structure to the human bone by reducing their toughness and increasing their porosity. Consequently, over the past few decades, there has been a growing scientific interest in incorporating porous structures, like lattices, into the implant designs in a trial to create bio imitation of the bone structure and enhance biocompatibility.

2.3 Cellular structures

Natural cellular-structured materials such as cork, wood, and bone have been used for decades and their structure has been imitated in modern technologies such as the manufacturing of foams and honeycombs [52]. Lattice structures are an appealing option for many design applications in many fields, especially for the light-weighting feature due to the fact that they have a high specific strength and stiffness by virtue of their porous structure [53]. Lattice

structures have also proved useful with energy absorption applications based on their deformation behavior [54].

Lattice structures are considered to be another type of cellular materials that is usually differentiated from the foamy structure by the regular repetition of their unit cells [55]. Gibson [56] states lattice structures to be consisted of interconnected networks of struts or plates. Ashby, however, further explains that lattice structures are a form of cellular materials and they differ from engineered structures like trusses in terms of their scale where the lattice structure has a millimetric or even a micrometric scale [57].

These definitions lead to the conclusion that a lattice structure should be dealt with as a material with its own mechanical properties, which gives the opportunity to directly compare between the parent materials properties and the newly generated lattice structures.

Lattice structures are primarily composed of layers of interconnected beam elements that form a lattice-like body. This gives the designers the ability to effectively control the flow of material in the desired structural design [58]. Because of their suitable properties and useful characteristics, lattice structures have been increasingly involved within the structural design field. Mainly, their exceptional ability to be easily adjusted geometrically and to have their properties controlled [59].

Seharing et al. described lattice structures to be a porous and hollow formation that are done by positioning the cells in a three-dimensional space [60]. As to Helou et al., lattices are explained as a space-filling unit cells that can be tessellated along any axis without the existence of gaps among the cells [61].

Another interesting fact about lattice structures is that their characteristics are dependent on the number of cells, the material, cell's orientation, strut distance and the manufacturing process [62]. Sakshikokil et al. [63] designated the

micro-lattice structures and explained that their resistance to the exerting loads is a feature related to the micro-construction and it is measurable with the help of the amount of stress-energy that builds up in the latticed structure after applying the loads.

Figure 6 shows the models of the micro-lattice structures.

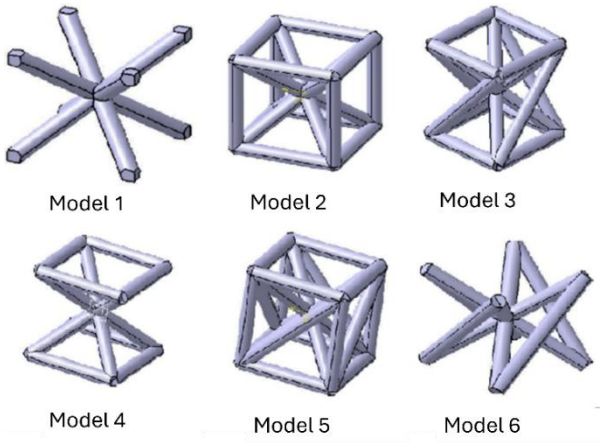

Figure 6. Micro-lattice [63]

Hanna et al. [64] showed the types of unit cells used with hip implant optimization in some cases. Using a 15-mm-diameter cylinder their research shows the types of lattices after optimizing the design as shown in Figure 7.

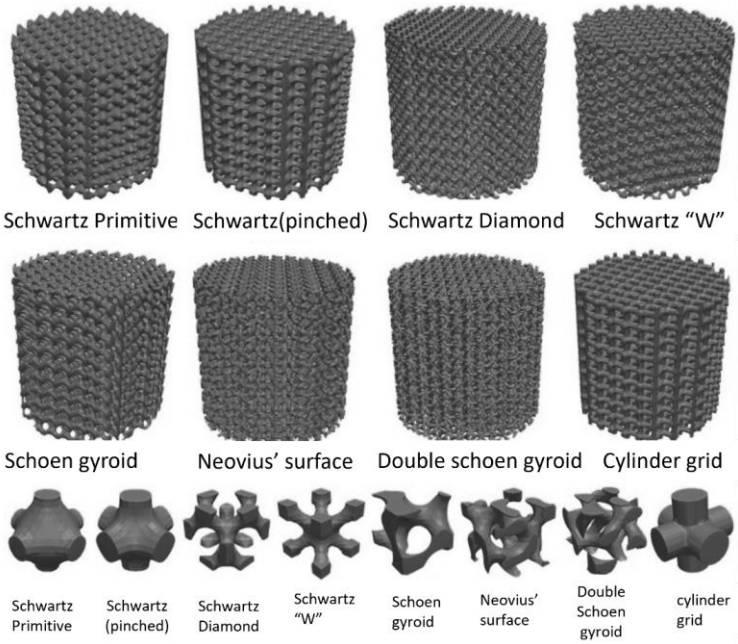

Figure 7. Types of lattices used with hip implants optimization [64]

Although there are many definitions that try to simplify the principle of lattice structures, there is still no agreed-upon definition. That is mainly because cellular structures are not only limited to the changing size of the struts and the connection type between cells. Many researchers have their own definition of the lattice structures, but most of them are based on the definition stated by Gibson and Ashby's of lattices as mentioned in the beginning of this chapter.

Lattice structures are generally, based on their mechanical response, divided into two separate groups being either bending-dominated or stretch-dominated. The difference between the two categories is that the bending-dominated structures usually experience bending moments inside their structure, and they comply with the pressure since there are not sufficient struts to equilibrate the bending moments at the joints, Figure 8, a. On the other hand, stretch-dominated structures bear axial loads because they have adequate struts to intercept the load and equilibrate the load, thus they are more stiff and stronger than the latter type, Figure 8, b [65]. The topology of

the unit cell usually is the main factor in determining whether the structure will be bending or stretch-dominated.

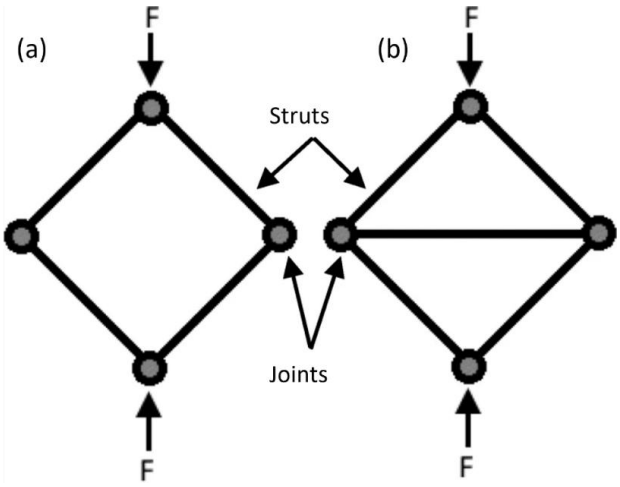

Figure 8. bending-dominated (a) and stretch-dominated (b) structures [66]

The lattice structures are cellular materials where the material's topology distribution is carefully governed and optimized for special properties or functions [67]. The classification of lattice structures relies on their applied relative density, the fact that leads to three distinct groups. These groups include the foamy structures that has low relative density up to 5%, lattices with relative density ranging between 20% to 50%, commonly known as architected materials, and structures that have a relative density exceeding 60% which shows mechanical responses that resemble, to a high extent, bulk materials [68]. For some existing literature [69], [70], the relative density of each material of lattice structure depends on the ratio between two design-related parameters: thickness of the strut (t) and the length of the unit cell (l).

Another categorization system divides three-dimensional lattice structures into non-stochastic (periodic) and stochastic (foam) structures basing on the order of the unit cells, and every structure can be also categorized into open-cell and closed-cell structures as shown in Figure 9 [71]. The open-cell foam type

structures have open walls for its unit cells, which is usually formed using an inflation during its production, leaving only the framework that permits the gases and the fluids to pass through easily [72].

On the other hand, closed-cell structures have cells with closed walls and usually are non-porous and impermeable. Non-stochastic structures are also called as periodic or lattice structures, where the unit cell of each shape is repeatedly organized like honeycombs and trusses [73]. Stochastic structures have metallic and non-metallic foams which form a spongy structure [74].

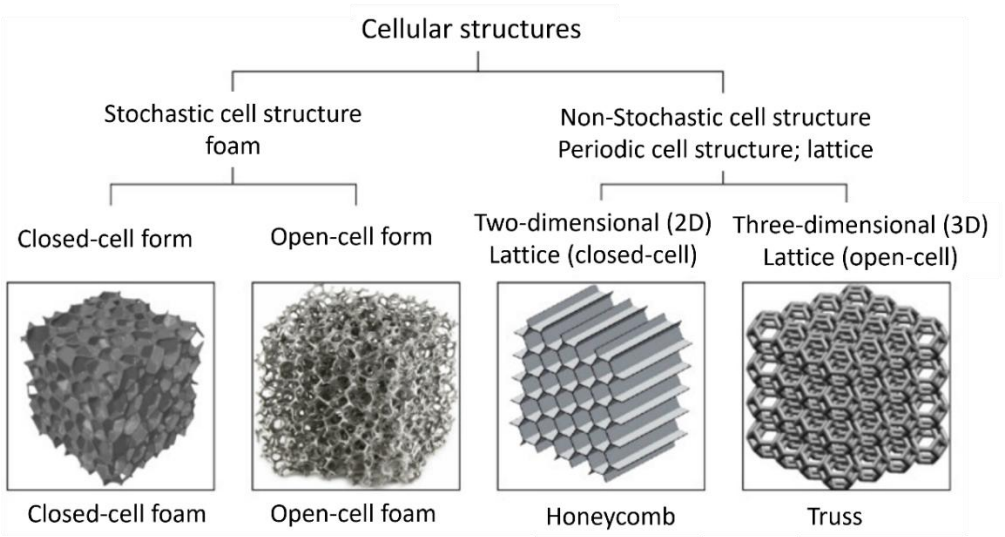

Figure 9. Categories of lattice structures [75]

Lattice structures are, consequently, a good option to be implemented into the orthopedic implants. In our research, lattice structures of non-stochastic 3D cell truss structure type were considered based on the ANSYS software used to perform simulations and on the 3D printer used to 3D-print the actual designs. This type of lattice structure offers an easier approach with unit cell parameters control, a feature that creates room for optimization, where optimal mass distribution and better bone ingrowth can be obtained [76].

2.4 Lattice structures and osseointegration of Hip implant

2.4.1 Hip implant design

The human hip joint is the largest type of ball-and-socket joint in the body, where the upper thighbone or the femur moves freely inside the hollow socket of the pelvis that is cup-shaped as shown in Figure 10, a. This mechanism gives the lower extremity the free motion within a certain range while holding the upper part of the body and withstanding the impact resulting from the movement [77]. Hip implant is usually composed of three main parts: the head, the cup and the stem as shown in Figure 10, b. The stem is inserted into the endosteal face of the canal of the femur and provides the stability needed for the implant. The cup is considered to be the replacement of the damaged acetabulum in the pelvis, and the spherical shaped head (the ball) fits into the acetabular shell immersed in the cup.

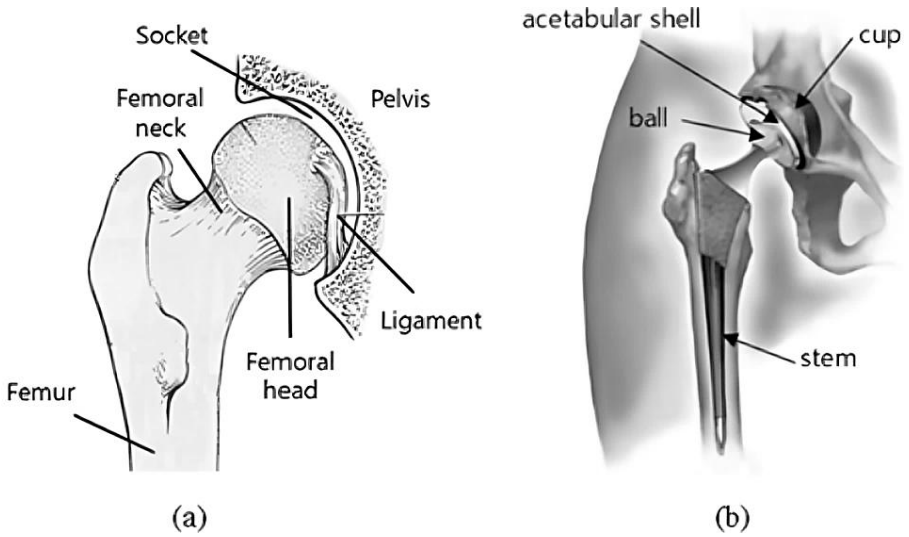

Figure 10. a) bones distribution in the normal hip, b) artificial hip implant embedded in the pelvis and the femoral canal [77].

Osteoarthritis (damage of the cartilage covering the bone ends) and osteonecrosis (blood flow is not enough for the joint, which causes fracture or

dislocation), are common as diseases that happen to the hip area, this may necessitate the total hip replacement surgery. Hip dysplasia, as well, is the event of dislocation or displacement of the joint in the hip area. In this situation, the hip socket is not able to cover the ball of the upper part of the thighbone [78], [79].

Hip replacement surgery can relieve the pain, support the hip function, and improve the mobility of the patient. However, many factors may affect the performance of the implant including size, design, weight material and age of the patient [80]. As mentioned before, in case of implant loosening, a second surgery might be needed to rectify the position of the implant. In most cases, the loosening is a result of the stress shielding discussed earlier [7].

Figure 11 a and b demonstrate relationships between the human thigh bone and the associated implant. Once the suggested system extracts hip joints, parameters determining the shape of related implants becomes a straightforward process. It is essential to note that the actual size of components may vary, either larger or smaller compared to the corresponding parameters of a patient's hip joint.

Ensuring stability is important, and to achieve this, it is ideal for femoral components of the implant to conform to the surface of the thigh bone canal as shown in Figure 11, c. The design of the stem profile aims to align with the shaft of the thigh bone while avoiding any interference with the canal. The length of the stem is established based on its position within the thigh bone canal specifically located 80 mm from its trochanter.

Adjustments in factors like neck shaft angle and head offset length are made based on a patient's head parameters. The anteversion angle for implanting in neck is also determined by considering a patient's anteversion parameter. Additionally, obtaining information about cup size implanted in the pelvis involves utilizing the head parameter. In summary, all dimensions related to a

patient's implant components are defined using primary geometry parameters derived from their own hip joint.

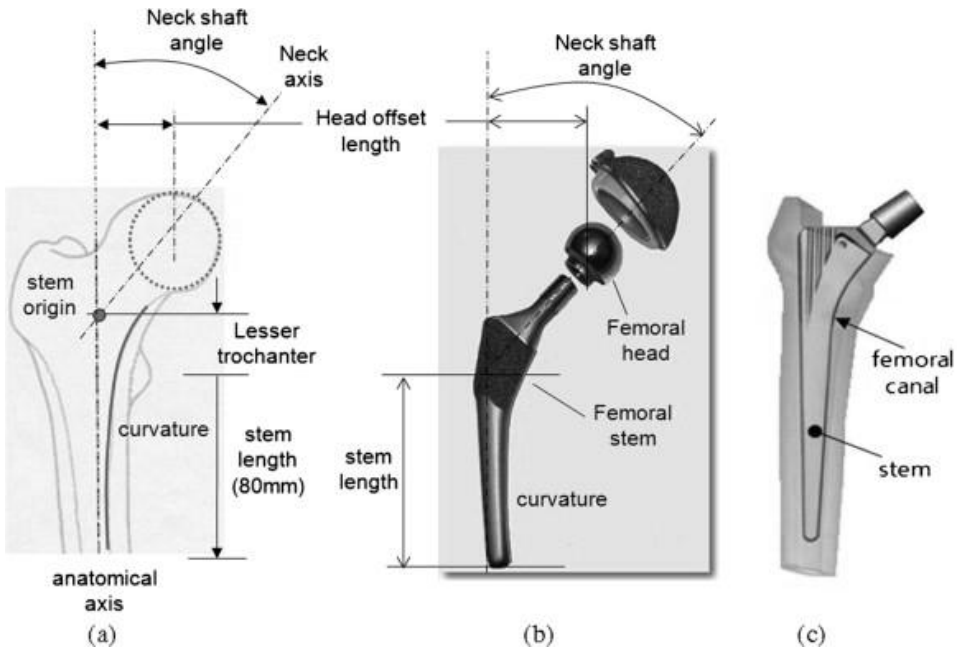

Figure 11. Geometric parameters of Hip implant. a) femur parameters, b) patient's specific implant parameters, c) the stem in front of the canal. [77].

In some cases, the geometry of the designed implant may be unacceptable to the surgeon performing the surgery with relation to their medical expertise and knowledge. In that situation, the surgeon might choose a different design of the implant in order to insert some practical knowledge to generate an optimal design for the implant. Thus, every implant design should be confirmed with the surgeon performing the operation before moving on to the manufacturing stage in order to achieve a more reliable design of the hip implant [77].

2.4.2 Hip implants

Over the past few decades, many researchers have tried to investigate hip implants to improve their design to obtain a successful long-term result. High

percentage of these studies tried to assess the fit state of the implant design based on 2D radiographs [81]. Noble et al. [82] investigated statistical research on femoral geometry of American subjects with the use of 2D radiograph Khang et al. [83] tried using the CT to study 38 femurs taken out of cadavers and 200 femurs out of living Korean subjects. Results proved that femurs taken from Korean differ from those taken out of American. Computed tomography's use has been increasing in studies to study and analyze the anatomy of the femur [84].

Many attempts were made to create a design of patient-specific hip implant that can bear the physiological load transfer and provides sufficient stability [85]. Sugano et al. [86] was able to develop a CT-based technique with computer preoperative planning and put this technique into comparison with the traditional X-ray method that is generally used.

Göetzea et al. [87] tried to develop custom-made implants in pursuit of finding a solution for the geometric difference between the anatomy of the femoral canal and the conventional stems. Healy, [88] on the other hand, tried to focus on the selection of the hip implant for the arthroplasty in the elderly with regard to bone quality, implant fixation, morphologic properties and implant cost. Walker et al. [89] set the rules and principles for femur and presented its feasibility based on the analysis of the proximal femur.

During the last century, surgical operations methods have been improving along with the newly invented imaging devices and techniques, especially, the computer tomography CT, and the magnetic resonance imaging (MRI) [90]. No matter how developed the implants rationale can get, there will always be some main properties that need to be existent, ease of tissue regeneration and high biocompatibility for example.

Throughout the years, human implants are chronologically ordered into three generations based on their evolution [91], as can be seen in Figure 12. The

oldest generation is about the implants developed for fixation purposes and to enhance the damaged tissues, and they were famous for being completely inert towards the surrounding biosystem, i.e., no interaction whatsoever [92].

The next generation includes the implants with developed materials and structures that enhance the structural integrity and supports the blood diffusion along with the flow of nutrients, which leads to high biocompatibility [93]. The latest third generation contains the previously mentioned properties and features plus the biomimetic and bioactive properties [94], [95].

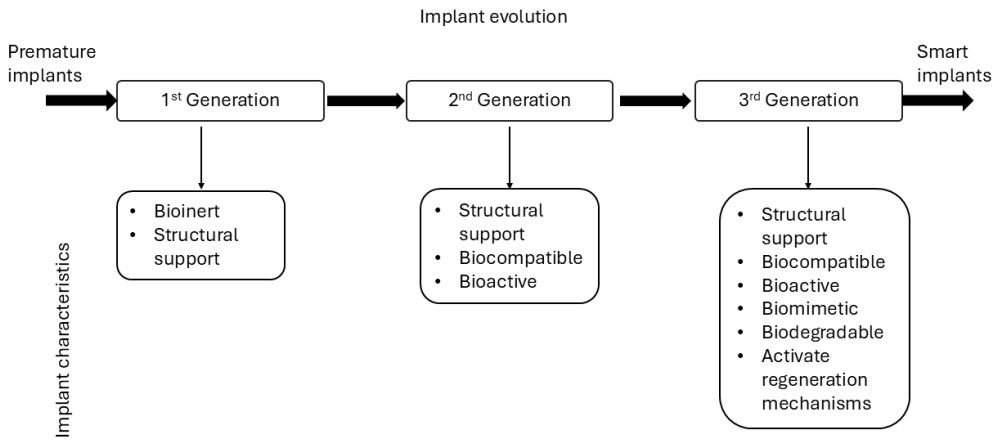

Figure 12. Human implant evolution [49]

Implants from the third generation can be enhanced by applying some of the growth factors on their outer surfaces, and that is to facilitate the tissue recreation process.

Several artificial types of implants are being used these days with replacement procedures. Yongtage et al [77], adopted the following steps in the THR surgery as shown below in Figure 13. The surgeon carefully selects the implant type that aligns with the needs of the patient depending on many 2D X-ray scans, then, the femur is extracted from the pelvis area to reveal the joint cavity. The femoral head is sliced into two segments slightly distal from the bigger

trochanter. The acetabulum of the pelvis is then expanded with a reamer, and the acetabulum is securely fixed into the reamed socket. The endosteal surface of the canal of the femur is punched to make a cavity matching the shape of the stem. In the end, the implant ball is inserted into the acetabular shell so that the joint is well aligned and finally the incision is sealed.

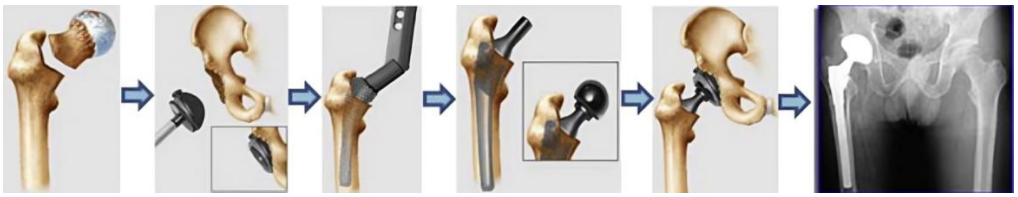

Figure 13. Total hip replacement surgery steps. [77]

2.4.3 Hip Stem fixation

The stem of the implant is inserted into the body bone and responsible for holding the hip implant in place. This creates a classification of the hip implants based on the way they are fixed into the body. The two most common techniques of fixing the hip implants into the bone are the cemented and cementless. Over the recent 40 years, many developments have been added into the cemented THA methods and materials.

In the cemented technique, the implants are glued by the use of cement, whereas, in the cementless implants, fixation takes place biologically [96]. During the cemented method, PMMA (acrylic polymer polymethylmethacrylate) [97], which is a powder mixed with monomer. The mixture preparation takes around 8-10 minutes relating to the surrounding temperature and humidity. Once the mixture is ready, it should be inserted into the patient's bone, and it should be followed by the implant. Both the implant and the bone should be held firmly against each other till the formation is completed.

For the cementation process in the THA to succeed, it is crucial to well take care of bone preparation and the application pressure of the cement. Some risks are to be expected with this technique. Mostly, the possibility of fracture in the interface between the bone and the cement. Moreover, certain allergies might arise for some patients against the materials used in the mixture. Consequently, the cementless THA was invented in order to replace the cemented technique when in need [98].

Around the year 1980, the newly improved design of implants was introduced as cementless implants. Cementless implants are directly inserted into the canal that was prepared by the surgeon performing the surgery. In order to guarantee minimal micromotion of the implant and to enhance the bone ingrowth process, the stem should be well stabled within the bone. The surface of the cementless implant is usually made porous in order to facilitate the osseointegration that also, in turn, enhances stability. Long-term stability and success of the implant greatly depend on the initial stability in its early stages [96].

Patient's weight, shape of the implant, and bone's quality can affect the initial stability of the implant [99]. Khanuja et al. classified the cementless implants into six different groups according to their geometries and how the fixation is achieved. The six groups can be summarized as the following: Single wedge prosthesis, Double-wedge prosthesis, Type 3 are tapered and round, tapered and splined, tapered and rectangular, Type 4 is cylindrical and fully coated, Type 5 is modular, and Type 6 is anatomic [100]. Figure 14 shows the six types of hip implant stems.

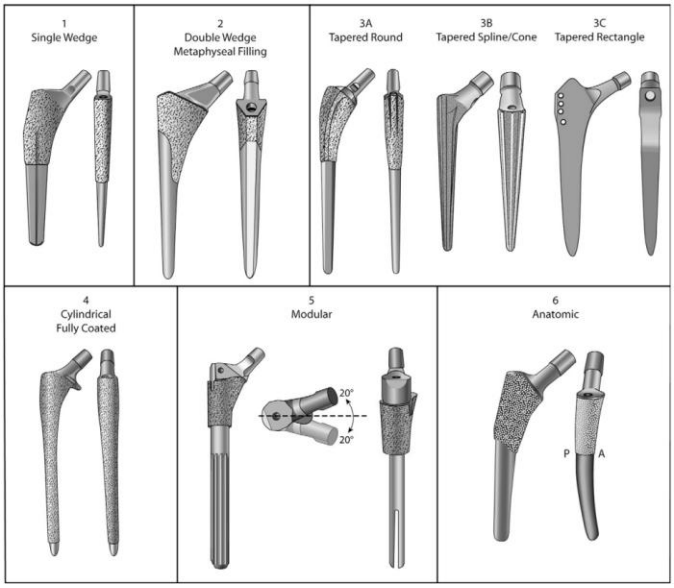

Figure 14. Hip Cementles stem designs [100]

Figure 15 shows a comparison between the cement and cementless hip implant design. The left side shows the cemented prosthesis where the cement attaches the metal to the bone. On the right side, however, the cementless prosthesis can be seen to have fine mesh of pores on its surface area that gets in touch with the bone.

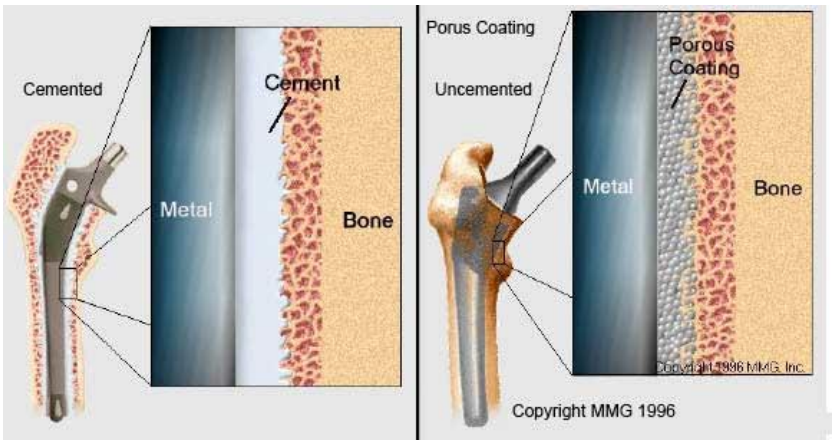

a b

Figure 15. Cemented vs uncemented prosthesis [101]

2.4.4 Implant osseointegration

Branemark defined the principle of osseointegration to be the direct structural and functional connection between living bone and the adjacent surface of the implant carrying the load. On his initial remarks on the osseointegration process, Branemark stated that the titanium implants were able to permanently integrated with the bone where the living bone and the titanium oxide layer of the implant could be fused to the extent that separation can only be done with fracturing the connection [102], [103]. Basically, osseointegration is a fixation mechanism where non-vital object can be inserted into living bone and can survive under all usual parameters of loading [104].

In the biomedical field, an implant can be described as osseointegrated in the absence of motion between the bone and the implant that is in immediate contact with it. However, osseointegration features the clinical status that describes a long-term stability of the implant and this is not a biological feature of the implant itself or the metal [105]. Moreover, osseointegration is not the outcome of a favorable biological tissue reaction, but rather the absence of a negative tissue response [106].

Many factors can contribute to the performance of the osseointegration process. They are divided into two categories, factors that support osseointegration and factors that hinder osseointegration. Factors supporting osseointegration include factors related to the implant itself like material, length, diameter, implant design, chemical composition, implant surface topography, and implant surface treatment [107]. The host bone status is also an enhancing factor and its healing properties [108], as well as the stability of the mechanical loading conditions exerted on the implant [109].

Factors that hinder osseointegration can be the intensive mobility and micromotion in the implant [110], inadequate porosity of the implant coating [111], radiation therapy and the use of some pharmacological agents [112].

Factors related to the patients can also inhibit the osseointegration process like osteoporosis, advanced age, rheumatoid arthritis, nutritional deficiency, renal insufficiency and smoking [113], [114], [115].

Another crucial factor that affects osseointegration is the material biocompatibility, and it can play a significant role in predicting the osseointegration performance. Its importance comes from the idea that in the contact area between the bone and the implant, it is preferrable not to have any fibered tissue at the interface [116].

Titanium is one of the most used materials in the field of orthopedics, and that is due to its high biocompatibility, resistance to corrosion, and the low level of toxicity. An oxide layer constitutes part of the Titanium's surface, and it provides the capacity to self-repair via reoxidation when any damage happens [117].

2.4.5 Effect of lattice structures on osseointegration

As discussed in the previous chapter, osseointegration is a complex process that can be affected by many factors, and since the lattice structures affect many of the biomechanical properties of the implant, they can have a great effect on the osseointegration as well [118]. Since lattice structures have that effect on the bone ingrowth into the bone, their properties like porosity, unit cell topology, shape and pore size can strongly affect that process in their turn [119], [120], [121].

Arabnejad et al. studied samples chosen from two lattice structures, Tetrahedron and Octet truss, where the parameters were selected based on a limited area that suits the osseointegration process. This limited area of selection was set by many previous experiments [30], [122]. This selection area states, for Tetrahedron type of lattice structures, that the size of the pore be in

the range between 50-800 μm [123]. As shown in the next Figure 16, the design limits are exhibited with the red lines.

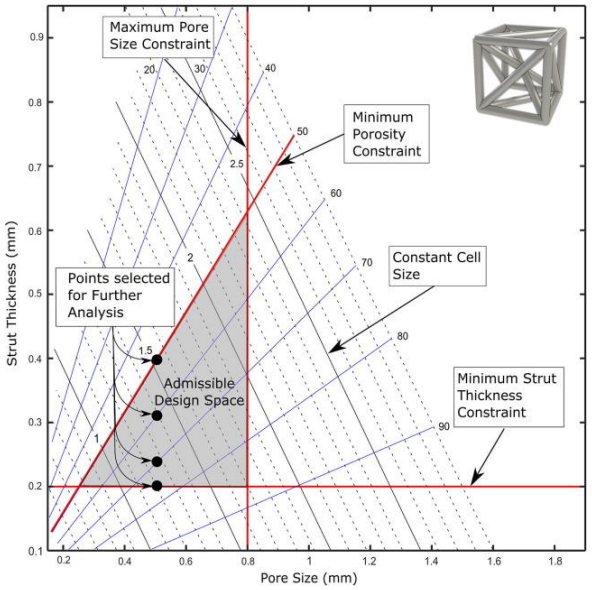

Figure 16. Design limits for Tetrahedron topology [124]

However, for the Octet truss lattice type, the limits for designing were 400-800 μm for the size of the pore, 50% for the porosity and a thickness ranging between 200-400 μm, as shown in Figure 17.

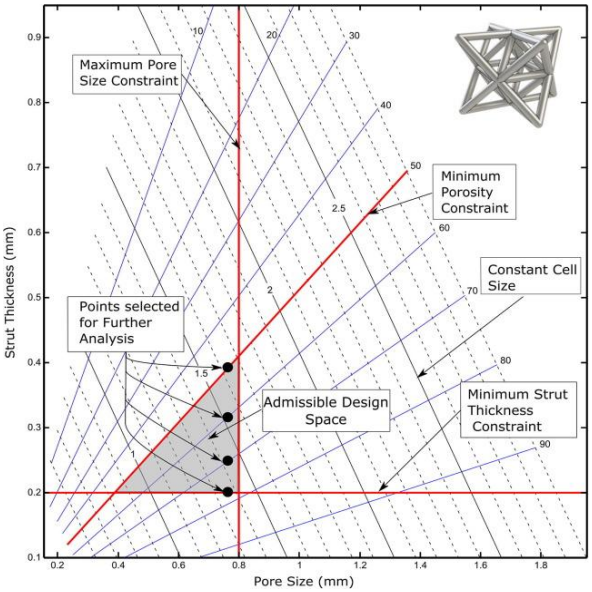

Figure 17. Octet truss design limits [124]

Generally speaking, titanium implants optimized via lattice structures for a better bone ingrowth should have special shape and dimensions of pores because all of that affect the osseointegration properties of the implant [125]. Researchers usually try finding the optimum combination between the pore size and the strut thickness to produce implants having a certain porosity level that facilitates the osseointegration; hence boosting the fixture of the implant into the bone. Based on the literature concerning the implant osseointegration levels, the best results for bone ingrowth with lattice structures in use can be achieved with the following ranges 500–750 μm, 200–500 μm, and 50–90%, for the pore size, strut thickness, and porosity, respectively [126].

Yet, there is no clear set of parameters for an optimum pore size. This is because of the fact that for every type of bone in the body, there exists certain biomechanical properties. Thus, every type of unit cell should be inspected to be in the optimum pore size that will produce an implant structure that matches that specific bone.

2.5 Additive Manufacturing (AM)

Additive manufacturing is a method of manufacturing during which the raw materials like plastic, powder, or metal are layer-by-layer deposited to build the 3D model up from a Computer Aided Design (CAD) model. This technique differs from the conventional manufacturing methods that depend on removing materials out of the raw materials to get to the required shape [127], [128].

Applications of AM have been enormously increasing in the orthopedics field. Many biomedical devices, tools, implants, and prosthesis have been manufactured using AM techniques. AM has gained this wide-spread usage with manufacturing due to its ability to manufacture complex shapes with high precision. It provides a very flexible solution in the orthopedics field where the desired shape and size for the implants can be manufactured as per demand, and it can help create any customized design no matter how delicate and complex it is [129]. This ability comes from the fact that AM uses layer-by-layer building of the geometry of the model under manufacturing. Moreover, using AM with expensive materials and alloys such as titanium alloys can save cost to a high extent. AM can be described as a method that facilitates the surgeon's work and increases the success rate, not to mention that it provides a great patient-specific implant with unlimited geometric freedom [130].

The AM, however, has many techniques to handle the manufacturing process. Much research has been done in order to select the suitable AM technique for the type of materials used in the orthopedics field. Power Bed Fusion PBF methods and techniques, such as Electron Beam Melting (EBM), Selective Laser Melting (SLM), and Direct Metal Laser Sintering (DMLS), are a good match for the manufacturing of implants of titanium alloys, and that is due to the high quality direct manufacturing method they use [131]. Liu tried to compare three AM techniques: selective laser melting SLM, directed energy deposition and electron beam melting (EBM) (SLM) and (DED) proved able to produce

structures that have 100-200 MPa higher yield and tensile strength when in comparison to EBM [132]. Two main AM techniques are discussed within this thesis, the SLM process since it is one of the most used techniques with metal biomaterials, and the DMLS since it is perfect to use with lattice structures made from titanium alloys and was used hereafter within the research done in the field.

SLM was first developed for laser technology in Germany in the 1990s [133], and has been adopted in many industries due to the ability to manufacture fully dense and functional products directly from metallic materials without the need for an intermediate binders or any additional processing methods [134].

Within the SLM process, a film of powder is spread on the build substrate. Then, the laser beam melts the powder following the shape to the desired geometry. In the next stage, a recoater applies the next film of powder using the already solidified part as the new basis. Because of the short reaction time between the laser beam and the powder, the cooling and heating ratio are high within the SLM process. The mechanical properties of components made by the SLM are totally different from those manufactured using the conventional methods due to the difference in manufacturing principle [135].

The development of AM has one main goal, and that is to fabricate three-dimensional complicated products directly from metallic powder via the CAD model. The laser sintering technique is one of the manufacturing techniques that is able to create metallic prototypes. There happens to be two types of laser sintering techniques that can process metallic powders via sintered laser:

The first one: Indirect laser sintering which is a technique that is not widely used with industrial applications due to the necessity of post-processing procedures needed and for the fact that most products manufactured with this method have a relatively low-density.

The second technique is the Direct metal laser sintering: which can be defined as a new additive manufacturing technique based on laser, and it was developed by the Rapid Product Innovation (Rusko, Finland) and EOS GmbH (Munich, Germany). DMLS is a developed laser-based manufacturing technology that uses data from a 3D designing software in order to build a component using layer-by-layer solidification. The process is initiated with the application of a thin layer of metallic powder on a platform called the building platform.

As exhibited in Figure 18, a high-energy laser beam scans the pattern described by the designer. The beam fuses the powder with the laser optic after each layer is executed. At the same time, the building platform continues to lower and the recoater spreads the powder on the platform thereafter. The DMLS technique operates with liquid-phase sintering to create a bond among the particles [136]. The flexibility of the feedstock and the shapes it produces can offer a suitable solution for producing complicated parts with comparison to the traditional methods [137].

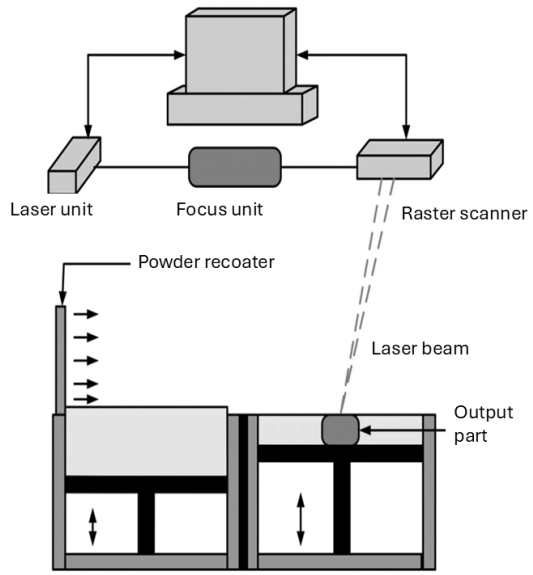

Figure 18. schematic graphic of DMLS process [136]

Figure 19 shows some of the parts manufactured using DMLS technology.

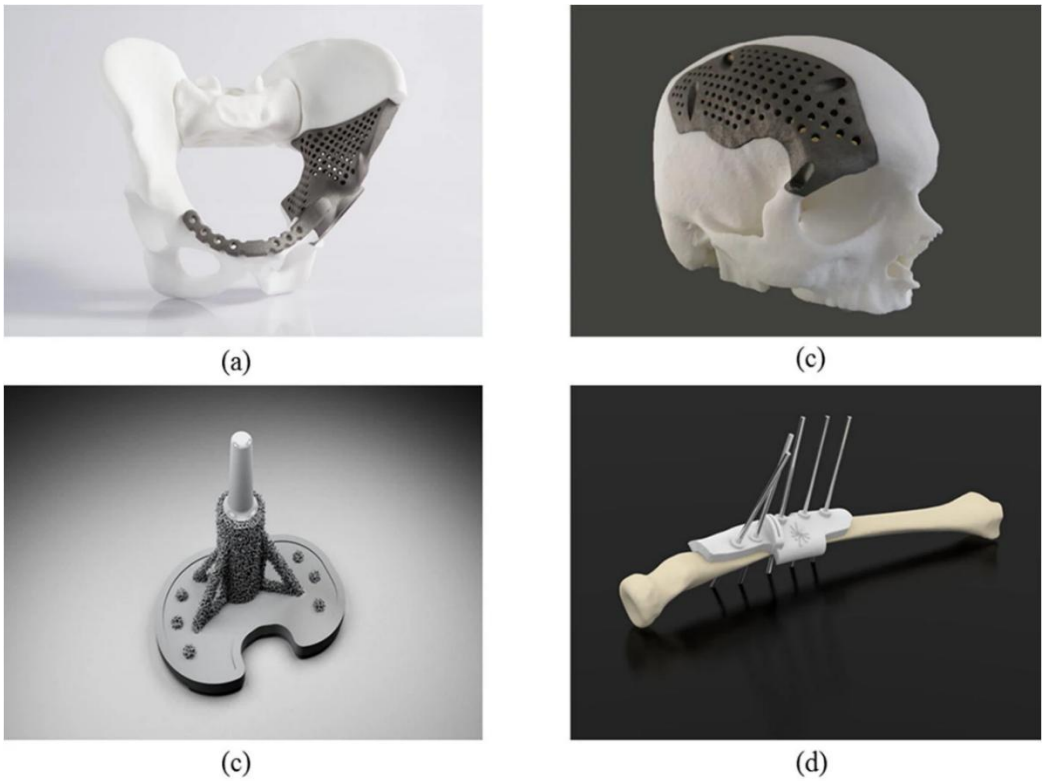

Figure 19. Parts manufactured via DMLS. a) hip implant, b) skull plate, c) Ti knee implant, d) rendered Drill guide to support stability in bone geometry [136]

As can be seen, the additive manufacturing techniques have facilitated the manufacturing of lattice structures. In our research, 3D-printer that uses DMLS technology was used to manufacture the designed specimens and implants for lab verification.

2.6 Finite element analysis in biomechanics

Due to the extremely large expenses that come with the using methods of additive manufacturing, the need for simulating the design results was a big necessity. Especially for the lattice structures complex design, and to avoid extra time and cost with manufacturing the implants of the body and then

experimenting on them and then applying the changes with the redesigning process, Finite Element Analysis (FEA) stepped in to help explore the behavior of the lattice-structured design which helps reduce the time in the manufacturing process and the costs of the prototype manufacturing [138].

FE can be used to simulate the real laboratory reaction of lattice structures and view the initial insight into the designed implant behavior. However, many studies confirmed that there would be a deviation when comparing between the laboratory tests and the simulated computerized results.

FEA has been of useful assistance to biomechanical designers where it helped define the critical regions of fractures, fatigue, strains, and mechanical stress that all can affect the longevity of the hip implant. Another crucial advantage of the FEA is that it can give an accurate estimate on the number of cycles a hip implant can bear before failure or yield [139].

Despite the fact that results might have some error between the real-life reaction and the computerized simulation, Zheng stated that there exists an agreement in overall results. His study investigated many lattice-structured with various shapes and porosities. The findings offered a prediction on the biomechanical properties and how the Young's modulus was affected by the relative density [140]. Helou et al. investigated the validation of lattice structures with both the finite element analysis and the experimental laboratory test. The experiment showed some differences between the two results [138].

With the help of FEA and the ANSYS software, Ghani [141] was able to calculate the elastic modulus of lattice structured samples printed with the SLM process. The study supported the principle of using FEA in the investigation of the distribution of stress within the three-dimensional model of human implant.

FEA was also used in an in vivo study on functionally graded lattice structures where the optimal design for the hip implant topology was created after estimating the stress behavior related design parameters. The study showed that the designed hip implant was able to bear the real life loads applied [141]. The FEA supported Gok with the reduction of the stress' maximum values by 25.89% which were related to multi-lattice structures applied to the hip implant design.

Over the past few years, FEA has been extensively used to evaluate the biomechanical and biotribological properties of knee and hip implants performance under static conditions. Maxian et al. was able to calculate the contact pressure of metal-on-metal and metal-on-ultrahigh molecular weight polyethylene hip implants with the use of Abaqus software [142]. Besong et al. [143] succeeded in predicting the pressure of metal-on-metal contact type of hip implant with the use of FEA. Kang and Liu [144] estimated the volume of wear caused with metal-on-UHMWPE in hip implants depending on the area of contact calculated using the FE method.

In trial to optimize the hip implant, Anthony et el. in [145] tried to perform FEM simulation on several hip stems. The study aimed to show a comparison of the von Misses stress between each of the designed stems along with the displacement. Their study used 3 different materials: Cr-Co-Mo Stainless Steel SS316L and Titanium alloy Ti6Al4V. The cross sections of the hip implant in the study were distributed among four different ones: Circular, Elliptical, Trapezoid and Oval.

Three hip profiles were used in the experiment, for each hip profile, the four cross sections were tested. The hip implants were bounded and loaded in a way that imitates the real boundary conditions and loads that the hip implant usually withstands. The research showed that Ti6Al4V has the lowest stress values compared to those of CoCr and 316L SS.

2.7 Implant optimization

Researchers in the orthopedics field have always studied the structure of the medical implant to be able to achieve better biomechanical properties and manufacture implants that can match need in the best way. Over the years, scientists have classified optimization into three different kinds of optimization: Shape optimization, size optimization and Topology optimization (TO) [146]

TO can be defined as a mathematical technique that can rearrange flow of materials in order to achieve the required properties while maintaining the necessary constraints, and, at the same time, is capable of using the trial-and-error principle to provide a useful designing tool [147].

In its early stages, TO was used mostly with the mechanical design in the aviation field in order to optimize the distribution of material on the average structure [148]. Starting from the 1980s, TO has been considered a useful technique that can be applied to improve the design of biomedical implants [149]. In most cases, the results of topologically optimized structures are complex designs that used to create a big challenge for conventional manufacturing methods to fabricate. In the current up-to-date AM techniques, the limitations in manufacturing were overcome, and the number of topologically optimized orthopedic implants with better biomechanical properties have increased over recent years.

Within the FEA process, TO offers a developed technique to functionally improve the mechanical properties by redesigning the material's distribution in a specific domain. This distribution is based solely on the loading exerted and the constrained boundary conditions [150].

In the orthopedics field, the main aim of the majority of research is to improve the implants into implants that has low strain energy which can be defined as

the energy stored in a body when certain work or load has been exerted on it [151]. Li et al. stated that TO can determine whether the element under the FEA possesses enough stress, and when the answer is no, the element would be adjusted or removed in order to improve the overall efficiency [152]. Nowadays, FEA software like Abaqus (Dassault Systems, USA), Hypermesh (Altair Engineering, Troy, MI) and Ansys (Ansys, Inc., USA) are able to perform the total iterated topology optimization operation using some specialized algorithms.

In order to prove the manufacturability of the new TO design, the resulting part was 3D printed. The investigation was a classic example on how TO was moved from theory into practice and proved that the TO use with the biomedical implants is of great use [153]. Porous structures were also applied to the local microstructure according to the TO design with different material's density.

Topology optimization might impose some complications on the design since it changes the material's distribution by editing the material's flow into the structure. In order to get the desired porosity out of the lattice structures' parameters, and since there is not yet any obvious equation that dictates the relationship between the topological optimization and the parameters, many trial-and-error experiments are usually done in order to reach to the desired and/or optimum results when designing a lattice-structured implant. This conclusion has led to the fact that machine learning (ML) can step to offer some help in processing the manipulation in parameters since it can handle the randomness of the designing parameters and their effect on the resultant structure. ML can also process complex numerical analysis if necessary. Yet, the only downside of using the ML methods is that it might, sometimes, be time-consuming due to the complexity in the code [154].

Some trials have been made to apply the ML techniques into the lattice generation and the results improved efficiency to an acceptable extent. A study

used the autoencoder for the prediction of the mechanical properties of micro-lattice structure with the help of an encoder and generated micro-lattices with the desired mechanical properties by using the decoder [155].

The machine learning regression application was used by Mesut and Fatih [156] to get the metrics of performance for the heart sound data. They utilized many classification techniques such as: Decision Trees, Naive Bayes, Support Vector Machine (SVM). Whereas Nur [157] performed a comparison between several machine learning models: SVMs, regression models, and ANNs in the prediction of three output variables. Root Mean Square Error (RMSE), Mean Square Error (MSE) and R^2 coefficient were used to evaluate the model's accuracy.

Neural network (NN) technique was also applied to create relationships between the traditional triangular lattices and their elastic properties for a better design of architectured anisotropy-tuned lattice structures [158]. NN was also used to establish data-driven inverse design where the desired properties to be an input for the model and the output to be the design parameters of the latticed materials [159]. In order to predict the mechanical properties of aniso-truss lattices and to help with calculating sensitivity analysis, NN with single layer was applied to a designing model [160].

In another research paper, 57 samples were collected from various studies, and a support vector machine (SVR) model was applied to anticipate the biomechanical properties of lattices. The target properties of designs were the elastic modulus, porosity, unit cell length and the material's density. The investigation generated a model that was able to set the designing parameters in a way that they produce the required properties required [161].

Guoji et al. used the stress-strain graphs that were obtained from FEM and used the results as training data for an artificial neural network (ANN) that could refine the FEM prediction. This study was able to expand the design range of

the generated lattices with the required properties. They concluded that heterogeneous lattices with specific responses can be obtained with the help of deep learning DL methods [162].

Deep learning was also used to generate a reverse design of graded lattices in order to attain a multiscale design built on two methods, the topology optimization and the neural networks together. The built system improved efficiency in time for the creation of high-performing structures with quick design process that takes up to 2 seconds and was able to prepare a reference for the TO design of lattices. The study also confirmed that using DL meta-structure design technique is more rapid than the optimization flow [163]

Three hidden layers were proposed in the deep learning neural network DLNN technique used with the data. The input layer was represented by the orientation angle, the diameter, and the struts length. The output layer was of three nodes with sigmoid function as an activation. The output results were the specific strength, the Young's modulus and the ultimate strength. Fifty neurons composed each of the hidden layers. Hidden layers used the same size based on the suggestions from [165] because of the convenience it produces when applying the relative technique. The Activation function was Swish to activate the first hidden layer, whereas the second and third layers were activated with a rectified linear unit (ReLU).

Chapter 3: Mechanical properties of Ti6Al4V

3.1 Experiment setup

The mechanical properties of the Ti6Al4V are important to be defined in order to guarantee accurate results in both the simulation and the lab validation. The most important mechanical property when dealing with a certain material is the Young's modulus, i.e. how elastic the material is.

The designing software used in the experiment is the ANSYS software version 2020 R2 (Canonsburg, PA, USA). Ansys SpaceClaim was used for the CAD design of the models, and Ansys Workbench was used for the static simulation of the compression test. 3D-printing of the specimens to be used in this experiment was performed using EOS M290 (Electro Optical Systems, Munich, Germany) machine that uses direct metal laser sintering technique. The machine is equipped with a laser head type Yb fiber with 400 W power. The focal diameter of the machine is 100 μm whereas the scanning speed is 7 m s^{-1} [166]. Mitutoyo digital caliper with a precision of ±0.02 mm was the main measuring tool to precisely check the heights and diameters of the specimens.

The compression test was performed using INSTRON 8801 servo-hydraulic fatigue testing machine as per ISO 13314 Standard. A video extensometer device was installed on the testing machine that was equipped with a high-resolution camera in order to register any change in the displacement throughout the experiment. The chemical composition of the TI6Al4V alloy used in the research's experiments is shown in Table 1.

Table 1. Chemical composition of Ti6Al4V

Element	Chemical composition percentage %
Al	5.50 - 6.50
V	3.50 - 4.50
O	0.13
N	0.05
C	0.08

H	0.012
Fe	0.25
Y	0.005
Other elements each	0.1
Other elements total	0.4

A quick experiment was performed in the lab in order to determine the exact Young's modulus that the specimens have after being 3D-printed. Three cylindrical samples were CAD designed and then 3D-printed, as shown in Figure 20, using the same titanium alloy.

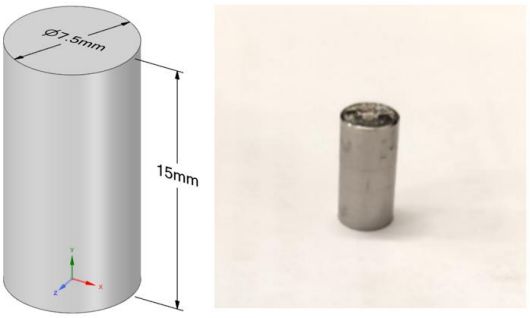

Figure 20. Specimen for compression testing

The samples were then tested on compression and finite element analysis was performed with the use of Ansys software to validate the results through the comparison between simulative and laboratorial results. The reason behind the extra check with this experiment is to determine the exact Young's modulus of the material being dealt with. If the nominal value is inserted in the software, then the laboratory value of the material might be different, and that is due to the 3D printing accuracy, quality, and the material's quality. Young's modulus was calculated with Equation 2.

$$E = \frac{\sigma}{\varepsilon} \tag{2}$$

Where E is the young's modulus in MPa, σ is the stress which resulted from the force over the area of the sample's cross section. ε is the strain resulted from the change in height of the sample. In the FEM analysis the stress and strain

values were calculated through the Ansys Workbench software, and in the laboratory, the same variable values were extracted from the compression machine. The compression test was performed with a loading speed of 1 mm/min. The test was monitored also using a video extensometer which is provided with a high-quality camera that can detect changes in displacement all through the compression experiment. Figure 21 shows the compression test set up and the FEM process parameters.

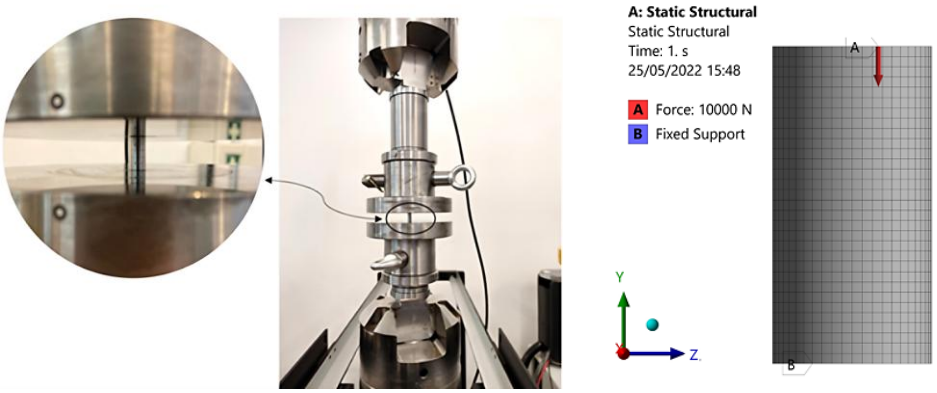

a b

Figure 21. a) Compression test, b) FEM

3.2 Compression test results

Using the video extensometer, the strain values resulting from the applied displacement were registered throughout the experiment. As for stress values, they were calculated using the reaction forces registered by the testing machine. Figure 22 shows the stress-strain values for all specimens.

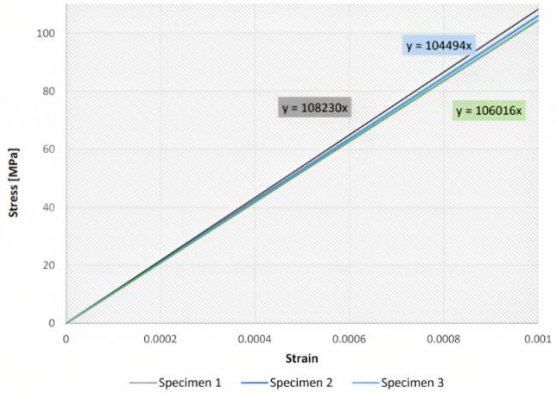

Figure 22. Stress-strain values

As per the graph above, Young's modulus average result is 106247 MPa, which is 6% deviated from the nominal value that is 113800 MPa.

3.3 FE analysis results

In order to perform a comparison between the simulative compression test and the lab experiment, the Young's modulus calculated in the lab experiment was applied into the simulation investigation setup. The simulative test was performed within the elastic range of the material. Mesh convergence analysis for the deformation results was conducted to guarantee an accurate simulation process. The deformation reaches a convergence with a change less than 5%. Figure 23 shows the mesh element size against deformation in the convergence study.

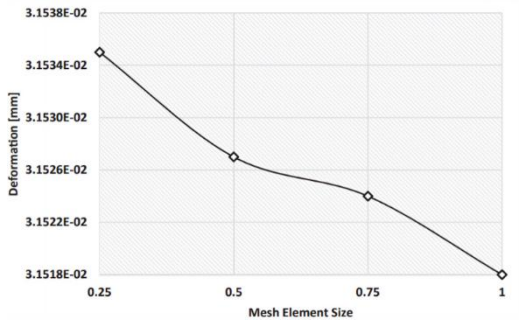

Figure 23. Convergence study

Figure 24 shows the stress-strain results for the simulation test. A value of 108151 MPa was obtained for the Young's modulus which is also close enough to the nominal value of the Ti6Al4V alloys. The deviation from the nominal value registered 4.9%. Nominal value, simulative value and the lab value of the Young's modulus were shown in the figure as well.

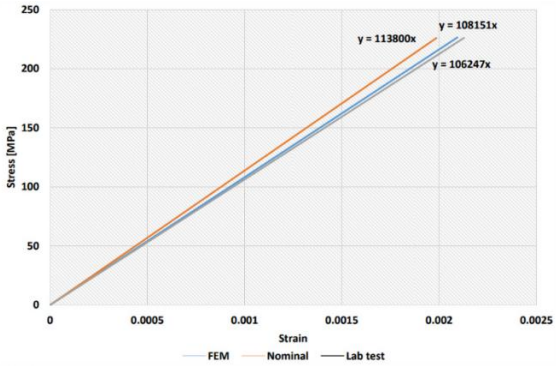

Figure 24. Stress-strain graph and Young's modulus values

The deviation between the three values can be attributed to many reasons and can be summarized by the following: The accuracy of the 3D-printing process, the quality of the 3D-printing process and the quality of the material used. Young's modulus defines the elasticity of the material, and since the Ti6Al4V alloy's Young's modulus is still bigger than the bone's elasticity range, lattice structures can be implemented into the design to reduce the stiffness of the material and approximate the alloy's Young's modulus to the bone's range as will be performed in the following chapters.

Chapter 4. Designing and manufacturing lattice structures

4.1 Latticed design

Now that the material's stiffness is defined accurately, and before the complete implant is designed, three types of lattice-structured specimens are to be created for the next phase of compression testing. Before moving on to the compression tests on the specimens, this chapter investigates the shape and dimensional accuracy of the manufactured titanium lattice structures.

The specimens were designed using SpaceClaim within the ANSYS software 2020 R2. The specimens' dimensions are 20 × 20 × 30 mm. Within the SpaceClaim software, two main parameters are needed in order to define the latticed structure:

- The length between the adjacent unit cell's centers, or simply, the length
- The thickness of each beam connecting the unit cells, or simply, the thickness

The latticing was implemented in the middle volume of the total specimen, where a 20 × 20 × 20 mm volume will be latticed in order to leave an upper and lower 5 mm solid volumes that will facilitate the later lab compression test by being compressed between the machine's two compression plates. Figure 25 shows the lattice details on the first type of lattice structures.

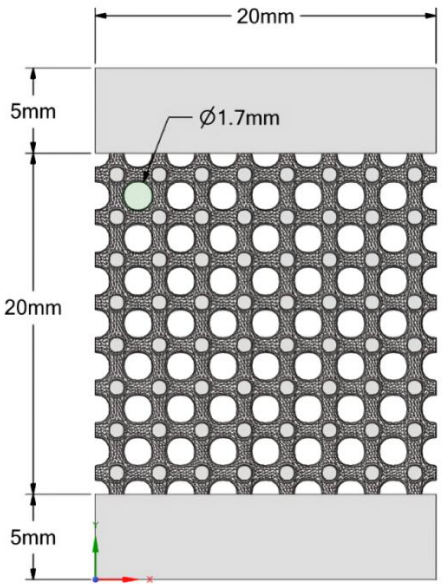

Figure 25. Dimensions and lattice details

4.2 Lattice structure's specimens manufacturing

Latticing was applied to the three chosen types of lattice structures with parameters that generate similar values of porosity within all types for the sake of making an accurate comparison between the reactions for all types. Figure 26 shows the three 3D-printed types of lattice structures. The manufacturing process produced three specimens of each 3D-printed type. The three types of unit cells are: 3D lattice infill pattern, double-pyramid lattice with cross, and octahedral lattice 2.

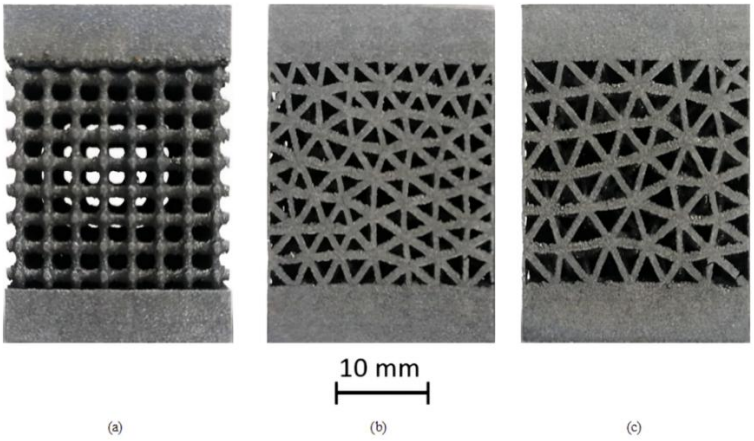

Figure 26. 3D-printed specimens(a) 3D lattice infill pattern, (b) double-pyramid lattice and face diagonals, (c) octahedral lattice 2 [167]

The unit cell parameters for the three lattice structures are shown in Table 2.

Table 2. Lattice structure's parameters

Unit cell type	Thickness (mm)	Length (mm)
3D lattice infill pattern	0.7	1.7
Double pyramid lattice and face diagonals	0.7	3.5
Octahedral lattice 2	0.7	3.8

Figure 27 shows a visualization on the lattice geometry for each type of lattices.

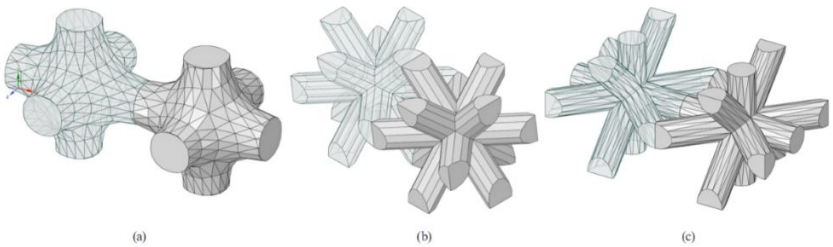

Figure 27. Lattice structures geometry: (a) 3 Dimensional Lattice Infill Pattern, (b) Double pyramid lattice and face diagonals, (c) Octahedral lattice 2 [167]

4.3 Results

The samples' dimensions were measured, and the masses were weighed. The average values are shown in the next Table 3.

Table 3. Average measurements of the 3D-printed specimens

Unit cell	Average length (mm)	Average width (mm)	Average height (mm)	Weight (g)
3D lattice infill pattern	19.99	19.97	30.29	26.61
Double pyramid lattice and face diagonals	19.96	20.03	30.24	28.34
Octahedral lattice 2	20.04	20.03	30.26	28.44

For the evaluation of the 3D printing outcome, all three types of lattice structures (3-Dimensional Lattice Infill Pattern, Double pyramid lattice and face diagonals and Octahedral lattice 2) were reviewed and inspected. After having measured the dimensions and mass of the specimens, an accuracy check was performed using the GOM ATOS high-speed scanning system available at the University of Debrecen, faculty of Engineering, 3D laboratory. The scanning process performs a precise measurement and detailed resolution via the structured blue light system [168]. The printed specimens were put in comparison with the designed CAD files in order to pinpoint the deviation between the designed and printed accuracy. Table 4 exhibits the comparison between the measured and nominal data for the three lattice structures.

Table 4. Measured vs nominal data comparison [167]

Specimen	Length [mm]	Width [mm]	Height [mm]	Mass [g]
Mean (specimens)	19.99	19.97	30.29	26.61
Std. Deviation	0.04	0.03	0.05	0.14
Nominal Mean (CAD model)	20.00	20.00	30.00	26.93
Error (Nominal, Specimens)	0.01	0.03	0.29	0.32
Max deviation	0.080	0.060	0.347	0.510

Max deviation percentage (%)	0.400	0.300	1.156	1.894
3-Dimensional Lattice Infill Pattern				
Mean (specimens)	19.96	20.03	30.24	28.34
Std. Deviation	0.04	0.06	0.03	0.10
Nominal Mean (CAD model)	20.00	20.00	30.00	28.70
Error (Nominal, Specimens)	0.04	0.03	0.24	0.37
Max deviation	0.073	0.127	0.273	0.460
Max deviation percentage (%)	0.367	0.633	0.911	1.602
Double pyramid lattice and face diagonals				
Mean (specimens)	20.04	20.03	30.26	28.44
Std. Deviation	0.07	0.08	0.06	0.04
Nominal Mean (CAD model)	20.00	20.00	30.00	29.00
Error (Nominal, Specimens)	0.04	0.03	0.26	0.58
Max deviation	0.133	0.163	0.333	0.590
Max deviation percentage (%)	0.667	0.817	1.111	2.033
Octahedral lattice 2				

For the first type, the 3D lattice infill pattern, the deviation of the dimensions was a maximum of 1.15% in the height, while the mass deviation was higher to 1.89%. The printing inaccuracy also caused a decrease in the width and length.

On the other hand, the Double Pyramid lattice and face diagonals type had an average deviation in the length of up to 0.36% and in the width of up to 0.63%. Its mass deviation is less than the previous type with a percentage of 1.6%. As for the Octahedral Lattice 2 type, the deviations are higher compared to the other two types. Mass deviation was 2.03% of the designed value, and the dimensions deviation highest value was in width terms with a percentage of up to 0.8%.

Since porosity results from the change of the hole size which is considered a major variable in determining the osseointegration rate, the porosity values were calculated, using Equation 3, for each type of specimen under investigation.

$$P\ (\%) = \frac{V_{bulk} - V_{lattice}}{V_{bulk}} \cdot 100 \quad (3)$$

Where P is the porosity, $V_{lattice}$ is the latticed structure volume, and V_{bulk} is the volume of the total bulk block. Table 5 shows the porosity calculation and the variance between the nominal and real values. The highest deviation in the porosity values was of the Octahedral lattice 2 where the scored deviation was 2.93% from the nominal value. The rest of the types, however, showed a close percentage of around 2% in maximum.

Table 5. porosity values, deviation vs real values

Specimen	3D Lattice Infill Pattern	Double pyramid lattice and face diagonals	Octahedral lattice 2
Mean porosity(specimens) %	75.18	70.39	70.23
Std. porosity %	0.37	0.23	0.16
Nominal porosity %	74	69	68.4
Error	1.183	1.394	1.835
Deviation percentage %	1.60	2.02	2.68
Max deviation	1.72	1.74	2.00
Max deviation percentage (%)	2.33	2.52	2.93

Figure 28 shows the deviation and the relative error for dimensions, masses, and porosities of the printed specimens.

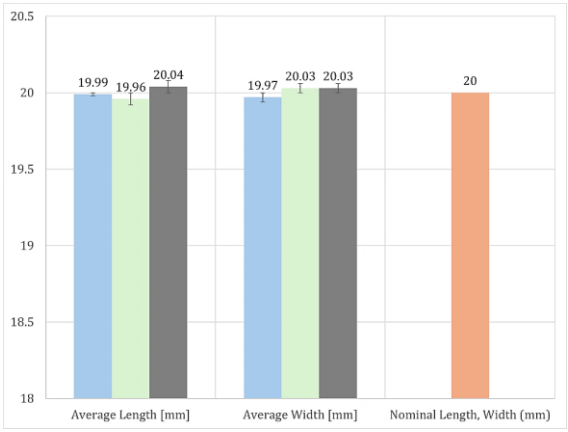
20.5
20
19.5
19
18.5
18
19.99
19.96
20.04
19.97
20.03
20.03
20
Average Length [mm]
Average Width [mm]
Nominal Length, Width (mm)

a

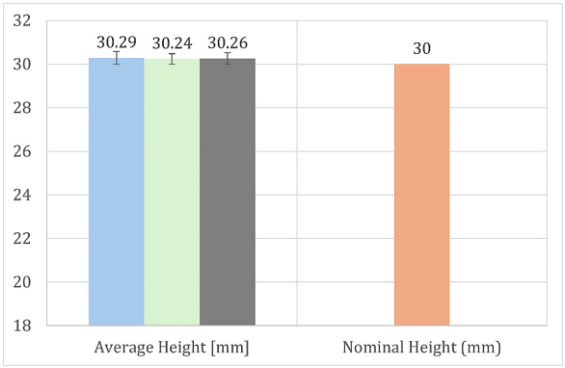
32
30
28
26
24
22
20
18
30.29
30.24
30.26
30
Average Height [mm]
Nominal Height (mm)

b

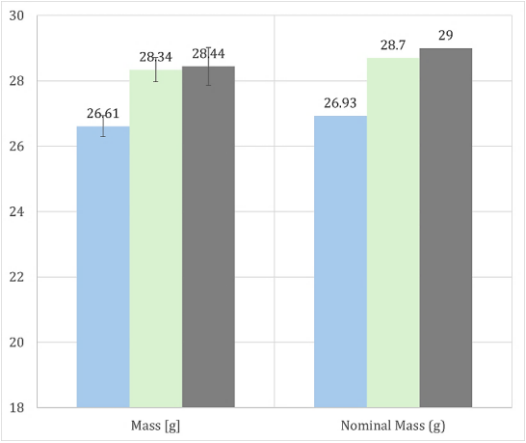
30
28
26
24
22
20
18
26.61
28.34
28.44
26.93
28.7
29
Mass [g]
Nominal Mass (g)

c

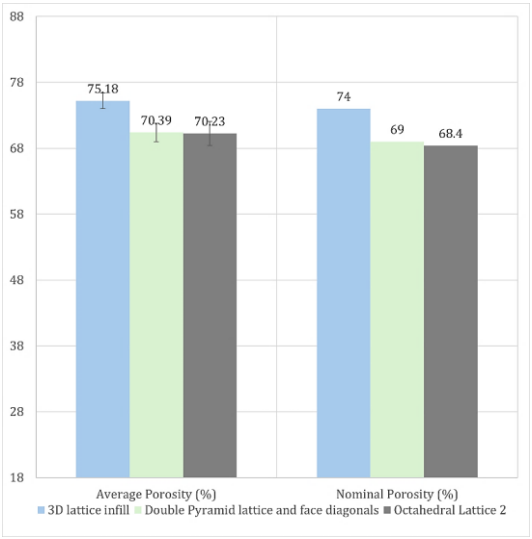

d

Figure 28. The deviation in values between CAD design's dimensions, masses, porosities and the printed specimens'. a) variance in Length, width, b) Variance in Height, c) Variance in mass, d) variance in porosity [167]

Figure 29 shows the results of scanning the specimens. Areas in green represent the inappropriate distribution of material, whereas areas in red color mean the density of material is higher than normal, and areas in blue color represent the low density or loss in material's distribution. Due to the direct relationship between the 3D-printing accuracy and material's distribution, the figure lists the dimensional accuracy next to the areas of material's distribution for a clearer comparison along the height of the specimens. The range for accuracy on the height axis varies by a unit of ±0.15 mm.

As seen in Figure 29, there are some fluctuations on the Octahedral lattice 2 that totally supports the results of accuracy on its dimensions, where the complexity of this type's shape played a significant role in producing, to some extent, inaccurate results. Among the three cases, the high level of material's distribution is concentrated on the areas of connections between the bulk and latticed part of the specimen.

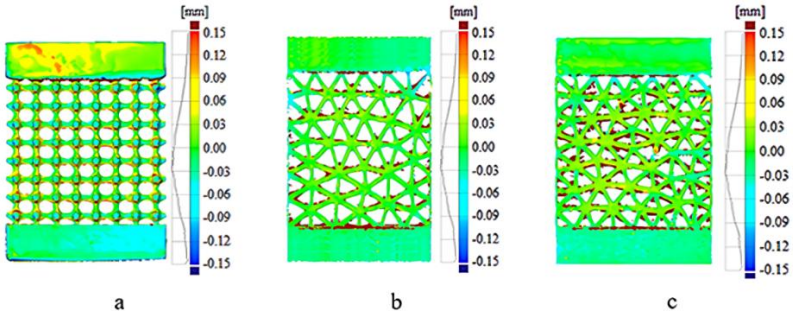

Figure 29. Scanning results for: a) 3-Dimensional Lattice Infill Pattern, b) Double pyramid lattice and face diagonals, c) Octahedral lattice 2 [167]

For better results and since the specimens are prepared to go through compression tests after having been 3D-printed, the heights of all specimens were leveled using milling machine available at the machining lab at the engineering faculty, University of Debrecen. The final height for all specimens was set to 30 mm. The upper and lower surface of the specimens are completely parallel where equal pressure can be guaranteed.

The study investigated three types of lattice structures to compare their designed geometries with their manufactured counterparts. For each structure type, six samples were fabricated using the EOS M 290 machine, which employs the Direct Metal Laser Sintering (DMLS) process. The key findings of the study are as follows: the dimensional accuracy in the XY plane was found to be higher than in the Z direction, which is attributed to the inherent precision of the printing system. The more complex the printed structure is, the lower the manufacturing accuracy will be. As the size of the printed object increases, a decline in accuracy occurs, potentially due to the machine's performance over prolonged printing durations. For better dimensional accuracy, it is advisable to use simpler unit cell geometries (e.g., basic 3D lattice infill types). 3D scanning and inspection revealed inconsistencies in material distribution. These fluctuations are influenced by factors such as laser scanning direction, laser power, and scanning speed during the printing process

Chapter 5: Lattice structures mechanical properties

5.1 Preparation of the specimens

Since the lattice structure application affects the mechanical properties of the implant's design, the purpose of this chapter is to determine the mechanical properties of the total structure after implementing the lattices into the 3D-printed specimens. The investigation takes place as a comparison between a simulative compression test done using FEM and a laboratory compression test. Effective Young's modulus values were calculated for all types of lattices in order to see how lattice structures could help reduce Young's modulus value to be as close to the human bone's stiffness as possible [169].

Four lattice structure types were drawn using SpaceClaim within ANSYS software 2020 R2. The dimensions of the lattices are 20 × 20 × 30 mm with a latticed middle volume of 20 × 20 × 20 mm, leaving two 5 mm upper and lower volumes to ensure homogenous distribution of compression under the machine's jaws. Table 6 shows the specimen's parameters with the porosity calculations as per Equation 3.

Table 6. Specimen's parameters

Unit cell	Porosity percentage (%)	Actual volume (mm^3)	Bulk volume (mm^3)	Beam thickness (mm)
3D lattice infill pattern	74	2079.17	8000	0.7
Double pyramid lattice with cross	74	2067.58	8000	0.85
Double pyramid lattice and face diagonals	71	2313.96	8000	0.6
Octahedral lattice 2	70	2431.76	8000	0.8

The four specimen types were manufactured using the same machine in the previous chapter, three specimens were manufactured of each type of lattices. Figure 30 shows the four manufactured types of lattices to be used in the study.

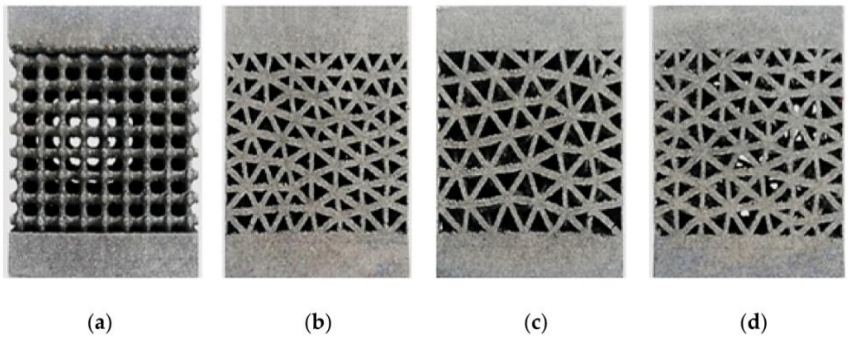

Figure 30. Lattice structures types: (a) 3D lattice infill pattern, (b) double-pyramid lattice with cross, (c) double-pyramid lattice and face diagonals, (d) octahedral lattice 2 [169].

5.2 Compression test and FE model

After the stage of manufacturing the specimens in preparation for the compression test, FEM analysis was used to validate the results. A comparison was performed to find the deviation between the cyber and actual results. In the compression test an INSTRON 8802 Servo Hydraulic Fatigue testing machine was used (Instron, Norwood, MA, USA) to perform the test. A video extensometer of type INSTRON AVE2 with a precision of 0.5% was also used during the compressing for the purpose of achieving precise measurement results of the displacement taking place within compression.

For full control over the process, Wave Matrix version 2 software (Instron, Norwood, MA, USA). To enhance the monitoring of the displacement happening on the specimens, the upper and lower bulk parts (5 mm thickness) of the specimens were marked with two white dots where they represent a reference for the video extensometer to be able to measure the strain. The displacement rate applied during the experiment was set to 1 mm/min. The maximum force

applied during the test reached up to 15kN in order to keep the results of the compression within the elastic range of the Ti6Al4V alloy used to print the specimens. There was no lubrication used during the experiment because of the fact that a very small sideways movement was anticipated. The total number of compression experiments was twelve quasi-static tests for three specimens of each type of the four lattices. Figure 31 shows the testing setup.

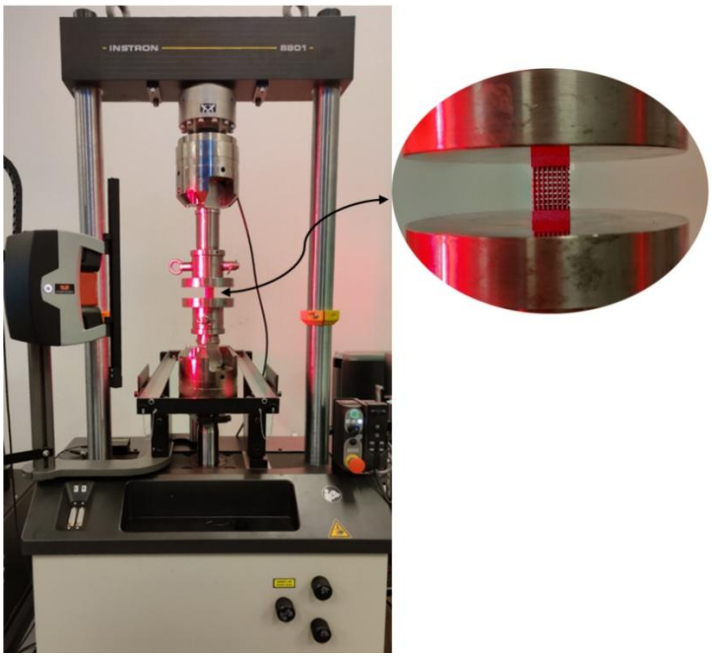

Figure 31. Compression test setup [169]

As a validation method, the FEM was performed with the help of ANSYS software R2 version 2020 (Ansys, Canonsburg, PA, USA). A complete simulation was performed with the same conditions mentioned in the laboratorial compression test. The loading force was 15 kN to be applied on the upper surface of the specimens. A fixed support was assigned on the bottom surface. The initial mesh default size was set to 2 mm. After performing a mesh convergence study as shown in Figure 32, the latest mesh size was set to 1.5 mm, which achieved a change of less than 1% for the average of all three types. With the applied mesh, the number of the elements reached a range between

500,000 and 700,000. In the Ansys software settings, the material's properties were set as described in the previous material's table 2.

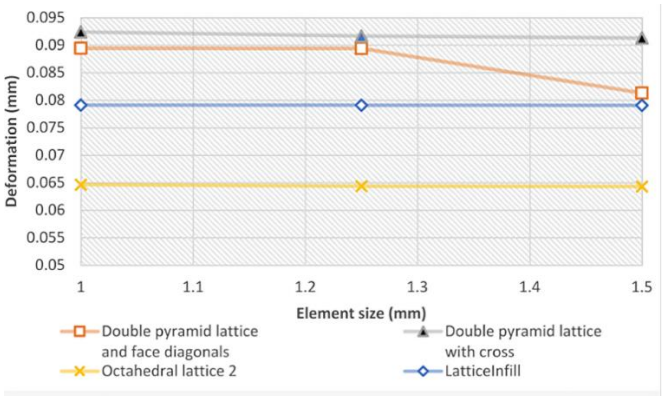

Figure 32. Mesh convergence study [169]

Figure 33 shows the simulation boundary and loading condition, taking into consideration that all types of unit cells underwent the same parameters and conditions of the process of the compression test.

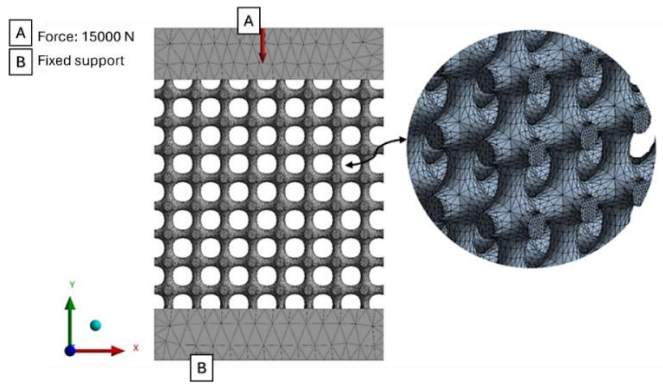

Figure 33. Simulation settings [169]

Stress-strain curves were drawn for the compression test results and each specimen's type was evaluated. As mentioned above, the compression was performed within the elastic region of the material, thus the relationship between stress and strain is completely linear.

5.3 Results

The results for laboratory compression tests are shown in the next Figure 34. Young's modulus was calculated and shown on the graphs.

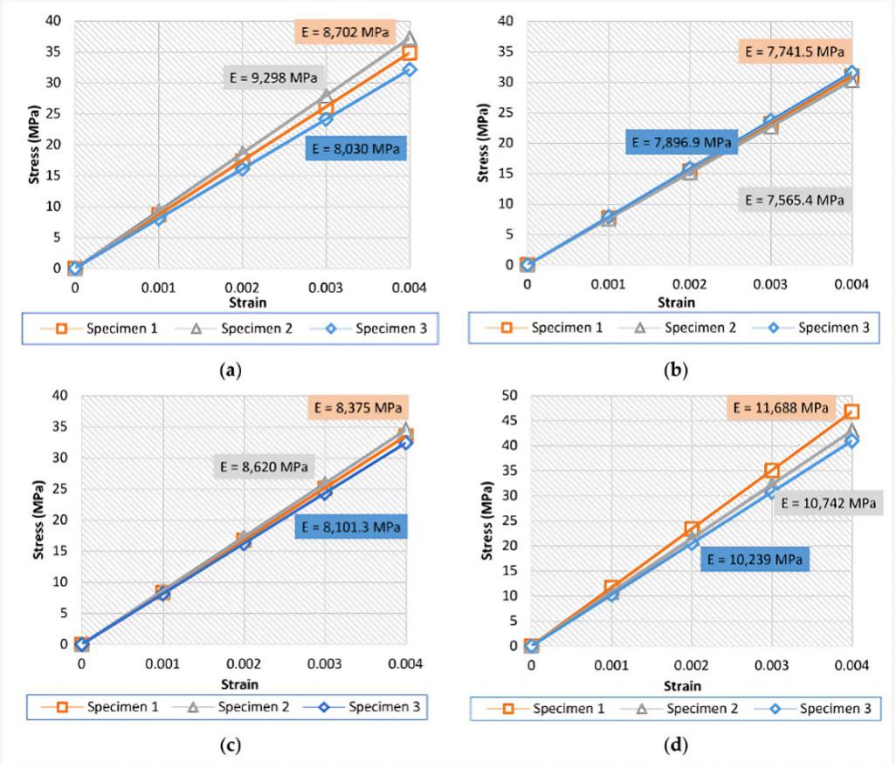

Figure 34. Effective Young's modulus: (a) 3D lattice infill pattern, (b) double-pyramid lattice with cross, (c) double-pyramid lattice and face diagonals, (d) octahedral lattice 2 [169].

As a main result of the research, the stiffness of the structure was reduced to a range of 80-90% with the application of latticed optimization. During the experiments, the load applied on all the types was of the same value, and since they all have the same area under the load, the stress will be the same for all types. The difference in value of the Young's modulus among all the types can be explained by the change in the strain values, which comes due to the fact that the reaction against the load for each type was unique and differs from the

other. The “Octahedral lattice 2” type showed the highest value of Young’s modulus which nominates it to be the stiffest type among the other types. On the other hand, the lowest value among the structures was for the “Double Pyramid lattice with Cross” type.

Figure 35 shows the results of the FEM analysis for all types of lattice structures, whereas the deviation between the laboratorial results and FEM results was shown in Table 7.

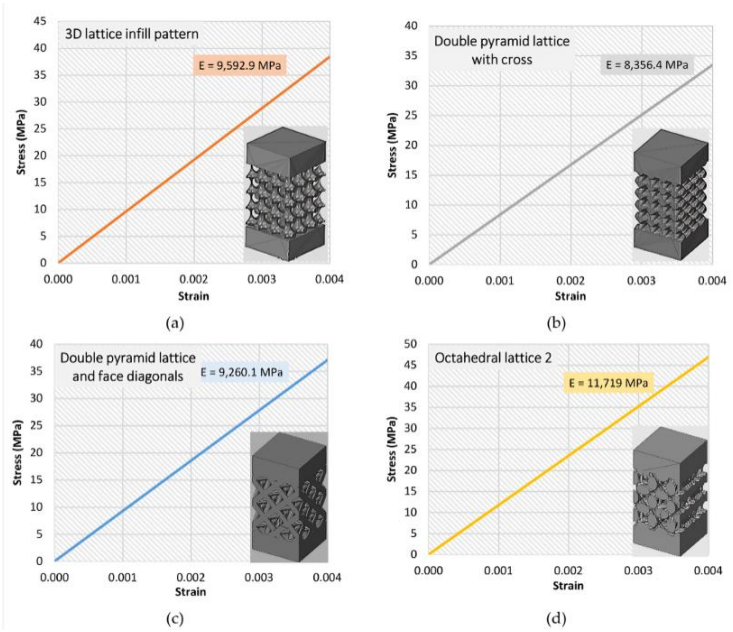

Figure 35. Young’s modulus FEM. (a) 3D lattice infill pattern, (b) Double pyramid lattice with cross, (c) Double pyramid lattice and face diagonals, (d) Octahedral lattice 2.

Table 7. Deviation in Young’s modulus values between numerical analysis and laboratorial results

Cell type	Effective Young’s Modulus (MPa) (measurement)	Effective Young’s Modulus (MPa) (numerical analysis)	Deviation %
3D lattice infill pattern	8676.67	9592.9	9.6
Double pyramid lattice with cross	7734.60	8356.4	7.4

Double pyramid lattice and face diagonals	8332.00	9260.1	10.0
Octahedral lattice 2	10889.67	11719	7.1

The deviation detected among the structures' Young's modulus reached up to 10% in the maximum case that happened at the Double Pyramid lattice and Face Diagonals. The reasons behind such a deviation might be related to one of the following results: The quality of the 3D-printing, the quality of the metal powder used within the printing process, the accuracy of the 3D printer and the compression test accuracy considering how accurate the machine is [169].

After examining these four lattice structures types with the focus on their linear elastic behavior within the compression tests, FE analysis was used to perform a validation of the experimental results. Based on the results, each type of lattice demonstrated a mechanical behavior that is suitable for specific type of the human bone in the hip implant area.

"Octahedral lattice 2" exhibited a high Young's modulus value of 11 GPa, which is close to the average modulus of mixed cortical/trabecular bone in the upper femur area that usually has a stiffness range of 10-12 GPa [170], [171]. The "3D lattice infill" and the " Double pyramid lattice and face diagonals" presented average values of 9 GPa, which is ideal in range for proximal femur cortical modulus where it can support the structural regions [171], [172]. The "Double pyramid lattice with cross" showed a low Young's modulus with a value of 8 GPa, which matches the compressive properties of the femoral head's trabecular bone in areas that require shock absorption [173], [174], [175]. This reduction in hip implant material's stiffness is crucial to align the implant's stiffness more closely to that of natural bone.

Chapter 6: Surrogate model Development

6.1 Lattice type selection

As mentioned previously, the Young's modulus for the Ti6Al4V material used in the research was measured in our previous article. According to the lattice structure kinds that were numerically examined and validated via compression tests to reduce the Young's modulus of the implant structure with the lattice structure application, the studies showed that every lattice structure type was specifically suitable for a certain type of implant to be inserted into the body.

However, the 3D lattice infill type was found to be a good choice for the hip implant optimization [169]. In this case study, the parameters for the lattice structures were chosen to be 0.6 mm for the length and 0.4 mm for the thickness, and since this is different from the parameters in the previous Young's modulus calculations, a numerical calculation for the Young's modulus and Poisson's ratio were performed in order to continue the FE simulation with the new suitable values. These parameters resulted in a porosity of 61% which helps enhance the bone ingrowth as proven in [124].

6.2 FE analysis setup

For the calculation, a rectangular specimen with 20×20×30 mm dimensions was designed in ANSYS SpaceClaim software version 2020 R2 (Ansys, Canonsburg, PA, USA), and the middle part of the specimen was latticed as 3D lattice infill type. A simulative compression test was executed using 2300 N force as stated in the hip implant testing standard 7206-04:2010 [176]. The fixed support was set to be on the lower part of the specimen. Patch-independent mesh method was applied to the latticed section with element size of 0.4 mm minimum. Element nodes were 248687 nodes, and the element number was 774817. The test setup is shown in Figure 36 below.

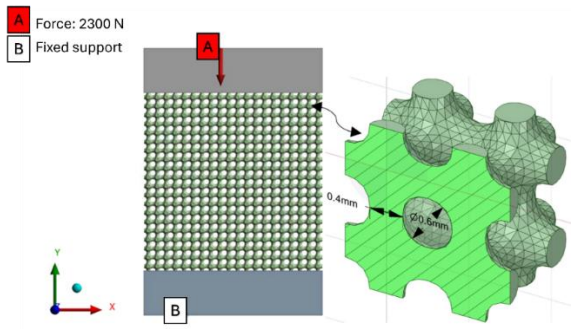

Figure 36. Compression setup for 3D Lattice infill type [177]

Using the stress-strain graph, Figure 37 below shows the resulting value for the Young's modulus of the 3D lattice infill. The graph results in a Young's modulus value of 23022 MPa.

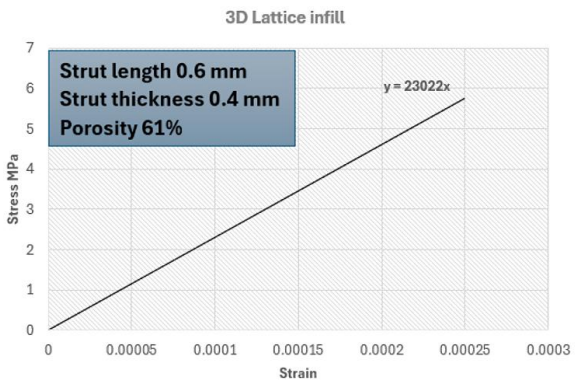

Figure 37. Young's modulus of 3D lattice infill [177]

In Figure 38, the calculations of Poisson's ratio are shown via the numerical compression test of 3D lattice infill unit cell. The same size of cell was used to fill a specimen of 10×6×6 mm.

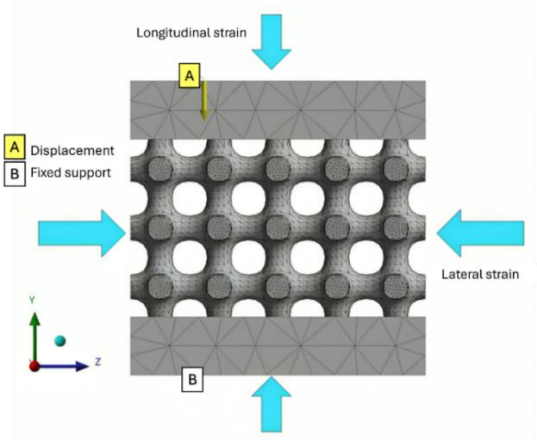

Figure 38. Poisson's ratio compressive test setup [177]

Longitudinal and lateral strain were measured so the Poisson's ration can be calculated using Equation 4.

$$\nu = \left|\frac{\varepsilon_{CS}}{\varepsilon_L}\right| \tag{4}$$

Where $\varepsilon_{cs}$is the cross-sectional normal strain and $\varepsilon_L$is the longitudinal normal strain. Table 8 shows the value of Poisson's ratio.

Table 8. Poisson's ratio result

Lattice	Longitudinal strain	Lateral strain	Poisson's ratio
3D Lattice infill type	0.1001	0.0384	0.384

Ansys SpaceClaim software version 2020 R2 (Ansys, Canonsburg, PA, USA) was used to design the hip implant following the standards of hip implant designing specifications ASTM F2033-12 [178]. Figure 39 shows the parts of the hip implant to be tested numerically. The implant is to be immersed in a resin base, and the middle stem will be filled with lattice structures.

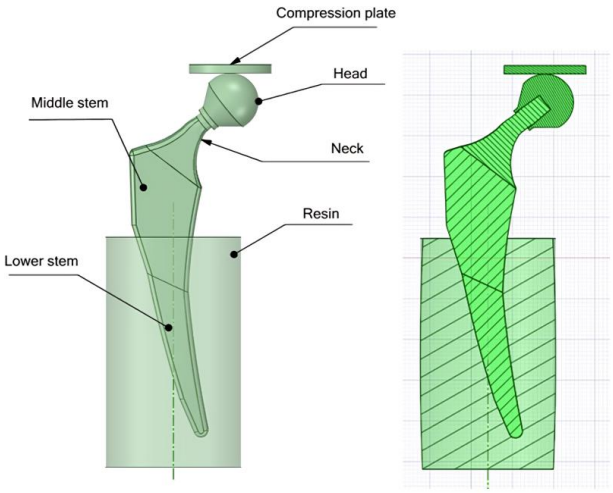

Figure 39. Hip implant [177]

In order to have as close as possible results between the finite element model and the lab compressions to be done, the Young's modulus of the resin to be used in the laboratory test was calculated using a compression test with the Instron 8874 testing machine (Instron, Norwood, MA, USA). Cylindrical specimens were made using the same resin mixture to be used in the test of the implant.

The machine is provided with a built-in computation system that could generate the values of the samples. Figure 40 a and b show the resin specimens and the compression test setup. The test considered the elastic region of the sample and was performed on three different samples, and the average value of Young's modulus was generated.

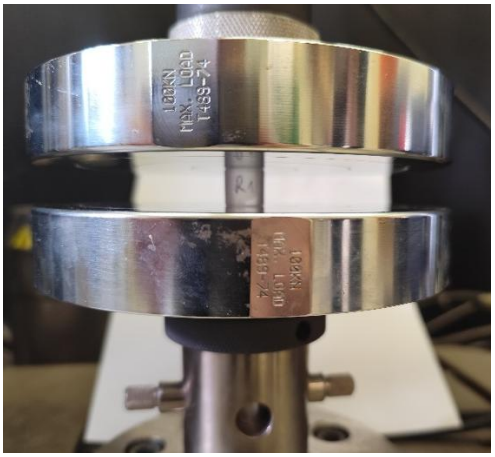

a b

Figure 40. a) Resin samples b) compression test setup

The samples were approximately intended to be 15 mm diameter and 13 mm height, yet the exact measurements are shown in Table 9.

Table 9. Resin samples dimensions and Young's modulus results

Model	Sample 1	Sample 2	Sample 3	Sample 4	Sample 5	Sample 6	Young's modulus (MPa)
	Diameter (mm)			Height (mm)			
1	15.34	15.35	15.38	13.77	13.79	13.71	1104
2	15.35	15.37	15.37	13.78	13.78	13.83	958
3	15.42	15.36	15.42	13.73	13.79	13.73	864
Average	15.37	15.36	15.39	13.76	13.79	13.76	975.33

The average Young's modulus for the resin is 975.33 MPa, this value will be dealt with along the upcoming tests and simulations.

In Table 10, the material properties for each part of the experiment are shown.

Table 10. Material's properties for FEM [179]

Material	Young's modulus MPa	Poisson's ratio	Applied to
Ti6Al4V (Ti64 grade 23)	106247	0.34	Hip implant's parts except for the latticed part
Lattice structure surrogate part (measured)	23022	0.384	Latticed part
CoCrMo	220000	0.35	Femoral head
316Steel	190000	0.26	Pressure plate
Resin	975.33	0.31	Base

3D lattice infill type was applied to the middle stem of the implant design where three different designs were created with 1, 2, and 3 mm shell of thickness. Figure 41 shows the application of lattice structure into the bulk hip implant.

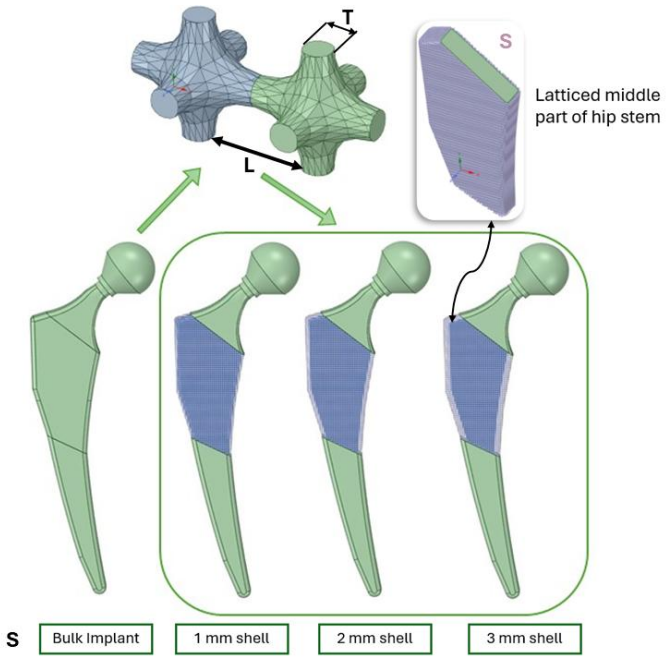

Figure 41. Application of lattice structure to the hip implant [179]

FE analysis was conducted to perform simulation of the latticed hip implant response under in vivo conditions. The compression testing was set up in accordance with ISO 7206-04:2010 [176], regulating the proper force application, the implant angles and the immersion depth into the resin base. The testing conditions are illustrated in Figure 42. As per the standard, a 2300 N force was applied vertically on the compression plate with a frictionless connection between the plate and the implant head, allowing unrestricted sliding along the plate's lower surface. A displacement constraint was imposed on the compression plate limiting its movement to the Y-axis only. The fixed support was set to the resin base, and the vertical deformation was measured as an indicator of the implant's deformation.

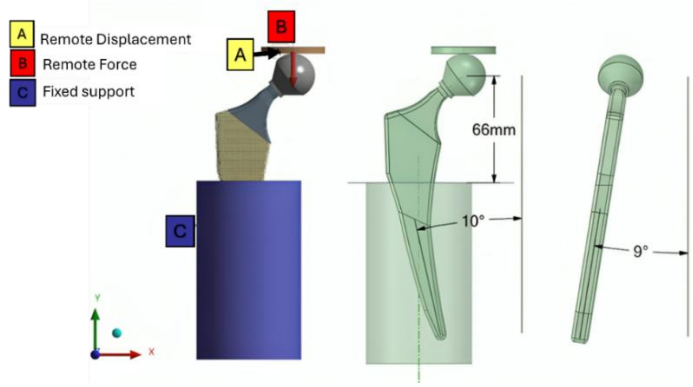

Figure 42. Compression test of hip implant with relation to ISO 7206-4:2010

For the purpose of reducing both time and computation capacity of the simulation, a surrogate model was introduced. In this model, the middle stem part of the implant (the lattice section) was modelled as a bulk geometry while maintaining the mechanical properties of the lattice structure. The two basic properties required for the Ansys Mechanical workbench software are Young's modulus and Poisson's ratio. Figure 43 exhibits a cross-sectional view of the hip designed hip implants, which are considered as surrogate models for the geometrically latticed design.

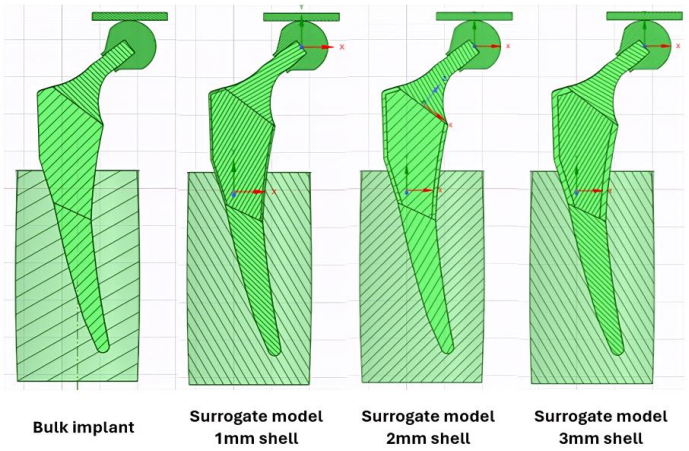

Figure 43. Hip implant's cross-section with surrogate models [179]

The two models, the surrogate model and the geometrically latticed model were compared to show the optimization of the processing time and computation capacity.

FE simulations were conducted to evaluate the hip implant's compressive behavior using ANSYS Mechanical Workbench 2020 R2 (Ansys, Canonsburg, PA, USA). The 3D CAD designs were analyzed with taking the in-vivo conditions into consideration as regulated by the previously mentioned standards. Both models, geometrically latticed and the surrogate models, were examined during the analysis.

6.3 Laboratory compression test

For validation purposes, the designed implants were 3D-printed, the 1 mm shell latticed design was 3D printed to be tested on compression in the laboratory. The 3D-printing was executed using EOS M290 (Electro Optical Systems, Munich, Germany) 3D printer. Figure 44 shows an example of the 3D printed implants. 3 samples were printed to have the average result.

Figure 44. 1 mm shell 3D printed implant

Hip implant's compression test standard ISO 7206-4:2010 [176] was followed within the procedure. Instron 8874 servo-hydraulic fatigue testing machine (Instron, Norwood, MA, USA) was used during the test. As per the standard, a 2300 N force was applied with a loading speed of 2mm/min and the implant was held into the resin base with the required angles, where a vice was used to keep the implant in the right position until the resin has solidified. Figure 45 shows how the implant is held in place using a moving vice.

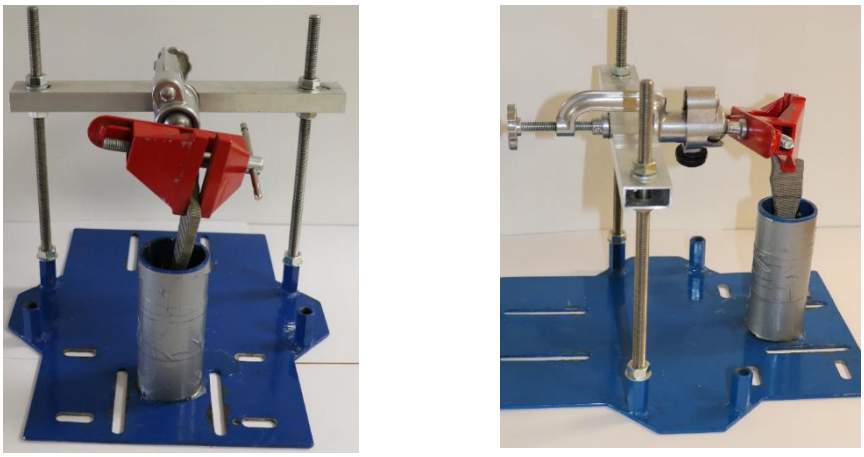

Figure 45. Positioning implant into the Resin

Figure 46 shows the implant under the horizontal compression plate with the numbering system for each implant.

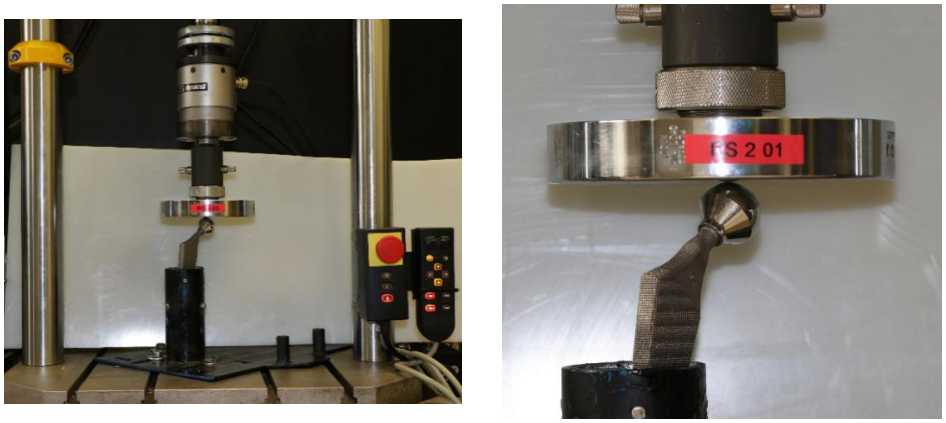

Figure 46. Hip implant compression setup

6.4 FEM results

Since the compression machine usually records the compression plate vertical deformation, Figure 47 compares the vertical deformation of the plates of the two models. The legends colored with black represent the absolute vertical deformation values, while the colorful legends provide insight into the implant's overall deformation behavior.

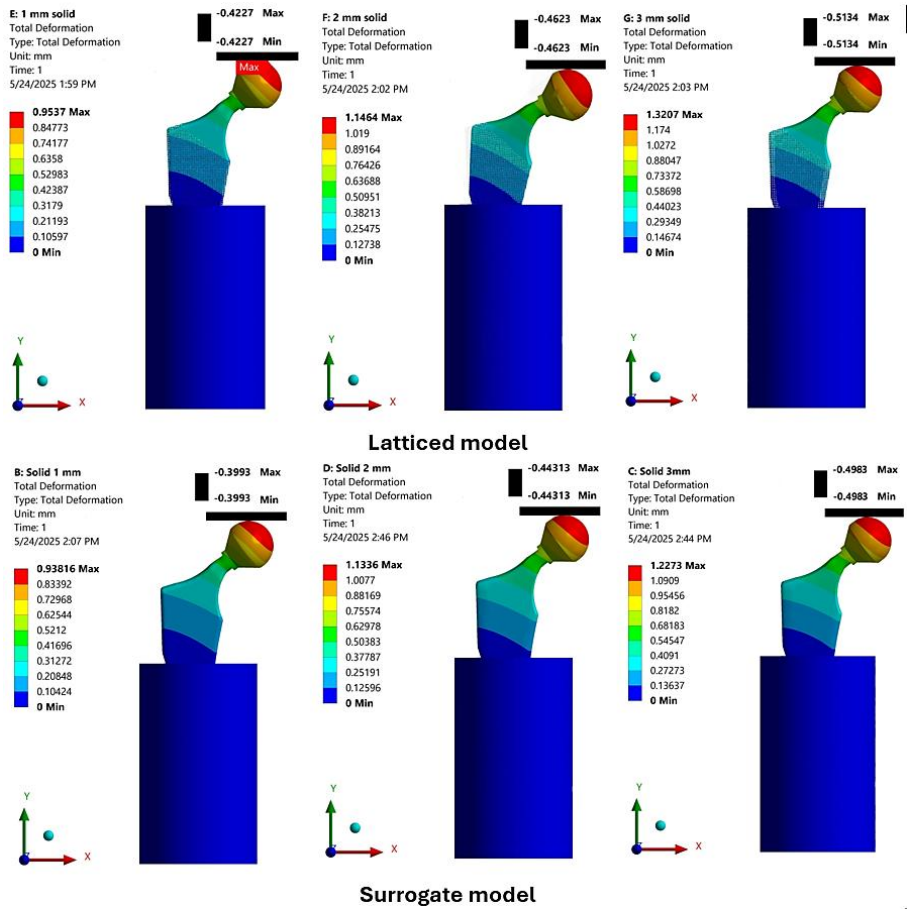

Figure 47. Compression plates' vertical deformation, latticed vs surrogate models

Table 11 shows a comparison, in values, between geometrically latticed model and surrogate model. The deviation range among the results varies between 2-5% which is an acceptable range.

Table 11. Vertical deformation results deviation between latticed and surrogate models FEM

Model	1 mm lattice	2 mm lattice	3 mm lattice
	Vertical deformation mm		
Geometrically latticed model	0.422	0.462	0.513
Surrogate model	0.399	0.443	0.498
Deviation %	5	4	2

The results were assessed through conducting a mesh convergence analysis of the vertical deformation in relation to the mesh size that is shown in Figure 48. The final mesh size of 0.5 mm was selected, and a tetrahedral mesh type with patch-independent method were applied to the model. A convergence of 5% was achieved.

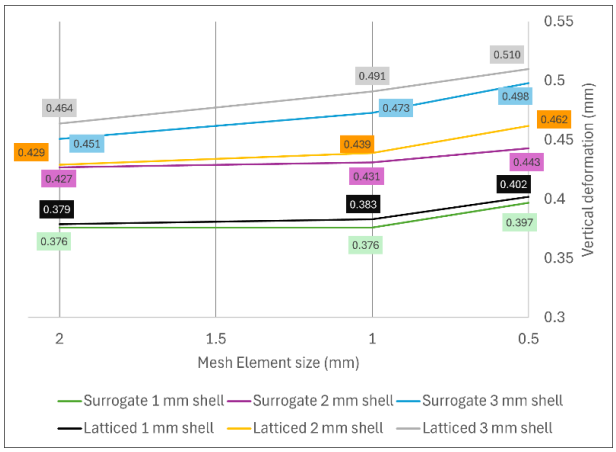

Figure 48. Mesh convergence

Therefore, the surrogate model can be a good replacement of the geometrically latticed model while still providing accurate results in numerical simulations. Table 12 exhibits a comparison of the two models with relation to the computation time and the RAM consumption in the operating system. The simulations were performed on a computer with four logical processors, four Intel® cores, and 16 GB installed physical memory (RAM).

Table 12. Deviations in computation results for latticed model vs surrogate model

	1 mm lattice		2 mm lattice		3 mm lattice	
Model	Normal model	Surrogate model	Normal model	Surrogate model	Normal model	Surrogate model
Time (s)	1580	17	7363	20	9683	24
Maximum Memory used (MB)	1878	116	1924	124	2293	140

Using the surrogate model significantly reduces both computation time and RAM usage, leading to substantial time and cost savings in the simulation process. The computation time decreased from several thousand seconds to just a few seconds, while RAM usage was reduced from thousands to only a few hundred seconds. The surrogate model can help facilitate the simulations performed on lattice structures where it can generate the resulting mechanical behavior almost with the same accuracy done on the normal model. Its ability to reduce computation time and capacity can greatly reduce the cost of the simulation process.

6.5 Laboratory compression test results

Table 13 compares the vertical deformation values of the latticed model calculated via FE analysis, with the values obtained from laboratory experiments for the 1 mm shell latticed implant. The comparison helps evaluate the accuracy and reliability of the FEM model by monitoring the match between the two results. The vertical deformation values for all three samples of the 1 mm implant are averaged and then compared with the value from the finite element analysis. A deviation of 5% is noticed.

Table 13. Vertical deformation Latticed model FE results vs Lab results

Implant 1	Implant 2	Implant 3	Average	Geometrically latticed model (FEM)	Deviation %
	Lab results				
			Vertical Deformation (mm)		
0.452	0.424	0.450	0.442	0.422	5

The deviation in results between the lab values and the FE values can be attributed to the following reasons: the inaccuracy of the exact positioning of the implant in the resin base, the machine error, the complex measurement setup due to many components participating in the process, and the 3D printing error.

Chapter 7: Porosity prediction via machine learning

A hip implant model was developed with the help of SpaceClaim software within the Ansys software 2021 R2 version (Ansys, Canonsburg, PA, USA). The purpose of the study is to improve osseointegration, enhance durability, and increase the total strength of the implant. Figure 49, a) a wall of 2 mm thickness all over the transparent part of the implant has been latticed with three kinds of unit cells b) 3D-lattice infill, c) double pyramid lattice and face diagonals, and d) octahedral lattice 2.

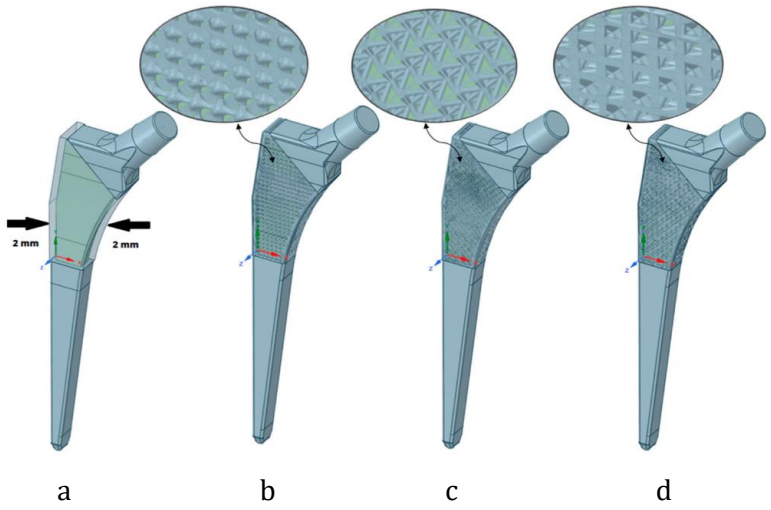

Figure 49. (a) Bulk Hip implant , (b) 3D-lattice infill, (c) double-pyramid lattice and face diagonals, (d) octahedral lattice 2

The porosity of the unit cells in the latticed parts of the implants was calculated for each type using equation 3. The results of the porosity can serve as a measure to provide an initial evaluation into the implant's composition and its biomechanical properties. Porosity range plays a significant role in determining the optimization process in the hip implant's design.

Many scenarios of length and thickness for the lattice structures strut were applied, and the porosity values were calculated as a result for these scenarios. They were chosen based on the manufacturing limits and the osseointegration suitability ranges as stated in our previous work [126]. Table 14 presents the porosity's values for each type of unit cell. In order to reach a required value of the porosity of a certain design of the hip implant, the values of the length and thickness were manipulated within the effective ranges that can present an implant with good osseointegration results and, at the same time, considers the manufacturing limits. All the results were then reorganized and shown as ranges.

Table 14. Range of porosity's values and their corresponding values of length and thickness

Unit cell type	Length (mm)	Thickness (mm)	Porosity (%)
3D lattice infill	1-1.6	0.2-1.5	50-83
Double pyramid lattice and face diagonals	1.8-2.5	0.2-0.6	51-86
Octahedral lattice 2	2-2.7	0.2-0.65	51-87

To help show the arranged input data as a range of strut's length and thickness's values, the visualizing Figure 50 was created.

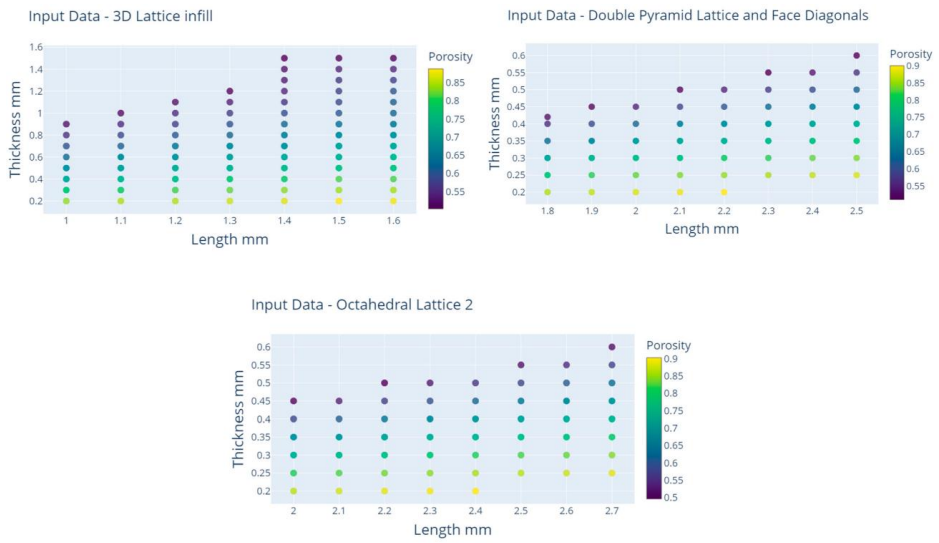

Figure 50. Unit cells' input data

Figure 51 also clarifies the ranges of data in a histogram plot for data.

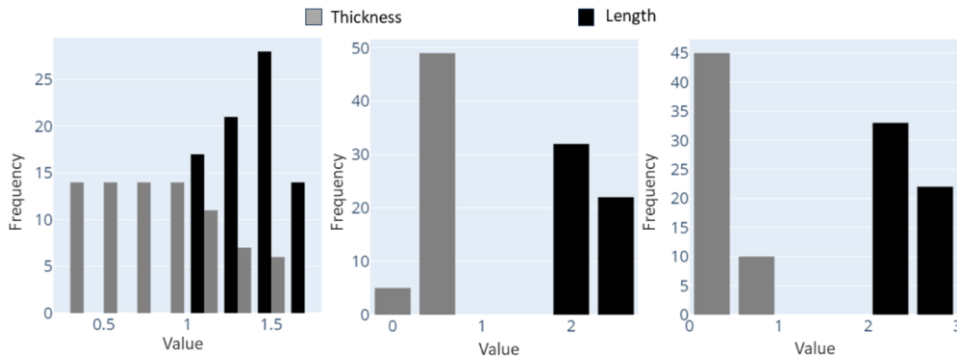

a b c

Figure 51. Input data histogram: (a) 3D-lattice infill, (b) double-pyramid lattice and face diagonals, (c) octahedral lattice 2.

For each type under investigation, the data were collected as pairs of length and thickness of the strut and their corresponding resulting porosity. Necessary libraries were used in the model, NumPy for numerical operations, Pandas for data manipulation, Linear Regression from scikit-learn [179] for linear regression. For calculation of R-square score, r1_score from scikit learn was imported. To create a 3D plot, Plotly.Graph-obj was also used.

Data were imported to Pandas in Jupyter Notebook 6.4.5 from a CSV file. Two features were recognized by the model as “Length” and “Thickness”, whereas the variable “Porosity” was considered a target variable, and they were stored in arrays ‘X’ and ‘y’, respectively. A linear regression model was formed and trained using feature array ‘X’ and target variable array ‘y’.

The model was utilized to anticipate the porosity values of the feature space, which was formed by generating a range of values for Length and Thickness through NumPy’s linspace function. The process resulted in the creation of ‘length-mesh’ and ‘thickness-mesh’, representing all possible combinations of Length and Thickness values. Using np.column-stack, the feature space was created by combining these two meshgrids. Subsequently, the model predicted porosity values for the feature space, which were then reshaped to match the shape of meshgrid in ‘porosity-pred’.

The model’s accuracy was assessed with the help of R-squared score by comparing predicted porosity values for the original ‘X’ against the actual porosity values ‘y’ and accordingly computing the R-squared score. Results were presented using 3D plot with Plotly, a Python library used for data visualization. The model was run for three cases for three sets of learning points with each set having a different number of learning points. The aim was to approximately find how many learning points are needed to build an accurate machine-learning model that can predict reasonable and effective porosity values.

In each case, a separate machine learning model was created for a third of the data, then two-thirds, then all learning points. The numbers for each set of learning points can be seen in Table 15.

Table 15. Numbers of learning points

Unit cell type	Case 1	Case 2	Case 3

3D lattice infill	27	54	81
Double pyramid lattice and face diagonals	18	35	54
Octahedral lattice 2	18	35	54

The machine learning models were done with good accuracy for all types of lattice structures. Table 16 exhibits the accuracy values for all types. When checking the accuracy levels in each case, it is clear that a good accuracy level can be reached out of 81, 54, 54, learning points for 3D lattice infill, Double pyramid lattice and face diagonals and Octahedral lattice 2 respectively.

Table 16. Accuracy values for lattice types

Unit cell type	Case 1 Accuracy (%)	Case 2 Accuracy (%)	Case 3 Accuracy (%)
3D lattice infill	98	96	96
Double pyramid lattice and face diagonals	98	98	99
Octahedral lattice 2	98	99	99

Figure 52 shows the model results where actual porosity values are shown as scattered blue points, and the predicted porosity values for the feature space are shown as color-graded surface plots.

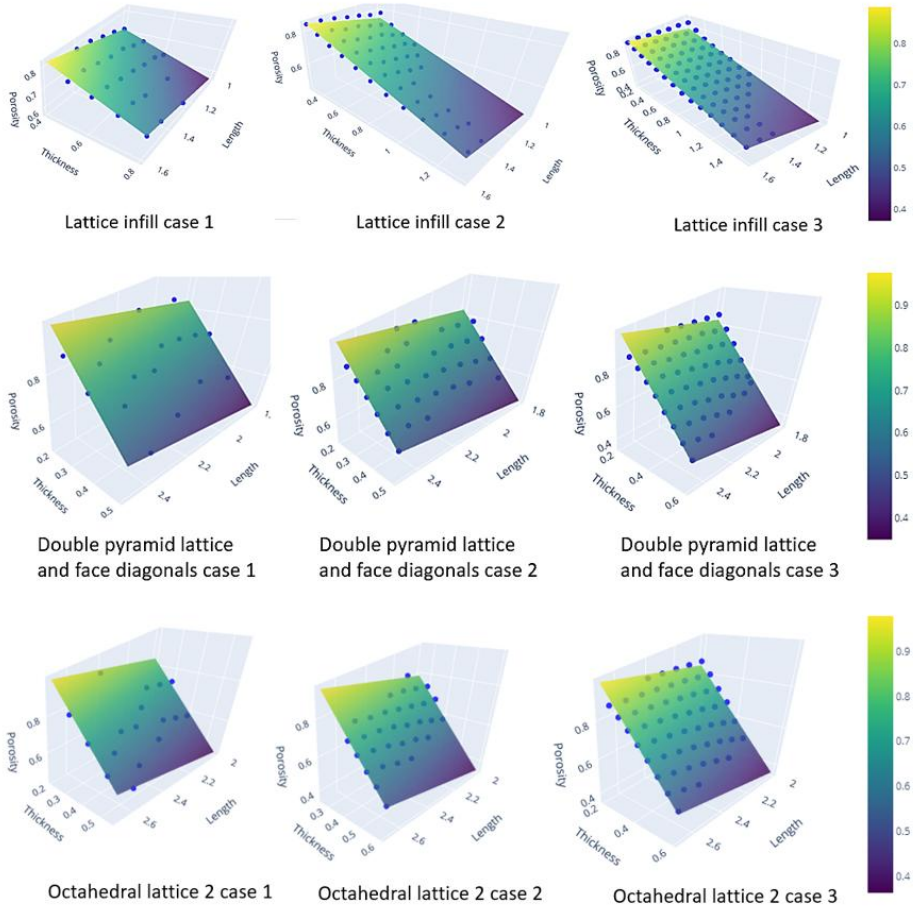

Figure 52. ML models

The models' accuracy for all models was also shown in Figure 53 using regression lines to visualize how accurate the models were.

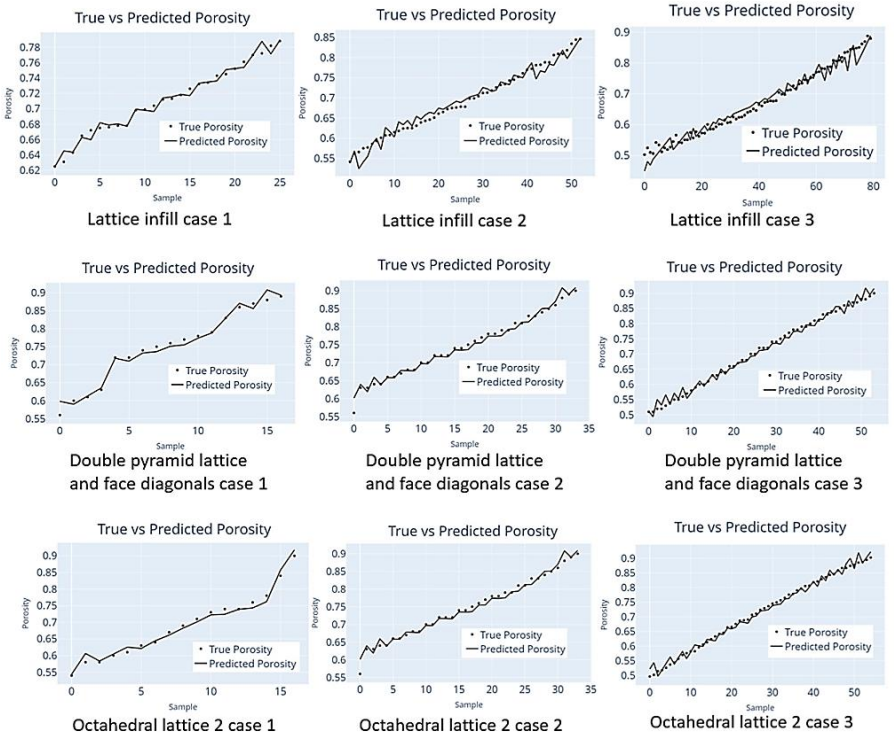

Figure 53. Prediction True vs Predicted

The higher accuracy the model shows, the more efficient and productive the process will be for predicting porosity and saving time and effort by avoiding trial-and-error process to reach the desired optimum porosity for a specific hip implant design. Double pyramid lattice type and octahedral lattice type presented more accurate results, and that is due to their inner structure being easier to predict and more mathematically conforming than the 3D lattice infill type. However, the accuracy level was over 96% for all three types, which is considered acceptable.

Chapter 8: Hip implant stem database

8.1 Introduction

The MATLAB regression learner app is an interactive tool provided by MATLAB to enable users to train, validate and compare the regression models without the need to write the actual code themselves. It is classified as part of the Statistics and Machine learning toolbox in the MATLAB application. Data can be imported into the app, and then the feature selection can be performed, multiple regression models can then be trained. The performance evaluation can be executed with metrics like RMSE, R-squared, and MSE. Subsequently, predictive models can be developed quickly and visually.

Several regression algorithms are used in the Regression learner app where a comparison in results can be shown quickly after calculation. The algorithms can be categorized into: Linear models such as Linear Regression Interactions Linear and Robust Linear, SVMs like Linear SVM Quadratic SVM and Cubic SVM, Decision trees like Fine tree Medium Tree and Coarse Tree, Ensemble models like Boosted Trees and bagged Trees, Gaussian Process Regression (GPR) like exponential GPR Squared Exponential GPR and Rational Quadratic GPR, Neural Networks like Narrow NN Medium NN and Wide NN [180].

The Regression learner app is, therefore, an ideal tool for our research in order to easily prototype and evaluate a wide range of regression models and make a comparison to choose the best machine learning method for accurate prediction results.

Since the main goal was to develop a predicting model that could give the outputs that defined the mechanical behavior of the latticed hip implants, only one size of hip implant was used, where in the future studies, the model could be generalized to include more than one size of latticed implant.

8.2 Hip Implants data preparation from FEM

Following our work described in Chapter 6, after designing the latticed hip implants with three variations: 1,2 and 3 mm of latticed structures as shown in Figure 41, the implants were tested numerically using the ANSYS software R2 version 2020 (Ansys, Canonsburg, PA, USA). In order to simulate the exact loads exerted *in vivo* on the hip implant, Bergmann [181] loading instructions were followed throughout the simulation.

In our case, the stumbling case was taken into consideration where the highest loads take place on the hip implant. In Figure 54, the hip implant accommodation inside the femur is shown.

Figure 54. Hip implant accommodation in the femur

The hip implant's loading condition based on Bergmann's standard are shown in Figure 55.

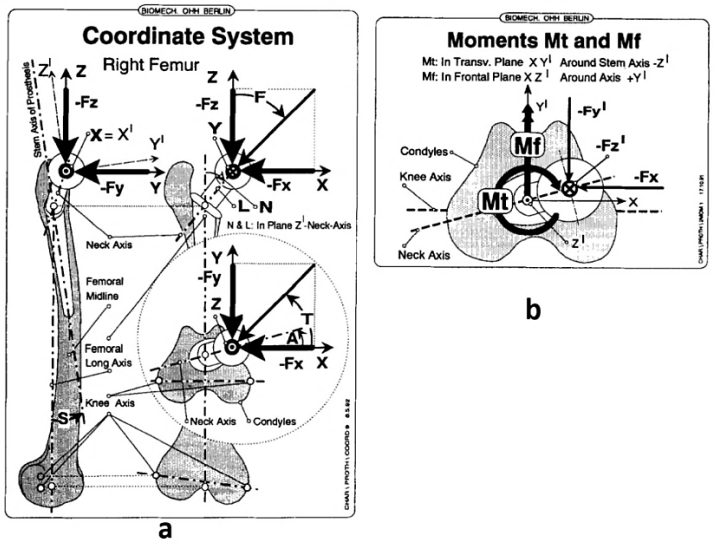

Figure 55. a) Forces and b) resulting moments, acting on the hip implant [182]

Force values were also calculated based on the same standard where Bergmann stated the values as a graph relative to the person's weight. Table 17 shows the calculated forces acting on the hip implant.

Table 17. Force values

Weight (kg)	F X-axis (N)	F Y-axis (N)	F Z-axis (N)	F Total (N)
60	1764	588	4704	5058.5
90	2646	882	7056	7589.3
120	3528	1176	9408	10104.3

These values of forces were applied for each variation of the hip implant with the three shell volumes. Figure 56 shows the simulative compression test conditions and the application of the 60 kg case of forces in the numerical study with reference to Bergmann's loading instructions. Since the femur is the fixed support as a constraint in the simulation, it was replaced with a cylinder to make the selection and calculation process easier.

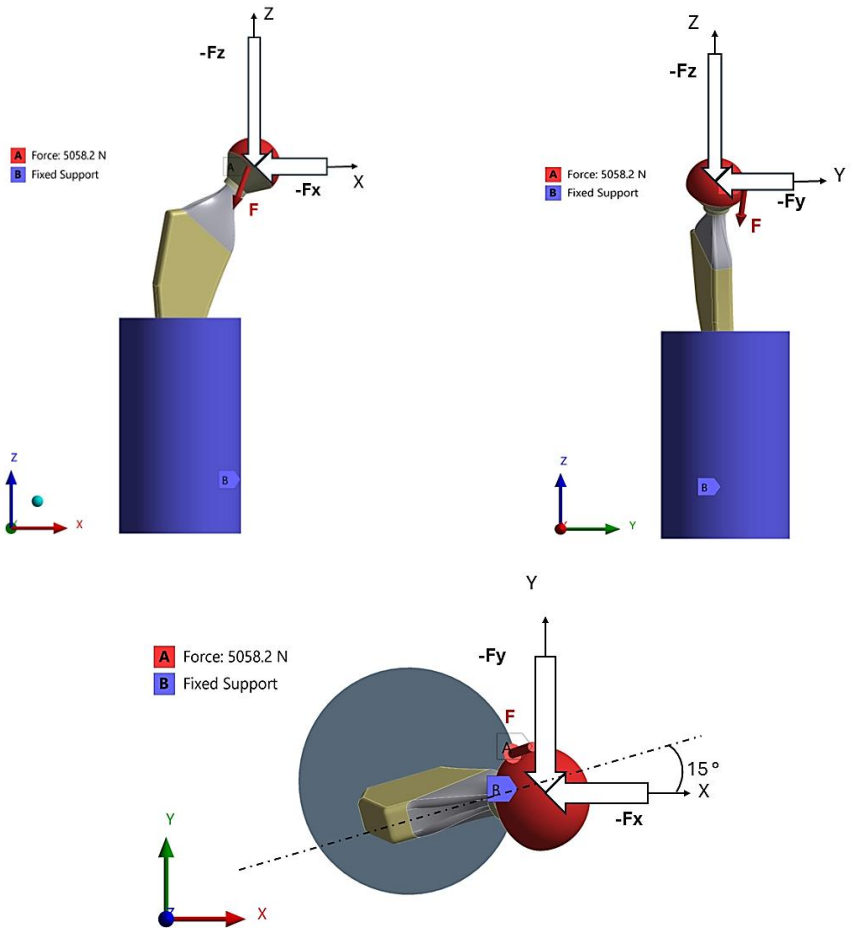

Figure 56. Forces acting on hip implant in stumbling case

Young's modulus values were calculated for 6 cases of Lengths and thicknesses, and then these values were applied to the 1- and 3-mm shelled thickness variations of hip implants for three weight cases of 60, 90 and 120 kg. The design parameters for the input data are taken according to the following ranges:

$$L(mm) \in (0.4, 0.6, 0.8), T(mm) \in (0.2, 0.4, 0.6),$$
$$S\ (mm) \in (1,2,3), W(kg) \in (60,90,120),$$

where L is the unit cell length, T is the unit cell thickness, S is the latticed shell thickness and W is the weight of the patient. L and T diemnsions were chosen based on medical guidelines so that the cell size helps osseointegration. The choice of shell thickness is based on the dimensions of the implant stem.
Once gathered, a total of 81 cases, the data were organized in a table and then imported into MATLAB version R2024b (MathWorks, Massachusetts, USA) and the Regression learner application analysis was applied on the data considering the L, T, S and W as inputs and the u_{max}, $\sigma_{max}$and U as outputs.

A separate regression learner model was developed for each resulting output due to the complexity of developing a single model to generate all the results. 80% of the data was used as a training set and 20% was used as a testing set. Cross validation scheme of 10 folds was applied to the data to avoid overfitting. In order to evaluate the accuracy of the prediction models, RMSE and R-squared values were checked for each model. Table 18 shows the FE calculated outputs for the mentioned ranges of lengths and thicknesses and according to the weights.

Table 18. FE calculated outputs values of the learning and testing points

Input				**output**	**output**	**output**
L (mm)	**T (mm)**	**S (mm)**	**W (kg)**	**umax (mm)**	**σmax (MPa)**	**U (Nmm)**
0.4	0.2	1	60	1.067	418.488	7.269
0.6	0.2	1	60	1.151	418.490	7.269
0.8	0.2	1	60	1.245	418.492	7.269
0.4	0.4	1	60	0.936	418.484	7.269
0.6	0.4	1	60	1.000	418.486	7.269
0.8	0.4	1	60	1.116	418.489	7.269
0.4	0.6	1	60	0.891	418.483	7.269
0.6	0.6	1	60	0.979	418.485	7.269

0.8	0.6	1	60	1.017	418.486	7.269
0.4	0.2	1	90	2.835	753.338	24.388
0.6	0.2	1	90	3.086	753.335	24.390
0.8	0.2	1	90	3.364	753.333	24.392
0.4	0.4	1	90	2.445	753.343	24.384
0.6	0.4	1	90	2.637	753.340	24.386
0.8	0.4	1	90	2.981	753.336	24.389
0.4	0.6	1	90	2.309	753.345	24.382
0.6	0.6	1	90	2.573	753.341	24.385
0.8	0.6	1	90	2.686	753.340	24.386
0.4	0.2	1	120	2.134	836.975	29.077
0.6	0.2	1	120	2.302	836.980	29.078
0.8	0.2	1	120	2.490	836.984	29.078
0.4	0.4	1	120	1.872	836.968	29.075
0.6	0.4	1	120	2.001	836.971	29.076
0.8	0.4	1	120	2.232	836.978	29.077
0.4	0.6	1	120	1.781	836.965	29.074
0.6	0.6	1	120	1.958	836.970	29.076
0.8	0.6	1	120	2.034	836.972	29.076
0.4	0.2	3	60	2.554	418.500	7.273
0.6	0.2	3	60	3.396	418.504	7.274
0.8	0.2	3	60	4.712	529.230	11.209
0.4	0.4	3	60	1.663	418.494	7.271
0.6	0.4	3	60	2.049	418.497	7.272
0.8	0.4	3	60	3.011	418.503	7.274
0.4	0.6	3	60	1.439	418.493	7.270
0.6	0.6	3	60	1.911	418.496	7.272
0.8	0.6	3	60	2.162	418.498	7.273
0.4	0.2	3	90	3.831	627.751	16.365
0.6	0.2	3	90	5.095	627.756	16.367
0.8	0.2	3	90	7.068	793.845	25.220
0.4	0.4	3	90	2.494	627.742	16.360
0.6	0.4	3	90	3.073	627.746	16.363
0.8	0.4	3	90	4.517	627.754	16.366
0.4	0.6	3	90	2.158	627.739	16.358
0.6	0.6	3	90	2.866	627.744	16.362
0.8	0.6	3	90	3.243	627.747	16.363
0.4	0.2	3	120	4.736	856.799	34.638

0.6	0.2	3	120	6.328	856.811	34.640
0.8	0.2	3	120	8.881	972.743	41.797
0.4	0.4	3	120	3.091	856.785	34.633
0.6	0.4	3	120	3.799	856.792	34.636
0.8	0.4	3	120	5.595	856.806	34.639
0.4	0.6	3	120	2.683	856.782	34.630
0.6	0.6	3	120	3.546	856.790	34.635
0.8	0.6	3	120	4.008	856.794	34.636
0.4	0.2	2	60	1.949	418.506	7.274
0.6	0.2	2	60	2.328	418.510	7.275
0.8	0.2	2	60	2.791	418.514	9.222
0.4	0.4	2	60	1.440	418.498	7.273
0.6	0.4	2	60	1.677	418.502	7.274
0.8	0.4	2	60	2.164	418.508	7.275
0.4	0.6	2	60	1.290	418.496	7.272
0.6	0.6	2	60	1.596	418.501	7.273
0.8	0.6	2	60	1.742	418.503	7.274
0.4	0.2	2	90	3.215	721.024	13.546
0.6	0.2	2	90	3.949	721.057	17.106
0.8	0.2	2	90	5.021	829.867	23.008
0.4	0.4	2	90	2.363	720.993	13.543
0.6	0.4	2	90	2.745	721.005	13.544
0.8	0.4	2	90	3.620	721.042	14.943
0.4	0.6	2	90	2.131	720.988	13.541
0.6	0.6	2	90	2.611	721.000	13.544
0.8	0.6	2	90	2.853	721.009	13.545
0.4	0.2	2	120	3.685	856.822	34.639
0.6	0.2	2	120	4.417	856.834	34.641
0.8	0.2	2	120	5.330	856.846	34.954
0.4	0.4	2	120	2.725	856.802	34.634
0.6	0.4	2	120	3.169	856.812	34.637
0.8	0.4	2	120	4.099	856.829	34.640
0.4	0.6	2	120	2.444	856.795	34.632
0.6	0.6	2	120	3.016	856.809	34.636
0.8	0.6	2	120	3.291	856.814	34.637

8.3 Regression learner results

The regression learner application trained all kinds of models and showed the RMSE and MSE results for the validation and test set results. The four best results in terms of RMSE and R-squared value for total displacement Umax is shown in Table 19. Wide neural network performed the best in both training and testing based on the RMSE value, which proves good generalization. The model also scored high R-squared value which explains the variance in the data.

Table 19. Evaluation of the Total displacement prediction model

Model	RMSE		R-squared	
	Training	Test	Training	Test
Neural Network (Wide NN)	0.26	0.31	0.96	0.96
Neural Network (Medium NN)	0.30	0.34	0.95	0.93
Neural Network (Bilayered NN)	0.40	0.42	0.91	0.90
Gaussian Process Regression (Matern 5/2 GPR)	0.51	0.62	0.85	0.76

While in Table 20 the best models for stress von Mises prediction are shown. Gaussian process regression with squared exponential type showed the lowest error values, and a good R-squared value, proving the best reliability.

Table 20. Evaluation of the Stress von Mises prediction model

Model	RMSE		R-squared	
	Training	Test	Training	Test
Gaussian Process Regression (Squared exponential GPR)	14.55	15.36	0.99	0.98
Gaussian Process Regression (Rational quadratic GPR)	14.64	15.95	0.99	0.96
Neural Network (Trilayered NN)	18.35	34.07	0.99	0.95

Tree (Fine tree)	20.69	47.77	0.99	0.90

Table 21 shows the best four models for total strain energy, where trilayered neural networks yielded a low RMSE value and a high R-squared value in both models, training and testing, which outperformed the rest of the models.

Table 21. Evaluation of the Total strain energy prediction model

Model	RMSE		R-squared	
	Training	Test	Training	Test
Neural Network (Trilayered NN)	0.34	1.06	0.99	0.97
Tree (Fine tree)	0.42	0.88	0.96	0.98
Neural Network (Wide NN)	0.42	0.99	0.95	0.94
Neural Network (Bilayered NN)	0.71	0.74	0.93	0.95

As can be seen from the above tables, various models of neural networks performed well for each set of data. Figure 57 shows the True vs Predicted response of the training and testing models for all three outputs.

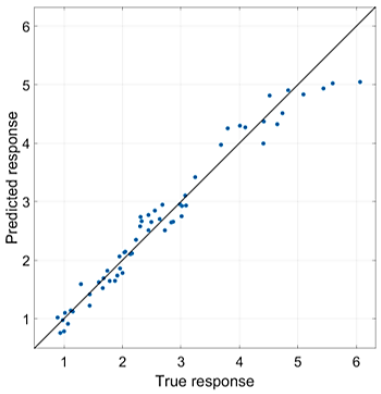

a

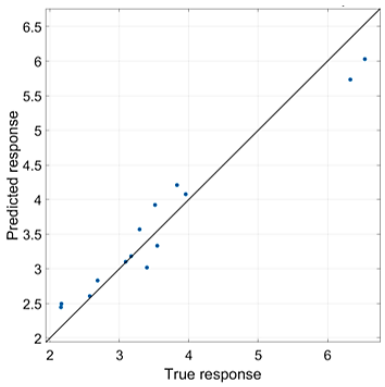

b

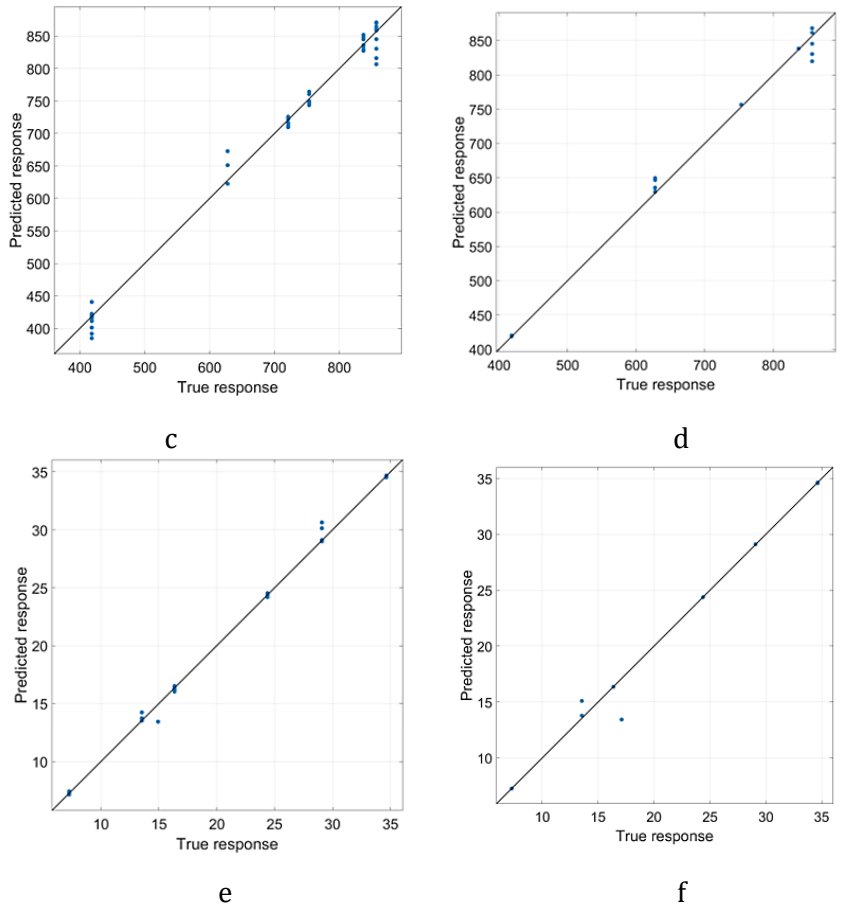

Figure 57. True vs Predicted response graph a) Maximum displacement training, b) Maximum displacement testing , c) von Mises stress training d) von Mises stress testing e) Total strain energy training f) Total strain energy testing

The models are performing fairly well, however, there is noticeable deviation for higher true values, especially in stress and total energy cases, which suggests that models struggle a bit with the extreme cases. Overall, the models have decent predictive accuracy with moderate variance and a slight bias for larger values.

For verification purposes, finite element analysis was performed for a patient weighing 80 kg where the forces and moments were calculated accordingly. The shell thickness was chosen to be 2 mm, length was 0.4 mm, and thickness

was 0.2 mm All three output values, deformation, stress and total energy were calculated via FE. Figure 58 shows the FE calculated results.

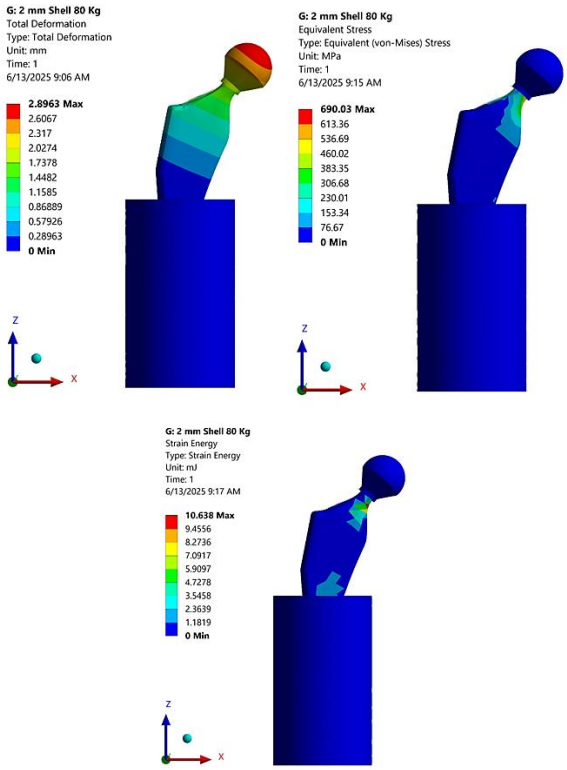

Figure 58. FE calculated values case 2mm shell, 80-kg patient Length 0.4, Thickness 0.2

The results were compared with the values calculated via the trained models. Table 22 shows the deviation between the two results. The model generalized well with accuracy over 90% where it generated results deviating up to 9% from the FEM analyzed ones.

Table 22. FEM calculated cases vs Trained model calculated case

				Regression model	FEM	
L (mm)	T (mm)	S (mm)	W (kg)	u_{max} (mm)	u_{max} (mm)	Deviation %
0.4	0.2	2	80	3.094	2.896	6

L (mm)	T (mm)	S (mm)	W (kg)	σ_{max} (MPa)	σ_{max} (MPa)	Deviation %
0.4	0.2	2	80	633.270	690.030	9
L (mm)	T (mm)	S (mm)	W (kg)	U (Nmm)	U (Nmm)	Deviation %
0.4	0.2	2	80	11.651	10.638	9

The generated models were then exported into MATLAB and used to create a database for almost all possible cases of latticed implants variables. The calculations took the following ranges into consideration:

$L(mm) \in (0.4,0.45,0.5,\dots,0.8)$, $T\ (mm)\ \in\ (0.2,0.25,0.3,\dots.,0.6)$,

$S\ (mm)\ \in\ (1,1.5,2,2.5,3), W\ (kg)\ \in\ (60,70,80,\dots,120)$,

This database can be a reference for the surgeon to choose the suitable case for each specific patient. Models can now predict the behavior of the latticed implant against real life conditions without having to go through the simulation or the lab testing. Table 23 shows the first and last fourteen values of the database for reference. The database is composed of 2835 cases of latticed hip implants.

Table 23. Hip implant stem database

L (mm) 0.4-0.8	*T (mm) 0.2-0.6*	*S (mm) 1-3*	*W (kg) 60-120*	u_{max} *(mm)*	σ_{max} *(MPa)*	*U (N.mm)*
0.4	0.2	1	60	1.067	418.828	7.269
0.4	0.2	1	70	1.919	549.275	10.951
0.4	0.2	1	80	2.576	663.058	18.215
0.4	0.2	1	90	2.836	752.574	24.388
0.4	0.2	1	100	2.775	812.570	25.862
0.4	0.2	1	110	2.482	840.652	27.090
0.4	0.2	1	120	2.134	837.419	29.113
0.4	0.2	1.5	60	1.505	418.465	7.250
0.4	0.2	1.5	70	2.878	542.881	9.014
0.4	0.2	1.5	80	3.945	653.648	15.591

0.4	0.25	1	60	2.383	418.311	7.482
0.4	0.25	1	70	3.635	512.266	8.282
0.4	0.25	1	80	4.519	604.180	10.658
0.4	0.25	1	90	4.914	688.855	11.898
.	.	.	.	.	.	.
.	.	.	.	.	.	.
.	.	.	.	.	.	.
.	.	.	.	.	.	.
.	.	.	.	.	.	.
0.8	0.55	3	90	628.111	16.366	3.511
0.8	0.55	3	100	699.915	22.400	3.774
0.8	0.55	3	110	766.507	28.480	4.143
0.8	0.55	3	120	824.528	34.617	4.344
0.8	0.6	2.5	100	749.252	17.827	4.457
0.8	0.6	2.5	110	803.909	26.825	4.460
0.8	0.6	2.5	120	841.521	35.755	4.054
0.8	0.6	3	60	418.594	7.272	2.160
0.8	0.6	3	70	484.190	7.646	2.777
0.8	0.6	3	80	555.031	10.614	3.008
0.8	0.6	3	90	627.665	16.363	3.243
0.8	0.6	3	100	698.392	22.396	3.553
0.8	0.6	3	110	763.578	28.476	3.930
0.8	0.6	3	120	819.963	34.636	4.008

Chapter 9: Conclusion and Future Work

Over the last decades, hip implant designers have always sought the optimization of the hip implant design by applying many techniques. The main aim has always been the quality improvement of the hip implant replacement process. This dissertation has built a designing chart flow, where the final result can be a well suitable patient-specific hip implant designed with the exact needs of the patient and optimized in way that increases the osseointegration of the hip with the adjacent bone, optimizes the weight and volume of the implant, and, at the same time, keeps the limits of manufacturability in consideration.

The main theme of this research has benefited from the lattice structure properties in order to generate a lattice-optimized hip implant that has the biomedical properties required by patients, and with the help of machine learning modules, the properties of the lattice structures can be manipulated, and the target design's properties can be anticipated and hence adjusted in the patient's favor.

One of the obstacles that face biomedical designers when using lattice structures to optimize a structure, like the hip implant, is the complexity of the inner structure of these lattices. This creates the problem of having to wait for long hours of analysis time even with the use of heavy-duty computers. Consequently, building a machine learning model that can predict the resulting properties of lattice-optimized implants can save both the time and cost of such an optimization. In this research, a machine learning model was developed to expect the porosity of the resulting design based on the length and thickness of the lattice structures. This can help a lot yet building a complete model that can take many input properties and anticipate all the biomedical properties that can help designers judge the quality of the resulting implant.

Another breakthrough was the building a regression model to help generate the indicators that define the mechanical behavior of the latticed implant which makes the selection process of the latticed hip implant an easier process for the surgeons based on the patient's needs.

Another aim in the near future is to try to build an immediate connection between designing variables and the ANSYS software, where the APDL Ansys Parametric Design Language can be connected with the design's variables and can be changed in real-time to show and preview the resulting design.

Theses:

This section shows the dissertation's relevant contributions, and the publications associated with the work done during the PhD stages.

Thesis 1:

Development of lattice structures to support bone ingrowth and reduce stress shielding for hip implant stem design

Test specimens with the same porosity, designed using four different lattice structures (3D lattice infill, Double pyramid lattice with cross, Double pyramid lattice and face diagonals, Octahedral lattice) and developed for hip implant placement were printed using additive technology and Ti6Al4V raw material according to ISO 13314 standard. The cell sizes of the specimens were chosen to promote bone ingrowth for better fixation. Compression tests showed that the stiffness of the bulk material can be reduced by 90% using the investigated lattice structures. With this method, I developed lattice structures whose stiffness closely approximates the stiffness of the femur, thereby reducing the occurrence of stress shielding.

This thesis is based on the following publications: (P1), (P5), (P7)

Thesis 2:

Development of a surrogate finite element model for lattice-structured hip implant stem

Due to the complex geometry, finite element analysis of a hip implant stem designed with a lattice structure is extremely time-consuming. A surrogate finite element model has been developed for the hip implant stem to replace the lattice structures. This shortens the finite element pre-processing and reduces the computational cost by several orders of magnitude while

maintaining the calculation accuracy in accordance with engineering practice. The developed surrogate model enables serial calculations for optimization tasks to be performed in a manageable amount of time, thus accelerating the hip implant design process.

This thesis is based on the following publication: (P4)

Thesis 3:

Porosity prediction of lattice structures using linear regression algorithm

Due to the complex design, geometric modeling of lattice structures is extremely time-consuming. The porosity of structures made of lattices depends primarily on the choice of the dimensions of the lattice length and lattice thickness. A linear regression algorithm was used to estimate the porosity of 3 different lattice structures (3D lattice infill, Double pyramid lattice and face diagonals, Octahedral lattice) as a function of lattice length and lattice thickness. The applied machine learning model is able to estimate the porosity of the lattice structure with 95% accuracy without time-consuming geometric modeling.

This thesis is based on the following publication: (P6)

Thesis 4:

Development of a database for hip implant stem designed with lattice structure

The study developed a comprehensive database for latticed implant stems, that includes the applied materials properties, additive manufacturing properties, cell-specific parameters, cell structure, and patient's weight. The developed database enables the simulation of the implant environment to help facilitate predicting the mechanical behavior of the hip implant. Consequently, the

proposed system offers surgeons the ability to select patient-specific implant solutions, yet within certain limitations

This thesis is based on the following publication: (P3)

Publications

(P1) Alkentar, R.; File, M.; Mankovits, T. Use of Compression Test to Determine the Young's Modulus of the Titanium Alloy Ti6Al4V Manufactured via Direct Metal Laser Sintering. *Int. Rev. Appl. Sci. Eng.* 2023, 14 (2), 256–262. https://doi.org/10.1556/1848.2022.00536.

(P2) Alkentar, R.; Mankovits, T. A Study on the Shape and Dimensional Accuracy of Additively Manufactured Titanium Lattice Structures for Orthopedic Purposes. *Period. Polytech. Mech. Eng.* 2022, 66 (4), 336–343. doi:10.3311/PPme.20382

(P3) Alkentar, R.; Manó, S.; Huri, D.; Mankovits, T., "Development of Patient-Specific Lattice Structured Femoral Stems Based on Finite Element Analysis and Machine Learning," *Crystals*, vol. 15, no. 7, 2025, doi: 10.3390/cryst15070650.

(P4) Alkentar, R.; Mankovits, T. Development of Surrogate Model for Patient-Specific Lattice-Structured Hip Implant Design via Finite Element Analysis. *Appl. Sci.* 2025, 15 (7). https://doi.org/10.3390/app15073522.

(P5) Alkentar, R.; Kladovasilakis, N.; Tzetzis, D.; Mankovits, T. Effects of Pore Size Parameters of Titanium Additively Manufactured Lattice Structures on the Osseointegration Process in Orthopedic Applications: A Comprehensive Review. *Crystals* 2023, 13(1), 1–16. doi:10.3390/cryst13010113.

(P6) Alkentar, R.; Mankovits, T. Optimization of Additively Manufactured and Lattice-Structured Hip Implants Using the Linear Regression Algorithm from the Scikit-Learn Library. *MDPI Cryst*. 2023, 13 (10). doi:10.3390/cryst13101513.

(P7) Alkentar, R.; File, M.; Mankovits, T. Investigation of the Performance of Ti6Al4V Lattice Structures Designed for Biomedical Implants Using the Finite Element Method. *Materials* **2022**, *15*(18), 1–14. doi:10.3390/ma15186335.

(P8) Alkentar, R.; Huri, D.; Mankovits, T. Numerical Investigation of 3D Lattice Infill Pattern Cellular Structure for Orthopedic Implant Design. *In KOD 2021: International Conference on Machine and Industrial Design in Mechanical Engineering. Maja, C., Radivoje, M., Milan, R., Eds.; Springer International Publishing Ag: Berlin*, 2022; pp 467-472 PG – 6. doi:10.1007/978-3-030-88465-9_45.

(P9) Abdon, S. C. F. I.; Alkentar, R.; Bortolini, M. D. M. A.; Gurbanov, O.; Lima, J. M. D. C. Finite element analysis of cellular structures using Ansys. *International Journal of Engineering and Management Sciences* **2021**, *6*(2), 197-204 PG – 8. doi:10.21791/IJEMS.2021.2.16.

(P10) Alkentar, R. Use of ANSYS Software for the Acetabular Cup Structure Analysis out of the Hip Implant. *International Journal of Engineering and Management Sciences* **2020**, *5*(2),1–6. doi:10.21791/IJEMS.2020.2.1.

(P11) Alkentar, R. Topology optimization and rim design. *International Journal of Engineering and Management Sciences* **2019**, *4*(4), 92–101. doi:10.21791/IJEMS.2019.4.10.

(P12) Zhang, L.; Alkentar, R.; Manó, S.; Szabó, J.; Mankovits, T.; Csernátony, Z. Biomechanical Comparison of the Roof Step Cut Technique with the Bulk Bone Graft Technique During Total Hip Arthroplasty for Hip Dysplasia: A Finite Element Analysis. *Acta Chir. Orthop. Traumatol.* Cech. 2023, 90 (5).

(P13) Alkentar, R., Mankovits, T.: Design of Patient Specific Femoral Stem Using Lattice Structures.In: 8th International Scientific Conference on Advances in Mechanical Engineering (ISCAME 2022) / szerk, Homolya Márton, Mankovits

Tamás, Department of Mechanical Engineering, Faculty of Engineering, University of Debrecen, Debrecen, 11-12, 2023. ISBN: 9789634904489

References

[1] A. Terrier, “Adaptation of bone to mechanical stress: theoretical model, experimental identification and orthopedic applications,” 1999, *Verlag nicht ermittelbar*.

[2] M. M. Soliman *et al.*, “A Review of Biomaterials and Associated Performance Metrics Analysis in Pre-Clinical Finite Element Model and in Implementation Stages for Total Hip Implant System,” *Polymers (Basel).*, vol. 14, no. 20, 2022, doi: 10.3390/polym14204308.

[3] P. F. Gomez and J. A. Morcuende, “Early attempts at hip arthroplasty--1700s to 1950s.,” *Iowa Orthop. J.*, vol. 25, pp. 25–29, 2005.

[4] N. H. S. Choices, “Overview - Hip Replacement.” Accessed: Feb. 12, 2025. [Online]. Available: https://www2.hse.ie/conditions/hip-replacement/

[5] L. Guo *et al.*, “On the design evolution of hip implants: A review,” *Mater. Des.*, vol. 216, p. 110552, 2022, doi: https://doi.org/10.1016/j.matdes.2022.110552.

[6] M. Reimeringer and N. Nuño, “The influence of contact ratio and its location on the primary stability of cementless total hip arthroplasty: A finite element analysis,” *J. Biomech.*, vol. 49, no. 7, pp. 1064–1070, 2016, doi: https://doi.org/10.1016/j.jbiomech.2016.02.031.

[7] N. Tan and R. J. van Arkel, “Topology Optimisation for Compliant Hip Implant Design and Reduced Strain Shielding,” 2021. doi: 10.3390/ma14237184.

[8] C. Pabinger, H. Lothaller, N. Portner, and A. Geissler, “Projections of hip arthroplasty in OECD countries up to 2050.,” *Hip Int. J. Clin. Exp. Res. hip Pathol. Ther.*, vol. 28, no. 5, pp. 498–506, Sep. 2018, doi: 10.1177/1120700018757940.

[9] M. Schmitt-Sody, V. Pilger, and L. Gerdesmeyer, “Rehabilitation und Sport nach Hüfttotalendoprothese,” *Orthopade*, vol. 40, no. 6, pp. 513–519, 2011, doi: 10.1007/s00132-011-1761-2.

[10] C. Cooper, G. Campion, and L. J. 3rd Melton, “Hip fractures in the elderly: a world-wide projection.,” *Osteoporos. Int. a J. Establ. as result Coop. between Eur. Found. Osteoporos. Natl. Osteoporos. Found. USA*, vol. 2, no. 6, pp. 285–289, Nov. 1992, doi: 10.1007/BF01623184.

[11] OECD, *Education at a Glance 2019*. 2019. doi: https://doi.org/https://doi.org/10.1787/f8d7880d-en.

[12] T. Dixon, M. Shaw, S. Ebrahim, and P. Dieppe, “Trends in hip and knee joint replacement: socioeconomic inequalities and projections of need,” *Ann. Rheum. Dis.*, vol. 63, no. 7, pp. 825–830, 2004, doi: https://doi.org/10.1136/ard.2003.012724.

[13] L. Risse, S. Woodcock, J.-P. Brüggemann, G. Kullmer, and H. A. Richard, “Stiffness optimization and reliable design of a hip implant by using the potential of additive manufacturing processes,” *Biomed. Eng. Online*, vol. 21, no. 1, p. 23, 2022, doi: 10.1186/s12938-022-00990-z.

[14] H. Derar and M. Shahinpoor, “Recent Patents and Designs on Hip Replacement Prostheses,” *Open Biomed. Eng. J.*, vol. 9, pp. 92–102, 2015, doi: 10.2174/1874120701509010092.

[15] R. Bieger, A. Ignatius, R. Decking, L. Claes, H. Reichel, and L. Dürselen, “Primary stability and strain distribution of cementless hip stems as a function of implant design,” *Clin. Biomech.*, vol. 27, pp. 158–164, 2012, doi: 10.1016/j.clinbiomech.2011.08.004.

[16] G. L. Koons, M. Diba, and A. G. Mikos, “Materials design for bone-tissue engineering,” *Nat. Rev. Mater.*, vol. 5, no. 8, pp. 584–603, 2020, doi:

10.1038/s41578-020-0204-2.

[17] M. Fraldi, L. Esposito, G. Perrella, A. Cutolo, and S. C. Cowin, “Topological optimization in hip prosthesis design,” *Biomech. Model. Mechanobiol.*, vol. 9, no. 4, pp. 389–402, 2010, doi: 10.1007/s10237-009-0183-0.

[18] J. Franklin, O. Robertsson, J. Gestsson, L. S. Lohmander, and T. Ingvarsson, “Revision and complication rates in 654 Exeter total hip replacements, with a maximum follow-up of 20 years,” *BMC Musculoskelet. Disord.*, vol. 4, no. 1, p. 6, 2003, doi: 10.1186/1471-2474-4-6.

[19] D. Gebauer, H. J. Refior, and M. Haake, “Micromotions in the primary fixation of cementless femoral stem prostheses,” *Arch. Orthop. Trauma Surg.*, vol. 108, no. 5, pp. 300–307, 1989, doi: 10.1007/BF00932320.

[20] M. Viceconti, L. Monti, R. Muccini, M. Bernakiewicz, and A. Toni, “Even a thin layer of soft tissue may compromise the primary stability of cementless hip stems,” *Clin. Biomech.*, vol. 16, no. 9, pp. 765–775, 2001, doi: https://doi.org/10.1016/S0268-0033(01)00052-3.

[21] C. A. Engh, D. O’Connor, M. Jasty, T. F. McGovern, J. D. Bobyn, and W. H. Harris, “Quantification of implant micromotion, strain shielding, and bone resorption with porous-coated anatomic medullary locking femoral prostheses,” *Clin. Orthop. Relat. Res.*, no. 285, pp. 13–29, 1992.

[22] K. Soballe, E. S. Hansen, H. Brockstedt-Rasmussen, and C. Bunger, “Hydroxyapatite coating converts fibrous tissue to bone around loaded implants,” *J. Bone Joint Surg. Br.*, vol. 75-B, pp. 270–278, 1993, doi: 10.1302/0301-620x.75b2.8444949.

[23] Y. Ben-Shlomo *et al.*, “The National Joint Registry 17th Annual Report 2020,” 2020, *National Joint Registry, London*.

[24] M. Cilla, S. Checa, and G. N. Duda, “Strain shielding inspired re-design of proximal femoral stems for total hip arthroplasty,” *J. Orthop. Res.*, vol. 35, no. 11, pp. 2534–2544, Nov. 2017, doi: https://doi.org/10.1002/jor.23540.

[25] S. Arabnejad, B. Johnston, M. Tanzer, and D. Pasini, “Fully porous 3D printed titanium femoral stem to reduce stress-shielding following total hip arthroplasty,” *J. Orthop. Res.*, vol. 35, no. 8, pp. 1774–1783, Aug. 2017, doi: https://doi.org/10.1002/jor.23445.

[26] D. R. Sumner, “Long-term implant fixation and stress-shielding in total hip replacement,” *J. Biomech.*, vol. 48, no. 5, pp. 797–800, 2015, doi: https://doi.org/10.1016/j.jbiomech.2014.12.021.

[27] R. Huiskes, H. Weinans, and B. van Rietbergen, “The relationship between stress shielding and bone resorption around total hip stems and the effects of flexible materials.,” *Clin. Orthop. Relat. Res.*, no. 274, pp. 124–134, Jan. 1992.

[28] W. D. Bugbee, C. J. Sychterz, and C. A. Engh, “Bone remodeling around cementless hip implants.,” *South. Med. J.*, vol. 89, no. 11, pp. 1036–1040, Nov. 1996, doi: 10.1097/00007611-199611000-00002.

[29] M.I.Z. Ridzwan, Solehuddin Shuib, A. Y. Hassan, A.A. Shokri, and M. N. M. Ibrahim, “Problem of Stress Shielding and Improvement to the Hip Implant Designs: A Review.”

[30] O. L. A. Harrysson, O. Cansizoglu, D. J. Marcellin-Little, D. R. Cormier, and H. A. West, “Direct metal fabrication of titanium implants with tailored materials and mechanical properties using electron beam melting technology,” *Mater. Sci. Eng. C*, vol. 28, no. 3, pp. 366–373, 2008, doi: https://doi.org/10.1016/j.msec.2007.04.022.

[31] I. Levadnyi, J. Awrejcewicz, J. E. Gubaua, and J. T. Pereira, “Numerical evaluation of bone remodelling and adaptation considering different hip prosthesis designs,” *Clin. Biomech.*, vol. 50, pp. 122–129, 2017, doi: https://doi.org/10.1016/j.clinbiomech.2017.10.015.

[32] K. B. Hazlehurst, C. J. Wang, and M. Stanford, “A numerical investigation into the influence of the properties of cobalt chrome cellular structures on the load transfer to the periprosthetic femur following total hip arthroplasty,” *Med. Eng. Phys.*, vol. 36, no. 4, pp. 458–466, 2014, doi: https://doi.org/10.1016/j.medengphy.2014.02.008.

[33] B. Liu, H. Wang, N. Zhang, M. Zhang, and C.-K. Cheng, “Femoral Stems With Porous Lattice Structures: A Review,” *Front. Bioeng. Biotechnol.*, vol. 9, 2021, doi: 10.3389/fbioe.2021.772539.

[34] T. Q. Lee, D. A. Lewis, S. L. Barnett, W. C. Kim, and S. H. Anzel, “Structural integrity of implanted WMT Infinity hip and Osteonics Omnifit hip in fresh cadaveric femurs,” *J. Biomed. Mater. Res.*, vol. 39, no. 4, pp. 516–523, Mar. 1998, doi: https://doi.org/10.1002/(SICI)1097-4636(19980315)39:4<516::AID-JBM2>3.0.CO;2-M.

[35] J. Orlik, A. Zhurov, and J. Middleton, “On the secondary stability of coated cementless hip replacement: parameters that affected interface strength,” *Med. Eng. Phys.*, vol. 25, no. 10, pp. 825–831, 2003, doi: https://doi.org/10.1016/S1350-4533(03)00099-7.

[36] D. R. Carter, T. E. Orr, and D. P. Fyhrie, “Relationships between loading history and femoral cancellous bone architecture,” *J. Biomech.*, vol. 22, no. 3, pp. 231–244, 1989, doi: https://doi.org/10.1016/0021-9290(89)90091-2.

[37] R. E. Smallman and R. J. Bishop, “Chapter 13 - Biomaterials,” R. E. Smallman and R. J. B. T.-M. P. M. and M. E. (Sixth E. Bishop, Eds., Oxford:

Butterworth-Heinemann, 1999, pp. 394–405. doi: https://doi.org/10.1016/B978-075064564-5/50013-6.

[38] O. Bazaka, K. Bazaka, P. Kingshott, R. J. Crawford, and E. P. Ivanova, “Chapter 1 Metallic Implants for Biomedical Applications,” in *The Chemistry of Inorganic Biomaterials*, The Royal Society of Chemistry, 2021, pp. 1–98. doi: 10.1039/9781788019828-00001.

[39] W. Murphy, J. Black, and G. Hastings, *Handbook of biomaterial properties, second edition*. 2016. doi: 10.1007/978-1-4939-3305-1.

[40] L. T. Kuhn, “Chapter 5 - Biomaterials,” in *Biomedical Engineering*, J. D. Enderle and J. D. B. T.-I. to B. E. (Third E. Bronzino, Eds., Boston: Academic Press, 2012, pp. 219–271. doi: https://doi.org/10.1016/B978-0-12-374979-6.00005-8.

[41] F. Bartolomeu, M. M. Costa, N. Alves, G. Miranda, and F. S. Silva, “Selective Laser Melting of Ti6Al4V sub-millimetric cellular structures: Prediction of dimensional deviations and mechanical performance,” *J. Mech. Behav. Biomed. Mater.*, vol. 113, p. 104123, 2021, doi: https://doi.org/10.1016/j.jmbbm.2020.104123.

[42] F. Bartolomeu, N. Dourado, F. Pereira, N. Alves, G. Miranda, and F. S. Silva, “Additive manufactured porous biomaterials targeting orthopedic implants: A suitable combination of mechanical, physical and topological properties,” *Mater. Sci. Eng. C*, vol. 107, p. 110342, 2020, doi: https://doi.org/10.1016/j.msec.2019.110342.

[43] F. Bartolomeu, M. Gasik, F. S. Silva, and G. Miranda, “Mechanical Properties of Ti6Al4V Fabricated by Laser Powder Bed Fusion: A Review Focused on the Processing and Microstructural Parameters Influence on the Final Properties,” 2022. doi: 10.3390/met12060986.

[44] D. Tigani, M. Fosco, R. Ben Ayad, and R. Fantasia, “6 - Orthopaedic implant materials and design,” in *Woodhead Publishing Series in Biomaterials*, S. B. T.-W. of O. I. and A. J. Affatato, Ed., Woodhead Publishing, 2013, pp. 133–177. doi: https://doi.org/10.1533/9780857096128.1.133.

[45] L. E. Murr *et al.*, “Microstructure and mechanical behavior of Ti-6Al-4V produced by rapid-layer manufacturing, for biomedical applications.,” *J. Mech. Behav. Biomed. Mater.*, vol. 2, no. 1, pp. 20–32, Jan. 2009, doi: 10.1016/j.jmbbm.2008.05.004.

[46] M. Munsch, “15 - Laser additive manufacturing of customized prosthetics and implants for biomedical applications,” in *Woodhead Publishing Series in Electronic and Optical Materials*, M. B. T.-L. A. M. Brandt, Ed., Woodhead Publishing, 2017, pp. 399–420. doi: https://doi.org/10.1016/B978-0-08-100433-3.00015-4.

[47] S. Boonen *et al.*, “Factors Associated with Cortical and Trabecular Bone Loss as Quantified by Peripheral Computed Tomography (pQCT) at the Ultradistal Radius in Aging Women,” *Calcif. Tissue Int.*, vol. 60, no. 2, pp. 164–170, 1997, doi: 10.1007/s002239900208.

[48] N. Koju, S. Niraula, and B. Fotovvati, “Additively Manufactured Porous Ti6Al4V for Bone Implants: A Review,” 2022, *MDPI Metals*. doi: 10.3390/met12040687.

[49] J. Scheinpflug *et al.*, “Journey into Bone Models: A Review,” 2018, *MDPI Genes*. doi: 10.3390/genes9050247.

[50] H. Chen, X. Zhou, H. Fujita, M. Onozuka, and K.-Y. Kubo, “Age-Related Changes in Trabecular and Cortical Bone Microstructure,” *Int. J. Endocrinol.*, vol. 2013, no. 1, p. 213234, 2013, doi: https://doi.org/10.1155/2013/213234.

[51] M. McGregor, S. Patel, S. McLachlin, and Mihaela Vlasea, “Architectural bone parameters and the relationship to titanium lattice design for powder bed fusion additive manufacturing,” *Addit. Manuf.*, vol. 47, p. 102273, 2021, doi: https://doi.org/10.1016/j.addma.2021.102273.

[52] L. J. Gibson, M. F. Ashby, and B. A. Harley, *Cellular Materials in Nature and Medicine*. Cambridge University Press, 2010.

[53] J. Banhart and H.-W. Seeliger, “Aluminium Foam Sandwich Panels: Manufacture, Metallurgy and Applications,” *Adv. Eng. Mater.*, vol. 10, no. 9, pp. 793–802, 2008, doi: https://doi.org/10.1002/adem.200800091.

[54] F. Zhu, G. Lu, D. Ruan, and Z. Wang, “Plastic Deformation, Failure and Energy Absorption of Sandwich Structures with Metallic Cellular Cores,” *Int. J. Prot. Struct.*, vol. 1, no. 4, pp. 507–541, Dec. 2010, doi: 10.1260/2041-4196.1.4.507.

[55] C. Yan, L. Hao, A. Hussein, S. L. Bubb, P. Young, and D. Raymont, “Evaluation of light-weight AlSi10Mg periodic cellular lattice structures fabricated via direct metal laser sintering,” *J. Mater. Process. Technol.*, vol. 214, no. 4, pp. 856–864, 2014, doi: https://doi.org/10.1016/j.jmatprotec.2013.12.004.

[56] L. J. Gibson, “Modelling the mechanical behavior of cellular materials,” *Mater. Sci. Eng. A*, vol. 110, pp. 1–36, 1989, doi: https://doi.org/10.1016/0921-5093(89)90154-8.

[57] M. F. Ashby, “The properties of foams and lattices,” *Philos. Trans. R. Soc. A Math. Phys. Eng. Sci.*, vol. 364, no. 1838, pp. 15–30, Jan. 2006, doi: 10.1098/rsta.2005.1678.

[58] S. Lee, Z. Zhang, and G. X. Gu, “Generative machine learning algorithm for lattice structures with superior mechanical properties,” *Mater. Horizons*,

vol. 9, no. 3, pp. 952–960, 2022, doi: 10.1039/D1MH01792F.

[59] W. Tao and M. C. Leu, “Design of lattice structure for additive manufacturing,” in *2016 International Symposium on Flexible Automation (ISFA)*, 2016, pp. 325–332. doi: 10.1109/ISFA.2016.7790182.

[60] A. Seharing, A. H. Azman, and S. Abdullah, “A review on integration of lightweight gradient lattice structures in additive manufacturing parts,” *Adv. Mech. Eng.*, vol. 12, no. 6, p. 1687814020916951, 2020, doi: 10.1177/1687814020916951.

[61] M. Helou and S. Kara, “Design, analysis and manufacturing of lattice structures: an overview,” *Int. J. Comput. Integr. Manuf.*, vol. 31, no. 3, pp. 243–261, Mar. 2018, doi: 10.1080/0951192X.2017.1407456.

[62] V. S. Deshpande, N. A. Fleck, and M. F. Ashby, “Effective properties of the octet-truss lattice material,” *J. Mech. Phys. Solids*, vol. 49, no. 8, pp. 1747–1769, 2001, doi: https://doi.org/10.1016/S0022-5096(01)00010-2.

[63] SakshiKokil-Shah, A. Sur, S. Darvekar, and M. Shah, “Recent Advancements of Micro-Lattice Structures: Application, Manufacturing Methods, Mechanical Properties, Topologies and Challenges,” *Arab. J. Sci. Eng.*, vol. 46, no. 12, pp. 11587–11600, 2021, doi: 10.1007/s13369-021-05992-y.

[64] H. E. Burton *et al.*, “The design of additively manufactured lattices to increase the functionality of medical implants,” *Mater. Sci. Eng. C*, vol. 94, pp. 901–908, 2019, doi: https://doi.org/10.1016/j.msec.2018.10.052.

[65] A. Zargarian, M. Esfahanian, J. Kadkhodapour, S. Ziaei-Rad, and D. Zamani, “On the fatigue behavior of additive manufactured lattice structures,” *Theor. Appl. Fract. Mech.*, vol. 100, pp. 225–232, 2019, doi:

https://doi.org/10.1016/j.tafmec.2019.01.012.

[66] T. Maconachie *et al.*, “The compressive behaviour of ABS gyroid lattice structures manufactured by fused deposition modelling,” *Int. J. Adv. Manuf. Technol.*, vol. 107, no. 11, pp. 4449–4467, 2020, doi: 10.1007/s00170-020-05239-4.

[67] T. A. Schaedler and W. B. Carter, “Architected Cellular Materials,” *Annu. Rev. Mater. Res.*, vol. 46, no. 1, pp. 187–210, Jul. 2016, doi: 10.1146/annurev-matsci-070115-031624.

[68] L. J. Gibson and M. F. Ashby, *Cellular Solids: Structure and Properties*, 2nd ed. Cambridge: Cambridge University Press, 1997. doi: DOI: 10.1017/CBO9781139878326.

[69] N. Kladovasilakis, K. Tsongas, I. Kostavelis, D. Tzovaras, and D. Tzetzis, “Effective Mechanical Properties of Additive Manufactured Strut-Lattice Structures: Experimental and Finite Element Study,” *Adv. Eng. Mater.*, vol. 24, Oct. 2021, doi: 10.1002/adem.202100879.

[70] N. Kladovasilakis, K. Tsongas, I. Kostavelis, D. Tzovaras, and D. Tzetzis, “Effective mechanical properties of additive manufactured triply periodic minimal surfaces: experimental and finite element study,” *Int. J. Adv. Manuf. Technol.*, vol. 121, no. 11, pp. 7169–7189, 2022, doi: 10.1007/s00170-022-09651-w.

[71] L. J. Gibson, “Cellular Solids,” *MRS Bull.*, vol. 28, pp. 270–274, 2003, doi: 10.1557/mrs2003.79.

[72] M. Brennan, M. Dossi, and M. Moesen, “A Multi-Physics Study of the Wave Propagation Problem in Open Cell Polyurethane Foams,” 2017.

[73] C. Pan, Y. Han, and J. Lu, “Design and Optimization of Lattice Structures: A Review,” *Appl. Sci.*, vol. 10, no. 18, 2020, doi: 10.3390/app10186374.

[74] D. Lehmhus, M. Vesenjak, S. De Schampheleire, and T. Fiedler, “From Stochastic Foam to Designed Structure: Balancing Cost and Performance of Cellular Metals,” *Materials (Basel).*, vol. 10, no. 8, 2017, doi: 10.3390/ma10080922.

[75] K.-M. Park, K.-S. Min, and Y.-S. Roh, “Design Optimization of Lattice Structures under Compression: Study of Unit Cell Types and Cell Arrangements,” 2022. doi: 10.3390/ma15010097.

[76] S. D. Larsen, O. Sigmund, and J. P. Groen, “Optimal truss and frame design from projected homogenization-based topology optimization,” *Struct. Multidiscip. Optim.*, vol. 57, no. 4, pp. 1461–1474, 2018, doi: 10.1007/s00158-018-1948-9.

[77] Y. Jun and K. Choi, “Design of patient-specific hip implants based on the 3D geometry of the human femur,” *Adv. Eng. Softw.*, vol. 41, no. 4, pp. 537–547, 2010, doi: https://doi.org/10.1016/j.advengsoft.2009.10.016.

[78] J. Moya-Angeler, A. L. Gianakos, J. C. Villa, A. Ni, and J. M. Lane, “Current concepts on osteonecrosis of the femoral head.,” *World J. Orthop.*, vol. 6, no. 8, pp. 590–601, Sep. 2015, doi: 10.5312/wjo.v6.i8.590.

[79] S. A. HAQ and F. DAVATCHI, “Osteoarthritis of the knees in the COPCORD world,” *Int. J. Rheum. Dis.*, vol. 14, no. 2, pp. 122–129, May 2011, doi: https://doi.org/10.1111/j.1756-185X.2011.01615.x.

[80] J. T. Evans, J. P. Evans, R. W. Walker, A. W. Blom, M. R. Whitehouse, and A. Sayers, “How long does a hip replacement last? A systematic review and meta-analysis of case series and national registry reports with more than 15 years of follow-up,” *Lancet*, vol. 393, no. 10172, pp. 647–654, 2019, doi: https://doi.org/10.1016/S0140-6736(18)31665-9.

[81] J. L. Knight and R. D. Atwater, “Preoperative planning for total hip

arthroplasty: Quantitating its utility and precision," *J. Arthroplasty*, vol. 7, pp. 403–409, 1992, doi: https://doi.org/10.1016/S0883-5403(07)80031-3.

[82] P. C. Noble, J. W. Alexander, L. J. Lindahl, D. T. Yew, W. M. Granberry, and H. S. Tullos, "The anatomic basis of femoral component design.," *Clin. Orthop. Relat. Res.*, no. 235, pp. 148–165, Oct. 1988.

[83] G. Khang, K. Choi, C.-S. Kim, J. S. Yang, and T.-S. Bae, "A Study of Korean Femoral Geometry," *Clin. Orthop. Relat. Res.*, vol. 406, no. 1, 2003.

[84] H.-J. Laine, J. K. Pajamäki, T. Moilanen, and M. U. Lehto, "The femoral canal fill of two different cementless stem designs," *Int. Orthop.*, vol. 25, no. 4, pp. 209–213, 2001, doi: 10.1007/s002640100245.

[85] J. Hua and P. S. Walker, "Relative motion of hip stems under load. An in vitro study of symmetrical, asymmetrical, and custom asymmetrical designs.," *JBJS*, vol. 76, no. 1, 1994.

[86] N. Sugano, K. Ohzono, T. Nishii, K. Haraguchi, T. Sakai, and T. Ochi, "Computed-tomography-based computer preoperative planning for total hip arthroplasty," *Comput. Aided Surg.*, vol. 3, no. 6, pp. 320–324, Jan. 1998, doi: https://doi.org/10.1002/(SICI)1097-0150(1998)3:6<320::AID-IGS6>3.0.CO;2-O.

[87] C. Götze, V. Vieth, N. Meier, F. Böttner, J. Steinbeck, and L. Hackenberg, "CT-based accuracy of implanting custom-made endoprostheses," *Clin. Biomech.*, vol. 20, no. 8, pp. 856–862, 2005, doi: https://doi.org/10.1016/j.clinbiomech.2005.05.015.

[88] W. L. Healy, "Hip Implant Selection for Total Hip Arthroplasty in Elderly Patients.," *Clin. Orthop. Relat. Res.*, vol. 405, 2002.

[89] P. S. Walker, G. W. Blunn, D. de Prada, and C. Casas, "Design Rationale

and Dimensional Considerations for a Femoral Neck Prosthesis," *Clin. Orthop. Relat. Res.*, vol. 441, 2005.

[90] M. F. Aguiar, A. P. Marques, A. C. P. Carvalho, and M. G. P. Cavalcanti, "Accuracy of magnetic resonance imaging compared with computed tomography for implant planning," *Clin. Oral Implants Res.*, vol. 19, no. 4, pp. 362–365, 2008, doi: https://doi.org/10.1111/j.1600-0501.2007.01490.x.

[91] G. Gautam, S. Kumar, and K. Kumar, "Processing of biomaterials for bone tissue engineering: State of the art," *Mater. Today Proc.*, vol. 50, pp. 2206–2217, 2022, doi: https://doi.org/10.1016/j.matpr.2021.09.459.

[92] S. Todros, M. Todesco, and A. Bagno, "Biomaterials and Their Biomedical Applications: From Replacement to Regeneration," 2021. doi: 10.3390/pr9111949.

[93] J. Guo *et al.*, "Comparison of Tri-Lock Bone Preservation Stem and the Conventional Standard Corail Stem in Primary Total Hip Arthroplasty," *Orthop. Surg.*, vol. 13, no. 3, pp. 749–757, 2021, doi: https://doi.org/10.1111/os.12946.

[94] L. L. Hench and J. M. Polak, "Third-generation biomedical materials.," *Science*, vol. 295, no. 5557, pp. 1014–1017, Feb. 2002, doi: 10.1126/science.1067404.

[95] A. Lenich, H. Vester, M. Nerlich, E. Mayr, U. Stöckle, and B. Füchtmeier, "Clinical comparison of the second and third generation of intramedullary devices for trochanteric fractures of the hip--Blade vs screw.," *Injury*, vol. 41, no. 12, pp. 1292–1296, Dec. 2010, doi: 10.1016/j.injury.2010.07.499.

[96] R. B. Ruben, J. Folgado, and P. R. Fernandes, "Three-dimensional shape

optimization of hip prostheses using a multicriteria formulation," *Struct. Multidiscip. Optim.*, vol. 34, no. 3, pp. 261–275, 2007, doi: 10.1007/s00158-006-0072-4.

[97] A. D. Ross and J. R. Howell, "Cemented hip arthroplasty: techniques used in primary and revision surgery," *Orthop. Trauma*, vol. 36, no. 1, pp. 22–29, 2022, doi: https://doi.org/10.1016/j.mporth.2021.11.004.

[98] S. Nazari-Farsani, "Precision and Accuracy of Marker-Based and Model-Based Radiostereometric Analyses in Determination of Three-Dimensional Micromotion of a Novel Hip Stem," 2014.

[99] F. Bottner, E. Su, B. Nestor, B. Azzis, T. P. Sculco, and M. Bostrom, "Radiostereometric analysis: the hip.," *HSS J.*, vol. 1, no. 1, pp. 94–99, Sep. 2005, doi: 10.1007/s11420-005-0114-2.

[100] H. S. Khanuja, J. J. Vakil, M. S. Goddard, and M. A. Mont, "Cementless Femoral Fixation in Total Hip Arthroplasty," *JBJS*, vol. 93, no. 5, 2011, [Online]. Available: https://journals.lww.com/jbjsjournal/fulltext/2011/03020/cementless_femoral_fixation_in_total_hip.12.aspx

[101] A. Chung, "Hip Joint Replacement Surgery |." Accessed: May 28, 2025. [Online]. Available: https://www.healthpages.org/surgical-care/hip-joint-replacement-surgery/

[102] P.-I. Branemark, "Osseointegration and its experimental background," *J. Prosthet. Dent.*, vol. 50, no. 3, pp. 399–410, 1983, doi: https://doi.org/10.1016/S0022-3913(83)80101-2.

[103] P. I. BRANEMARK, "Vital microscopy of bone marrow in rabbit.," *Scand. J. Clin. Lab. Invest.*, vol. 11 Supp 38, pp. 1–82, 1959.

[104] E. C. S. Rigo, A. O. Boschi, M. Yoshimoto, S. Allegrini, B. Konig, and M. J.

Carbonari, “Evaluation in vitro and in vivo of biomimetic hydroxyapatite coated on titanium dental implants,” *Mater. Sci. Eng. C*, vol. 24, no. 5, pp. 647–651, 2004, doi: https://doi.org/10.1016/j.msec.2004.08.044.

[105] L. Linder *et al.*, “Electron microscopic analysis of the bone-titanium interface.,” *Acta Orthop. Scand.*, vol. 54, no. 1, pp. 45–52, Feb. 1983, doi: 10.3109/17453678308992868.

[106] A. F. Mavrogenis, R. Dimitriou, J. Parvizi, and G. C. Babis, “Biology of implant osseointegration.,” *J. Musculoskelet. Neuronal Interact.*, vol. 9, no. 2, pp. 61–71, 2009.

[107] F. Marco, F. Milena, G. Gianluca, and O. Vittoria, “Peri-implant osteogenesis in health and osteoporosis.,” *Micron*, vol. 36, no. 7–8, pp. 630–644, 2005, doi: 10.1016/j.micron.2005.07.008.

[108] L. Linder, K. Obrant, and G. Boivin, “Osseointegration of metallic implants. II. Transmission electron microscopy in the rabbit.,” *Acta Orthop. Scand.*, vol. 60, no. 2, pp. 135–139, Apr. 1989, doi: 10.3109/17453678909149240.

[109] K. Søballe, “Hydroxyapatite ceramic coating for bone implant fixation. Mechanical and histological studies in dogs.,” *Acta Orthop. Scand. Suppl.*, vol. 255, pp. 1–58, 1993, doi: 10.3109/17453679309155636.

[110] N. J. Giori, L. Ryd, and D. R. Carter, “Mechanical influences on tissue differentiation at bone-cement interfaces.,” *J. Arthroplasty*, vol. 10, no. 4, pp. 514–522, Aug. 1995, doi: 10.1016/s0883-5403(05)80154-8.

[111] B. Otsuki, M. Takemoto, S. Fujibayashi, M. Neo, T. Kokubo, and T. Nakamura, “Pore throat size and connectivity determine bone and tissue ingrowth into porous implants: Three-dimensional micro-CT based structural analyses of porous bioactive titanium implants,” *Biomaterials*,

vol. 27, no. 35, pp. 5892–5900, 2006, doi: https://doi.org/10.1016/j.biomaterials.2006.08.013.

[112] M. Kudo, Y. Matsui, K. Ohno, and K. Michi, "A histomorphometric study of the tissue reaction around hydroxyapatite implants irradiated after placement.," *J. oral Maxillofac. Surg. Off. J. Am. Assoc. Oral Maxillofac. Surg.*, vol. 59, no. 3, pp. 293–300; discussion 301, Mar. 2001, doi: 10.1053/joms.2001.20998.

[113] R. Rosenqvist *et al.*, "Loosening of the porous coating of bicompartmental prostheses in patients with rheumatoid arthritis.," *J. Bone Joint Surg. Am.*, vol. 68, no. 4, pp. 538–542, Apr. 1986.

[114] H. Zhang, C. G. Lewis, M. S. Aronow, and G. A. Gronowicz, "The effects of patient age on human osteoblasts' response to Ti-6Al-4V implants in vitro.," *J. Orthop. Res. Off. Publ. Orthop. Res. Soc.*, vol. 22, no. 1, pp. 30–38, Jan. 2004, doi: 10.1016/S0736-0266(03)00155-4.

[115] A. Mombelli and N. Cionca, "Systemic diseases affecting osseointegration therapy.," *Clin. Oral Implants Res.*, vol. 17 Suppl 2, pp. 97–103, Oct. 2006, doi: 10.1111/j.1600-0501.2006.01354.x.

[116] K. Anselme, "Osteoblast adhesion on biomaterials.," *Biomaterials*, vol. 21, no. 7, pp. 667–681, Apr. 2000, doi: 10.1016/s0142-9612(99)00242-2.

[117] J. Breme, E. Steinhäuser, and G. Paulus, "Commercially pure titanium Steinhäuser plate-screw system for maxillofacial surgery," *Biomaterials*, vol. 9, no. 4, pp. 310–313, 1988, doi: https://doi.org/10.1016/0142-9612(88)90024-5.

[118] M. Fini *et al.*, "Osteoporosis and biomaterial osteointegration," *Biomed. Pharmacother.*, vol. 58, no. 9, pp. 487–493, 2004, doi:

https://doi.org/10.1016/j.biopha.2004.08.016.

[119] J. D. Bobyn, R. M. Pilliar, H. U. Cameron, and G. C. Weatherly, “The optimum pore size for the fixation of porous-surfaced metal implants by the ingrowth of bone.,” *Clin. Orthop. Relat. Res.*, no. 150, pp. 263–270, 1980.

[120] J. D. Bobyn, G. J. Stackpool, S. A. Hacking, M. Tanzer, and J. J. Krygier, “Characteristics of bone ingrowth and interface mechanics of a new porous tantalum biomaterial.,” *J. Bone Joint Surg. Br.*, vol. 81, no. 5, pp. 907–914, Sep. 1999, doi: 10.1302/0301-620x.81b5.9283.

[121] Á. É. Kovács *et al.*, “Comparative Analysis of Bone Ingrowth in 3D-Printed Titanium Lattice Structures with Different Patterns,” *Materials (Basel).*, vol. 16, no. 10, 2023, doi: 10.3390/ma16103861.

[122] V. Karageorgiou and D. Kaplan, “Porosity of 3D biomaterial scaffolds and osteogenesis,” *Biomaterials*, vol. 26, no. 27, pp. 5474–5491, 2005, doi: https://doi.org/10.1016/j.biomaterials.2005.02.002.

[123] M. de Wild *et al.*, “Bone regeneration by the osteoconductivity of porous titanium implants manufactured by selective laser melting: a histological and micro computed tomography study in the rabbit.,” *Tissue Eng. Part A*, vol. 19, no. 23–24, pp. 2645–2654, Dec. 2013, doi: 10.1089/ten.TEA.2012.0753.

[124] S. Arabnejad, R. Burnett Johnston, J. A. Pura, B. Singh, M. Tanzer, and D. Pasini, “High-strength porous biomaterials for bone replacement: A strategy to assess the interplay between cell morphology, mechanical properties, bone ingrowth and manufacturing constraints.,” *Acta Biomater.*, vol. 30, pp. 345–356, Jan. 2016, doi: 10.1016/j.actbio.2015.10.048.

[125] J. Wegrzyn, K. R. Kaufman, A. D. Hanssen, and D. G. Lewallen, “Performance of Porous Tantalum vs. Titanium Cup in Total Hip Arthroplasty: Randomized Trial with Minimum 10-Year Follow-Up,” *J. Arthroplasty*, vol. 30, no. 6, pp. 1008–1013, 2015, doi: https://doi.org/10.1016/j.arth.2015.01.013.

[126] A. Rashwan, N. Kladovasilakis, D. Tzetzis, and T. Mankovits, “Effects of Pore Size Parameters of Titanium Additively Manufactured Lattice Structures on the Osseointegration Process in Orthopedic Applications: A Comprehensive Review,” *Crystals*, vol. 13, no. 1, pp. 1–16, 2023, doi: 10.3390/cryst13010113.

[127] J. W. K. Choi Namkug, “Clinical Application of Three-Dimensional Printing Technology in Craniofacial Plastic Surgery,” *Arch Plast Surg*, vol. 42, no. 03, pp. 267–277, 2015, doi: 10.5999/aps.2015.42.3.267.

[128] L. Kumar, M. Tanveer, V. Kumar, M. Javaid, and A. Haleem, “Developing low cost 3 D printer,” vol. 5, Jan. 2016, doi: 10.6088/ijaser.05042.

[129] M. Javaid and A. Haleem, “Additive manufacturing applications in orthopaedics: A review,” *J. Clin. Orthop. Trauma*, vol. 9, no. 3, pp. 202–206, 2018, doi: https://doi.org/10.1016/j.jcot.2018.04.008.

[130] D. Herzog, V. Seyda, E. Wycisk, and C. Emmelmann, “Additive manufacturing of metals,” *Acta Mater.*, vol. 117, pp. 371–392, 2016, doi: https://doi.org/10.1016/j.actamat.2016.07.019.

[131] J. H. Tan, W. L. E. Wong, and K. W. Dalgarno, “An overview of powder granulometry on feedstock and part performance in the selective laser melting process,” *Addit. Manuf.*, vol. 18, pp. 228–255, 2017, doi: https://doi.org/10.1016/j.addma.2017.10.011.

[132] L.-C. Zhang, Y. Liu, S. Li, and Y. Hao, “Additive Manufacturing of Titanium

Alloys by Electron Beam Melting: A Review," *Adv. Eng. Mater.*, vol. 20, no. 5, p. 1700842, May 2018, doi: https://doi.org/10.1002/adem.201700842.

[133] I. Gibson, D. Rosen, B. Stucker, and M. Khorasani, *Additive Manufacturing Technologies*. Springer International Publishing, 2021. doi: 10.1007/978-3-030-56127-7.

[134] I. Yadroitsev, P. Bertrand, and I. Smurov, "Parametric analysis of the selective laser melting process," *Appl. Surf. Sci.*, vol. 253, no. 19, pp. 8064–8069, 2007, doi: https://doi.org/10.1016/j.apsusc.2007.02.088.

[135] J.-P. Kruth, M. Badrossamay, E. Yasa, J. Deckers, L. Thijs, and J. Van Humbeeck, "Part and material properties in selective laser melting of metals," 2010, *SHANGHAI JIAO TONG UNIV PRESS*.

[136] J. Nandy, H. Sarangi, and S. Sahoo, "A Review on Direct Metal Laser Sintering: Process Features and Microstructure Modeling," *Lasers Manuf. Mater. Process.*, vol. 6, no. 3, pp. 280–316, 2019, doi: 10.1007/s40516-019-00094-y.

[137] T. Grünberger and R. Domröse, "Optical In-Process Monitoring of Direct Metal Laser Sintering (DMLS)," *Laser Tech. J.*, vol. 11, no. 2, pp. 40–42, Apr. 2014, doi: https://doi.org/10.1002/latj.201400026.

[138] M. Helou, S. Vongbunyong, and S. Kara, "Finite Element Analysis and Validation of Cellular Structures," *Procedia CIRP*, vol. 50, pp. 94–99, 2016, doi: https://doi.org/10.1016/j.procir.2016.05.018.

[139] A. H. Choi, "19 - Stress induced at the bone-particle-reinforced nanocomposite interface: a finite element approach," in *Woodhead Publishing Series in Composites Science and Engineering*, K. L. Goh, A. M.K., R. T. De Silva, and S. B. T.-I. in P. and F. R. C. Thomas, Eds.,

Woodhead Publishing, 2020, pp. 515–528. doi: https://doi.org/10.1016/B978-0-08-102665-6.00019-4.

[140] C. Z. J. Juarez, S. C. Koay, M. Y. Chan, H. L. Choo, M. M. Pang, and T. K. Ong, "Finite Element Analysis Study on Lattice Structure Fabricated Recycled Polystyrene from Post-used Styrofoam Waste," *MATEC Web Conf.*, vol. 335, 2021.

[141] S. A. C. Ghani, W. S. W. Harun, Z. A. Mat Taib, F. F. Ab Rashid, R. M. Hazlen, and M. A. Omar, "Finite Element Analysis of Porous Medical Grade Cobalt Chromium Alloy Structures Produced by Selective Laser Melting," *Adv. Mater. Res.*, vol. 1133, pp. 113–118, 2016, doi: 10.4028/www.scientific.net/AMR.1133.113.

[142] T. A. Maxian, T. D. Brown, D. R. Pedersen, and J. J. Callaghan, "A sliding-distance-coupled finite element formulation for polyethylene wear in total hip arthroplasty," *J. Biomech.*, vol. 29, no. 5, pp. 687–692, 1996, doi: https://doi.org/10.1016/0021-9290(95)00125-5.

[143] A. A. Besong, R. Lee, R. Farrar, and Z. M. Jin, "Contact mechanics of a novel metal-on-metal total hip replacement," *Proc. Inst. Mech. Eng. Part H*, vol. 215, no. 6, pp. 543–548, 2001, doi: 10.1243/0954411011536145.

[144] F. Liu, Y. He, Z. Gao, and D. Jiao, "Enhanced computational modelling of UHMWPE wear in total hip joint replacements: The role of frictional work and contact pressure," *Wear*, vol. 482–483, p. 203985, 2021, doi: https://doi.org/10.1016/j.wear.2021.203985.

[145] A. L. Sabatini and T. Goswami, "Hip implants VII: Finite element analysis and optimization of cross-sections," *Mater. Des.*, vol. 29, no. 7, pp. 1438–1446, 2008, doi: https://doi.org/10.1016/j.matdes.2007.09.002.

[146] N. Wu *et al.*, "The advances of topology optimization techniques in

orthopedic implants: A review," *Med. Biol. Eng. Comput.*, vol. 59, no. 9, pp. 1673–1689, 2021, doi: 10.1007/s11517-021-02361-7.

[147] M. P. Bendsøe and O. Sigmund, *Topology Optimization*. Springer Berlin Heidelberg PP - Berlin, Heidelberg, 2004. doi: 10.1007/978-3-662-05086-6.

[148] J.-H. Zhu, W.-H. Zhang, and L. Xia, "Topology Optimization in Aircraft and Aerospace Structures Design," *Arch. Comput. Methods Eng.*, vol. 23, no. 4, pp. 595–622, 2016, doi: 10.1007/s11831-015-9151-2.

[149] M. P. Bendsøe and N. Kikuchi, "Generating optimal topologies in structural design using a homogenization method," *Comput. Methods Appl. Mech. Eng.*, vol. 71, no. 2, pp. 197–224, 1988, doi: https://doi.org/10.1016/0045-7825(88)90086-2.

[150] G. Chahine, P. Smith, and R. Kovacevic, "Application of Topology Optimization in Modern Additive Manufacturing," 2010.

[151] E. J. HEARN, "CHAPTER 11 - STRAIN ENERGY," E. J. B. T.-M. of M. 1 (Third E. HEARN, Ed., Oxford: Butterworth-Heinemann, 1997, pp. 254–296. doi: https://doi.org/10.1016/B978-075063265-2/50012-8.

[152] Q. Li, G. P. Steven, and Y. M. Xie, "On equivalence between stress criterion and stiffness criterion in evolutionary structural optimization," *Struct. Optim.*, vol. 18, no. 1, pp. 67–73, 1999, doi: 10.1007/BF01210693.

[153] Y. He, D. Burkhalter, D. Durocher, and J. M. Gilbert, "Solid-Lattice Hip Prosthesis Design: Applying Topology and Lattice Optimization to Reduce Stress Shielding From Hip Implants," Apr. 2018. doi: 10.1115/DMD2018-6804.

[154] A. Challapalli and G. Li, "Machine learning assisted design of new lattice core for sandwich structures with superior load carrying capacity," *Sci.*

Rep., vol. 11, no. 1, p. 18552, 2021, doi: 10.1038/s41598-021-98015-7.

[155] N. Després, E. Cyr, P. Setoodeh, and M. Mohammadi, “Deep Learning and Design for Additive Manufacturing: A Framework for Microlattice Architecture,” *JOM*, vol. 72, no. 6, pp. 2408–2418, 2020, doi: 10.1007/s11837-020-04131-6.

[156] M. Guven and F. Uysal, “A New Method for Heart Disease Detection: Long Short-Term Feature Extraction from Heart Sound Data,” *Sensors*, vol. 23, no. 13, 2023, doi: 10.3390/s23135835.

[157] N. Najwa Mohd Rizal, G. Hayder, M. Mnzool, B. M. E. Elnaim, A. O. Y. Mohammed, and M. M. Khayyat, “Comparison between Regression Models, Support Vector Machine (SVM), and Artificial Neural Network (ANN) in River Water Quality Prediction,” *Processes*, vol. 10, no. 8, 2022, doi: 10.3390/pr10081652.

[158] R. Kulagin, Y. Beygelzimer, Y. Estrin, A. Schumilin, and P. Gumbsch, “Architectured Lattice Materials with Tunable Anisotropy: Design and Analysis of the Material Property Space with the Aid of Machine Learning,” *Adv. Eng. Mater.*, vol. 22, no. 12, p. 2001069, Dec. 2020, doi: https://doi.org/10.1002/adem.202001069.

[159] S. Kumar, S. Tan, L. Zheng, and D. M. Kochmann, “Inverse-designed spinodoid metamaterials,” *npj Comput. Mater.*, vol. 6, no. 1, p. 73, 2020, doi: 10.1038/s41524-020-0341-6.

[160] D. A. White, W. J. Arrighi, J. Kudo, and S. E. Watts, “Multiscale topology optimization using neural network surrogate models,” *Comput. Methods Appl. Mech. Eng.*, vol. 346, pp. 1118–1135, 2019, doi: https://doi.org/10.1016/j.cma.2018.09.007.

[161] S. Ma, Q. Tang, Y. Liu, and Q. Feng, “Prediction of Mechanical Properties

of Three-Dimensional Printed Lattice Structures Through Machine Learning," *J. Comput. Inf. Sci. Eng.*, vol. 22, no. 3, Dec. 2021, doi: 10.1115/1.4053077.

[162] G. Yu, L. Xiao, and W. Song, "Deep learning-based heterogeneous strategy for customizing responses of lattice structures," *Int. J. Mech. Sci.*, vol. 229, p. 107531, 2022, doi: https://doi.org/10.1016/j.ijmecsci.2022.107531.

[163] Q. Zeng, Z. Zhao, H. Lei, and P. Wang, "A deep learning approach for inverse design of gradient mechanical metamaterials," *Int. J. Mech. Sci.*, vol. 240, p. 107920, 2023, doi: https://doi.org/10.1016/j.ijmecsci.2022.107920.

[164] H. Hassanin, Y. Alkendi, M. Elsayed, K. Essa, and Y. Zweiri, "Controlling the Properties of Additively Manufactured Cellular Structures Using Machine Learning Approaches," *Adv. Eng. Mater.*, vol. 22, no. 3, p. 1901338, Mar. 2020, doi: https://doi.org/10.1002/adem.201901338.

[165] G. E. Hinton, S. Osindero, and Y.-W. Teh, "A Fast Learning Algorithm for Deep Belief Nets," *Neural Comput.*, vol. 18, no. 7, pp. 1527–1554, Jul. 2006, doi: 10.1162/neco.2006.18.7.1527.

[166] EOS.info, "Technical Data EOS M 290." Accessed: Jun. 25, 2022. [Online]. Available: https://www.eos.info/metal-solutions/metal-printers/data-sheets/sds-eos-m-290

[167] A. Rashwan and T. Mankovits, "A Study on the Shape and Dimensional Accuracy of Additively Manufactured Titanium Lattice Structures for Orthopedic Purposes," 2022.

[168] G. Metrology, "Industrial 3D Measuring Systems with High-Speed Technology." Accessed: Jun. 10, 2025. [Online]. Available:

https://www.zeiss.com/metrology/en/systems/optical-3d.html

[169] A. Rashwan, M. File, and T. Mankovits, “Investigation of the Performance of Ti6Al4V Lattice Structures Designed for Biomedical Implants Using the Finite Element Method,” *Materials (Basel).*, vol. 15, no. 18, pp. 1–14, 2022, doi: 10.3390/ma15186335.

[170] L. Punnett and D. H. Wegman, “Work-related musculoskeletal disorders: the epidemiologic evidence and the debate.,” *J. Electromyogr. Kinesiol. Off. J. Int. Soc. Electrophysiol. Kinesiol.*, vol. 14, no. 1, pp. 13–23, Feb. 2004, doi: 10.1016/j.jelekin.2003.09.015.

[171] N. Tagawa *et al.*, “Heterologous enzyme immunoassay for serum androstenediol.,” *Clin. Chim. Acta.*, vol. 296, no. 1–2, pp. 193–201, Jun. 2000, doi: 10.1016/s0009-8981(00)00261-8.

[172] F. Nemathaga, S. Maringa, and L. Chimuka, “Hospital solid waste management practices in Limpopo Province, South Africa: a case study of two hospitals.,” *Waste Manag.*, vol. 28, no. 7, pp. 1236–1245, 2008, doi: 10.1016/j.wasman.2007.03.033.

[173] J. Y. Rho, R. B. Ashman, and C. H. Turner, “Young’s modulus of trabecular and cortical bone material: ultrasonic and microtensile measurements.,” *J. Biomech.*, vol. 26, no. 2, pp. 111–119, Feb. 1993, doi: 10.1016/0021-9290(93)90042-d.

[174] R. Carrá *et al.*, “Hepatitis C virus genotypes in elderly patients with chronic hepatitis C.,” *Arch. Gerontol. Geriatr.*, vol. 22 Suppl 1, pp. 287–290, 1996, doi: 10.1016/0167-4943(96)86950-0.

[175] G. Bertola, B. Pasquotti, S. Morassut, S. Massarut, R. Sigon, and C. Rossi, “Primary lung melanoma.,” *Ital. J. Surg. Sci.*, vol. 19, no. 2, pp. 187–189, 1989.

[176] “ISO 7206-4:2010,” 2010. Accessed: Feb. 12, 2025. [Online]. Available: https://www.iso.org/standard/42769.html

[177] A. Rashwan and T. Mankovits, “Development of Surrogate Model for Patient-Specific Lattice-Structured Hip Implant Design via Finite Element Analysis,” *Appl. Sci.*, vol. 15, no. 7, pp. 1–14, 2025, doi: 10.3390/app15073522.

[178] “Standard Specification for Total Hip Joint Prosthesis and Hip Endoprosthesis Bearing Surfaces Made of Metallic, Ceramic, and Polymeric Materials; ASTM F2033-12; ASTM International: West Conshohocken, PA, USA, 2012.,” 2012.

[179] F. Pedregosa *et al.*, “Scikit-learn: Machine Learning in {P}ython,” *J. Mach. Learn. Res.*, vol. 12, pp. 2825–2830, 2011.

[180] Mathworks, “Choose Regression Model Options.” Accessed: May 21, 2025. [Online]. Available: https://www.mathworks.com/help/stats/choose-regression-model-options.html#bvmpn_3-1

[181] G. Bergmann *et al.*, “Realistic loads for testing hip implants,” *Biomed. Mater. Eng.*, vol. 20, no. 2, pp. 65–75, 2010, doi: 10.3233/BME-2010-0616.

[182] G. Bergmann, F. Graichen, and A. Rohlmann, “Hip joint loading during walking and running, measured in two patients.,” *J. Biomech.*, vol. 26, no. 8, pp. 969–990, Aug. 1993, doi: 10.1016/0021-9290(93)90058-m.